Justus-Liebig-Universität Gießen

I. Physikalisches Institut

Impedimetric detection of anticancer drug action on individual tumor cells using field-effect transistor devices

Dissertation zur Erlangung des akademischen Grades einer

Doktorin der Naturwissenschaften

(Doctor rerum naturalium)

vorgelegt dem Fachbereich

Mathematik und Informatik, Physik, Geographie

von

Anna Susloparova

angefertigt bei Prof. Dr. Sven Ingebrandt

an der Hochschule Kaiserslautern – Standort Zweibrücken

Arbeitsgruppe Biomedizinische Messtechnik

Berichterstatter: Universitätsprofessor: Prof. Dr. Martin Eickhoff

Hochschulprofessor: Prof. Dr. Sven Ingebrandt

Abstract

This thesis describes an advancement in a new technique for measuring biological and electronic properties of individual cells on planar devices. The measuring principle of this technique is based on the impedance measurement of open-gate field-effect transistor (FET) devices. Due to the fact that the size of the transistor gate is comparable with the size of individual cells, FET devices can achieve a real single cell analysis. Thus, the application of FET devices for this technique can extend to cell cultures, which do not form confluent cell layers, such as nerve cells, individual cells of the immune system, etc.

The aim of this work was to investigate the cell-substrate adhesion process at an individual cell level using FET devices and to develop and elaborate a model explanation for the spectra, since the cellular adhesion plays an important part for understanding cancer cell behaviour. We further used this technique to proof effects of anticancer drugs to individual tumor cells.

In the context of this work, a new amplifier system was developed, which offered an increased bandwidth of the readout system and enabled measuring of impedance spectra at higher frequencies (up to 50 MHz). The impedance spectra recorded with this measurement setup were interpreted with an electrically equivalent circuit (EEC) model, for which an analytical expression was derived.

The measured impedance spectra with the developed amplifier system were fitted with the derived analytical expression and cell-related parameters were extracted. The ability to extract the biological relevant data from these complex spectra might be very important for the future application of our novel technique in biological experiments. Moreover, we utilized this EEC model to extract the device-related parameters and to fabricate a new generation of FET devices with better performance in cell-substrate adhesion experiments.

However, the FET devices based on silicon are complex, expensive to manufacture, and have the significant disadvantage in cell culture applications that they are not optically transparent. Due to this fact, devices based on organic semiconductor material were developed and fabricated in this work. The cellular adhesion experiments performed in this work eventually open up commercial opportunities for the Electrical Cell-substrate Impedance Sensing using field-effect transistors.

Contents

Chapter 1

1 Introduction

Adhesion of cells to *in vitro* surfaces finds broad interest from medical technology and biotechnology (Janshoff et al., 2010). Cell adhesion acts as an indicator for understanding cancer cell behavior such as migration, proliferation and invasion (Hong et al., 2011).

Cell-substrate adhesion can be studied by optical methods. Using reflection interference contrast microscopy, the cell adhesion dynamic can be investigated (Michaelis et al., 2012) (Curtis, 1964). With fluorescence interference contrast microscopy the exact cell–substrate separation distance can be measured (Michaelis et al., 2012) (Braun and Fromherz, 1998) (Lambacher and Fromherz, 1996). Total internal reflection fluorescence microscopy and total internal reflection aqueous fluorescence microscopy can be used for visualizing the cell–surface junction of living cells (Michaelis et al., 2012) (Geggier and Fuhr, 1999).

Moreover, cell-substrate adhesion can be recorded electronically by impedance spectroscopy. The electric cell-substrate impedance sensing (ECIS) approach on gold electrodes is well-known for decades and several commercial systems are applied in biomedical research (AppliedBiophysics, http://www.biophysics.com) (ACEA Biosciences, http://www.aceabio.com) (Molecular Devices, http://www.moleculardevices.com). This technique is used to study cancer, wound healing, toxicology, asthma, and the blood brain barrier. However, due to the sizes of the gold electrodes (typical 250 µm in diameter, AppliedBiophysics, http://www.biophysics.com) the attainment of the single cell resolution is difficult realizable.

The downscaling of metal electrodes for ECIS is limited, due to the fact that for a very small geometry of the electrodes (50 µm or less) the high metal-liquid interface impedance is resulting in large electrode impedances, which dominate the overall system impedance (Pradhan et al., 2012). In addition, cable impedance plays a decisive role in this case (Xiao et al., 2002). The lower size of the gold electrodes is 50 µm in diameter (Abdurrahman et al., 2007). Nevertheless, with the ECIS approach changes in cell-cell junction, in membrane capacitance and sealing resistance of the cell-substrate contact can be measured. However, these experiments are always done on a colony of cells on larger electrodes. Then the ECIS data can be interpreted with an established circuit model (Giaever and Keese, 1993) (Giaever and Keese, 1991).

An alternative approach for ECIS, which will be elaborated in this work, is the investigation of the cell-substrate adhesion with open-gate field-effect transistor (FET) devices. Transistors benefit from their very high sensitivity to changes in surface potential at the liquid-solid interface and their capability of miniaturization in size. In an impedance readout approach the input impedance is largely reduced compared to ECIS electrodes. The gate size of the open-gate transistor devices is comparable with the size of individual cells (Figure 1-1).

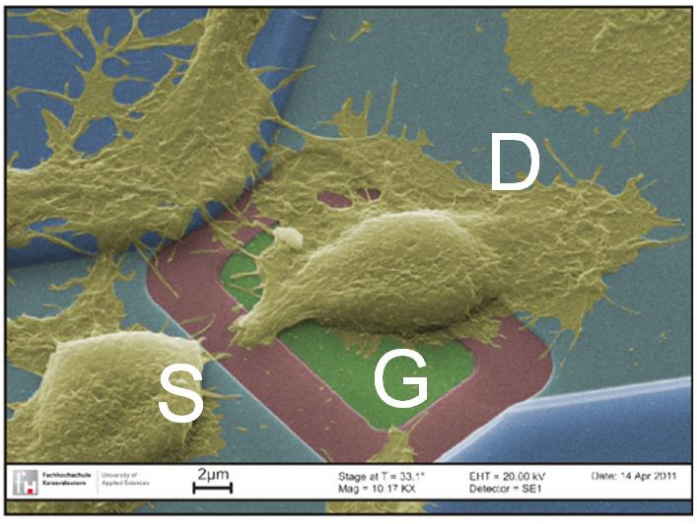

Figure 1-1 Colored scanning electron microscope image of a HEK293 cell, which is attached to an open-gate transistor structure. Source (S) and drain (D) contacts are indicated in the figure. The electrically sensitive part of the FET is marked (G) and in this case measures 16×1.5 µm^2. This image was adapted from (Susloparova et al., 2013).

Open-gate FET devices were applied for the detection of proteins (Bergveld, 2003), DNA sequences (Uslu et al., 2004) (Souteyrand et al., 1997), action potentials of neuronal (Fromherz et al., 1991) and cardiac cells (Ingebrandt et al., 2001) (Sprössler et al., 1999), and enzyme attachment and activities (Katz and Willner, 2003) (Kharitonov et al., 2001). An overview of FETs used in cell culture assays can be found by (Poghossian et al., 2009). Impedance spectroscopy with FETs was applied for immunosensing assays (Schasfoort et al., 1989), to test the encapsulation of ISFET devices (Chovelon et al., 1991), for protein detection (GhoshMoulick et al., 2009) (Kharitonov et al., 2001) (Kruise et al., 1992), for DNA detection (Ingebrandt et al., 2007), and for impedimetric sensing of cell-substrate adhesion (Schäfer et al., 2009).

The main disadvantages of the silicon-based FET devices compared to metal microelectrodes are the more complicated fabrication process and the opaque substrate, which interferes with standard cell culture microscopy. Devices based on organic semiconductor materials may provide low cost, easy fabrication and optical transparency (Lin and Yan, 2012) (Lin et al., 2010b). Therefore they might be an alternative for further biosensor developments. These devices were investigated as an alternative to the silicon FETs for transistor–based cell impedance sensing.

In general, organic semiconductor materials showed excellent performance in different electronic devices such as organic light-emitting diodes, organic solar cells, and organic thin-film transistors (OTFTs) (Lin and Yan, 2012). OTFTs can be divided into two types of transistors: organic field-effect transistors (OFETs) and organic electrochemical transistors (OECTs). Different conjugated polymers such as poly(3-hexylthiophene) (P3HT), poly(3-methylthiophene), polyaniline (PANI), polypyrrole, polycarbazole, and poly(3,4-ethylenedioxythiophene):poly(styrene sulfonate) (PEDOT:PSS) were used as the active layers for applications in chemical and biological sensing (Lin and Yan, 2012) (Lin et al., 2010b). The organic semiconductor films can be deposited on the glass substrates by low cost manufacturing processes such as spin coating (Lin et al., 2010b), screen printing (Rogers et al., 2001) and inkjet printing (Basiricò et al., 2012) (Nikolou and Malliaras, 2008) (Sirringhaus et al., 2000). Such devices were used in various chemical sensor systems:

- humidity sensor
    - OFET: (Li et al., 2005) (Zhu et al., 2002)
    - OECT: (Nilsson et al., 2002)

- ions sensor
    - OFET: (Scarpa et al., 2010b) (Ji et al., 2008)
    - OECT: (Mousavi et al., 2009) (Bernards et al., 2006)
- pH sensor
    - OFET: (Spijkman et al., 2010) (Caboni et al., 2009a) (Caboni et al., 2009b) (Loi et al., 2005) (Bartic et al., 2002)
    - OECT: (Paul et al., 1985) (Thackeray et al., 1985)

and biological sensor systems:

- antibody-antigen sensor
    - OECT: (Kim et al., 2010) (Kanungo et al., 2002)
- glucose sensor
    - OFET: (Liu et al., 2008) (Bartic et al., 2003) (Someya et al., 2002)
    - OECT: (Tang et al., 2011) (Yang et al., 2010) (Yang et al., 2009) (Shim et al., 2009)
- DNA sensor
    - OFET: (Khan et al., 2010) (Stoliar et al., 2009) (Yan et al., 2009)
    - OECT: (Lin et al., 2011) (Krishnamoorthy et al., 2004)
- cell sensor
    - OFET: (Scarpa et al., 2010a)
    - OECT: (Lin et al., 2010b) (Bolin et al., 2009).

At the beginning of this thesis following tasks needed to be addressed:

- Improvement of an existing impedimetric readout system
- Understanding and interpretation of the impedance spectra measured from cells
- Optimization and fabrication of FET devices based on silicon
- Development and fabrication of FET devices using organic semiconductor materials
- Test the method towards different applications in cell culture monitoring

This work is divided in seven chapters.

After this introduction, chapter 2 will present the most important concepts of the cell membrane and the cellular processes from a physical standpoint, the physical basics of inorganic and organic semiconductor materials, the general working principle of field-effect transistor

devices based on inorganic and organic semiconductor materials, and it will introduce the methods to investigate the cell-substrate adhesion.

Chapter 3 will describe silicon-based as well as organic field-effect transistor devices, the measurement setups for recording of the transfer functions (impedance spectra), the chip encapsulation and the chip cleaning protocols, as well as the cell types used in this work.

Chapter 4 will introduce an electrically equivalent circuit (EEC) model to interpret the recorded impedance spectra. Using this EEC model an analytical expression representing the transfer functions will be derived, which can be used to fit the measured impedance spectra and to extract the cell-related parameters of seal resistance and membrane capacitance. Moreover, it was possible to use this EEC model to investigate the effect of the device-related parameters on the impedance spectra, which was utilized to optimize the FET device performance.

Moreover, the usage of silicon-based FET devices to study individual adherent cells by impedance spectroscopy will be discussed. Also time-dependent readout at several different frequencies simultaneously will be described to follow the apoptosis event induced by a chemotherapeutic drug.

Chapter 5 will present the fabrication process of the organic-based FET devices. The typical field-effect behavior of the fabricated organic electrochemical field-effect transistor (OECT) devices, the biocompatible features of the devices as well as the cell adhesion measurements with OECT devices will be discussed.

Chapter 6 will conclude the performed experiments and results and give an outlook for future improvements and application of the introduced technique.

Chapter 2

2 Theoretical principles

In this chapter, the most important concepts of the cell membrane and the cellular processes from a physical standpoint, the physical basics of inorganic and organic semiconductor materials, the working principle of FET devices based on inorganic and organic semiconductor materials, and various methods to investigate the cell-substrate adhesion will be introduced.

2.1 Cells and their principle mechanisms

The cell is the smallest living unit of all organisms. All living cells fall into two categories: prokaryotic and eukaryotic. The distinction is based on whether or not the cell has a nucleus (Hofmann, 2009). The cell consists of a cell membrane, nucleus, mitochondria, Golgi apparatus, endoplasmic reticulum and ribosomes, lysosomes, cytoskeleton (Figure 2-1). They all have dedicated functions in the body or in an organ. The cell membrane contains specific proteins for the exchange of nutrients and other materials with the environment. The nucleus preserves the genetic information encoded in DNA and organized into chromosomes. Mitochondria are the power plants where carbohydrates, fats, and amino acids are oxidized to CO_2 and H_2O. The Golgi apparatus is involved in the processing and packaging of macromolecules for secretion and for delivery to other cellular compartments. The endoplasmic reticulum (ER) is

an organelle where both membrane proteins and lipids are synthesized. Proteins made by the ribosomes of the rough ER pass through the outer ER membrane into the cisternae and can be transported via the Golgi to the periphery of the cell. Lysosomes digest the materials entering the cell via phagocytosis or pinocytosis. The cytoskeleton determines the shape of the cell.

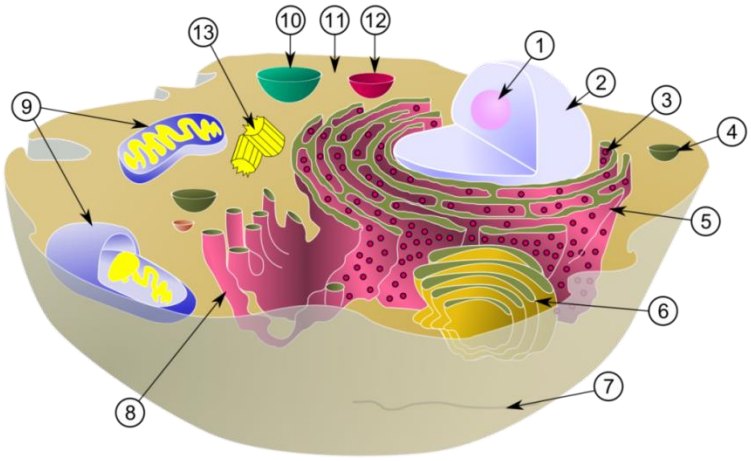

Figure 2-1 Organization of a typical eukaryotic animal cell: 1 Nucleolus 2 Nucleus 3 Ribosome 4 Vesicle 5 Rough endoplasmic reticulum 6 Golgi apparatus 7 Cytoskeleton 8 Smooth endoplasmic reticulum 9 Mitochondrion 10 Vacuole 11 Cytosol 12 Lysosome 13 Centriole The figure was adapted from (http://commons.wikimedia.org/wiki/File:Biological_cell.svg).

From a physical standpoint the cell is a closed compartment filled with electrolyte solution of certain composition and is sourrounded by an electrolyte solution with a different composition. These two compartments are separeted by a thin flexible membrane.

2.2 Cell membrane

Cell membranes are involved in a variety of cellular processes such as cell adhesion, ion conductivity and cell signalling. The cell membrane consists of the phospholipid bilayer with embedded proteins.

The lipid bilayers of cell membranes can be electrically modeled as a sandwich consisting of two layers of a conductor (the plane of the polar lipid heads) separated by a dielectric layer. Surrounding a cell, the lipid bilayer provides a barrier to maintain a different internal environment of ions and macromolecules from the extracellular bathing fluid. Certain types of cells have evolved to respond to particular types of stimuli (electrical, chemical, or mechanical) all with the same basic signal, a transient change in the membrane potential (depolarization of the membrane), followed by a restoration of the resting potential (repolarization).

The cell membrane can be electrically described by an equivalent circuit proposed by Hodgkin and Huxley (Figure 2-2). The lipid bilayer is represented as a capacitance C_M. The ion channels are represented by electrical conductances G_n in series with voltage sources E_n, where n is the specific ion channel (Na^+ and K^+ channels dominate). The conductances G_n can vary with time, depending on whether the ion channels are opened or closed. Leak channels are represented by linear conductances G_L. The leak includes the current of calcium and other ions (Sommerhage, 2011) (Newman, 2008).

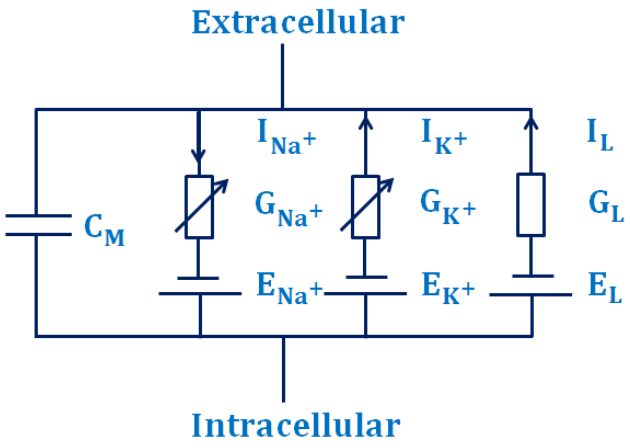

Figure 2-2 The Hodgkin–Huxley equivalent circuit for a cell membrane to describe the electrical behaviour.

2.3 Cell adhesion

There are two types of cellular adhesion, adhesion between adjacent cells (cell-cell adhesion) and adhesion between cells and the extracellular matrix (ECM) (cell-matrix adhesion). Cell

adhesion involves specific biomolecules such as membrane anchors and receptors, extracellular ligands and cytoskeketal components.

Adhesion of the cells to the surfaces is realised through adhesion proteins (e.g. fibronectin, collagen, laminin, vitronectin) using specific cell receptors, called integrins (Lotfi et al., 2013). The cytoplasmic binds to the protein talin, which binds to vinculin. Vinculin associates with α-actinin and is thereby linked to an actin filament.

Focal contacts can relay signals from the extracellular matrix to the cytoskeleton. Several protein kinases are localized to focal contacts and seem to change their activity with the type of the substrate on which they rest. These kinases can regulate the survival, growth, morphology, movement, and differentiation of cells in response to a new environment (Li, 2005).

2.4 Cell apoptosis and necrosis

Apoptosis is the controlled and energy-dependent process of programmed cell death. Apoptosis occurs as a homeostatic mechanism to maintain cell populations in tissues and as a defense mechanism such as in immune reactions or when cells are damaged by disease or noxious agents.

During the apoptosis process, morphological changes including cell shrinkage, membrane blebbing, chromatin condensation and nuclear fragmentation occur (Lowe and Lin, 2000), which can be recognized by light or electron microscopy. The apoptosis process begins with cell shrinkage, by which the cells get smaller in size. The cytoplasm is dense and the organelles are more tightly packed. Pyknosis results from chromatin condensation in the nucleus. The cytoskeleton of the cell breaks up and causes plasma membrane blebbing. Pyknosis is followed by karyorrhexis and separation of cell fragments into apoptotic bodies. Apoptotic bodies consist of cytoplasm with tightly packed organelles with or without a nuclear fragment. These bodies are subsequently phagocytosed and degraded within phagolysosomes (Elmore, 2007). The apoptosis process affects single cells or small clusters of cells. The apoptotic cell appears as a round or oval mass with dark eosinophilic cytoplasm and dense purple nuclear chromatin fragments.

In contrast to apoptosis, necrosis is a toxic, uncontrolled, and passive process, which follows an energy-independent mode of death. Necrosis usually affects large fields of cells. Necrotic cell injury is mediated by two main mechanisms; interference with the energy supply of the cell and direct damage to the cell membranes. Morphological changes that occur with necrosis include cell swelling, formation of cytoplasmic vacuoles, distended endoplasmic reticulum, formation of cytoplasmic blebs, condensed, swollen or ruptured mitochondria, disaggregation and detachment of ribosomes, disrupted organelle membranes, swollen and ruptured lysosomes, and eventually disruption of the cell membrane (Elmore, 2007).

2.5 Methods for investigation of cell-substrate adhesion

Cell-substrate adhesion can be recorded electronically by a technique called Electric Cell-substrate Impedance Sensing (ECIS) on gold electrodes (Lo et al., 1995) (Giaever and Keese, 1991) and by impedance spectroscopy with field-effect transistors (Schäfer et al., 2009). The ECIS approach is well-known for decades and several commercial systems are applied in biomedical research (AppliedBiophysics, http://www.biophysics.com) (ACEA Biosciences, http://www.aceabio.com) (Molecular Devices, http://www.moleculardevices.com). However, due to the sizes of the gold electrodes, a single cell resolution is difficult to realize. The smallest size of the gold electrodes is 50 µm in diameter (Abdurrahman et al., 2007), although 25 µm electrodes can be purchased from some distributors. The downscaling of the gold electrodes is physically limited, due to the fact that the double layer capacitance, which is formed at the metal-liquid interface, dominates the overall system impedance. The recorded currents are so small that cable impedance plays a decisive role in this case (Xiao et al., 2002). An alternative approach, which is intensively studied in this work, is the utilization of open-gate field-effect transistor devices. Transistors benefit from their very high sensitivity to changes in surface potential at the liquid-solid interface and their capability of miniaturization in size. In the following, both methods will be described. Compared to metal microelectrodes FETs have a much smaller capacitance.

2.5.1 Electric Cell-substrate Impedance Sensing

The ECIS approach, which was invented by I. Giaever and R. C. Keese in 1991, is a real-time, impedance-based method to investigate adhesion strength of cells. The ECIS approach has been applied to measure the invasive nature of cancer cells, the barrier function of endothelial cells, in vitro toxicity, and signal transduction involving G protein–coupled receptors for drug discovery (AppliedBiophysics, http://www.biophysics.com).

The ECIS system (Figure 2-3) consists of an eight well cell culture dish, with a small working electrode and a large counter electrode deposited on the bottom of each well, a lock-in amplifier, relays to switch between the different wells, and a personal computer to control the measurements and to store the data (Figure 2-4).

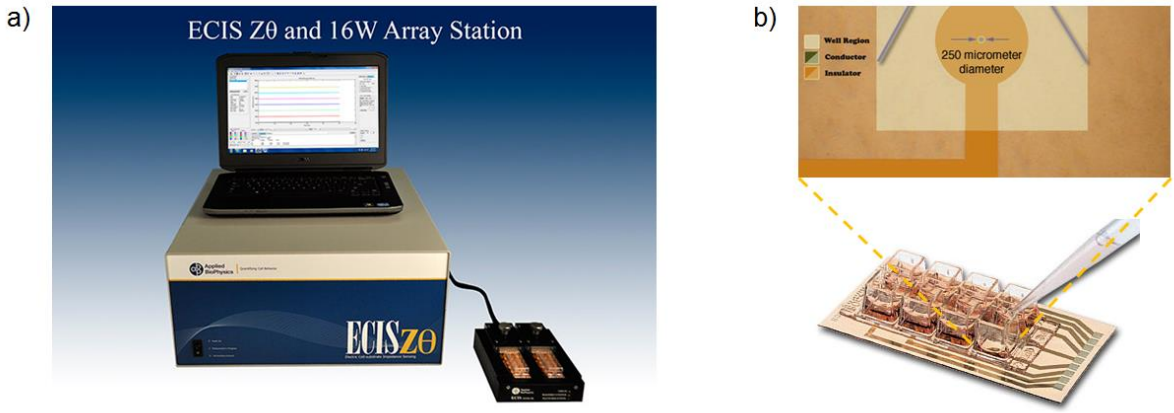

Figure 2-3 a) The ECIS system is composed of a ZΘ system controller, 16 and/or 96 well array station, and a computer with integrated software. The 16 well array station provides electrical contact for two b) 8 well ECIS arrays. Each well contains a single active electrode (250 μm in diameter). The figures were adapted from AppliedBiophysics (http://www.biophysics.com).

An alternating current signal of amplitude 1V and of frequency 4 kHz is applied through a series 1 MΩ resistor to the electrodes. The impedance is calculated from the change in the voltage between the electrodes (Wegener et al., 2000) (Giaever and Keese, 1991).

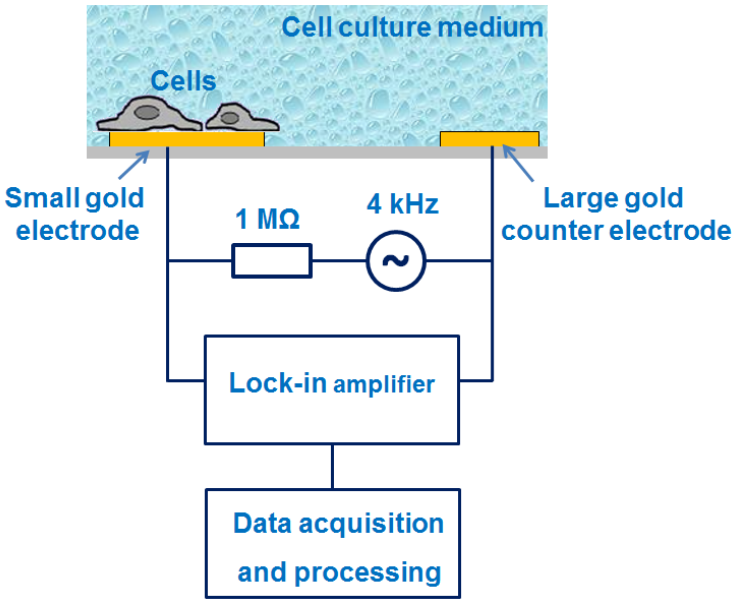

Figure 2-4 Schematic view of the ECIS measurement setup.

In order to calculate the specific impedance of a cell-covered electrode, a model based on the measured specific impedance of a cell-free electrode $Z_n(\nu)$, the specific impedance through the cell layer $Z_m(\nu)$, and the resistivity of the tissue culture medium ρ is used. The commonly used model is based on an earlier publication (Giaever and Keese, 1991). The ionic current flows in the space between the cell and the substratum can be described according to Kirchhoff's law as:

$$\frac{d^2V}{dr^2} + \frac{1}{r}\frac{dV}{dr} - \gamma^2 V + \beta = 0 \tag{2.1}$$

$$\gamma^2 = \frac{\rho}{h}\left(\frac{1}{Z_n} + \frac{1}{Z_m}\right) \tag{2.2}$$

$$\beta = \frac{\rho}{h}\left(\frac{V_n}{Z_n} + \frac{V_m}{Z_m}\right) \tag{2.3}$$

where V_n is the potential of the electrode, V_m the potential measured in the solution outside the cell layer, and h the height of the space between the surface of the cell and the substratum.

The specific impedance for a cell-covered electrode is then given by:

$$\frac{1}{Z_c} = \frac{1}{Z_n}\left(\frac{Z_n}{Z_n+Z_m} + \frac{\frac{Z_n}{Z_n+Z_m}}{\frac{i\gamma r_c I_0(\gamma r_c)}{2\ I_1(\gamma r_c)} + 2R_b\left(\frac{1}{Z_n}+\frac{1}{Z_m}\right)}\right) \tag{2.4}$$

where I_0 and I_1 are modified Bessel functions of the first kind of order 0 and 1, $i = \sqrt{-1}$, and R_b the resistance between the cells for a unit area.

For data interpretation the model can then be fitted and extracred.

$$\gamma r_c = r_c \sqrt{\frac{\rho}{h}\left(\frac{1}{Z_n} + \frac{1}{Z_m}\right)} = \alpha \sqrt{\frac{1}{Z_n} + \frac{1}{Z_m}} \tag{2.5}$$

For further study of this topic the interested reader should refer to the original publication (Giaever and Keese, 1991) (Giaever and Keese, 1993).

2.5.2 Transistor transfer function

Another, much newer approach for cell adhesion detection is based on the recording of the electronic transfer function of the ion-sensitive field-effect transistor (ISFET) devices. This method was pioneered in the group of Bergveld in 1989 (Schasfoort et al., 1989) for detection of protein layers and later was applied to other biomolecules (Kharitonov et al., 2001) (Antonisse et al., 2000) used for testing of encapsulation integrity (Kruise et al., 1992). The method was then firstly applied to cell-substrate arrays in our former group at the research center Jülich, Germany (Schäfer et al., 2009). In this section a simple model is presented based on (Kharitonov et al., 2001) (Antonisse et al., 2000) to explain the main effects.

The attached cell to the gate of the ISFET device can be represented by the electrically equivalent circuit shown in Figure 2-5. This circuit consists of the ISFET device element, the membrane element and the electrolyte solution resistance. The ISFET device element consists of the silicon electrode resistance R_{Si}, the space charge capacitance C_{sc}, and the gate oxide capacitance C_{ox}. The membrane element includes the bulk membrane properties (the bulk membrane capacitance C_M and the bulk membrane resistance R_M) and the interfacial properties of the membrane (the double-layer capacitance at the membrane interface C_{dl}, the charge transfer resistance at the membrane interface R_{ct} and the Warburg impedance W).

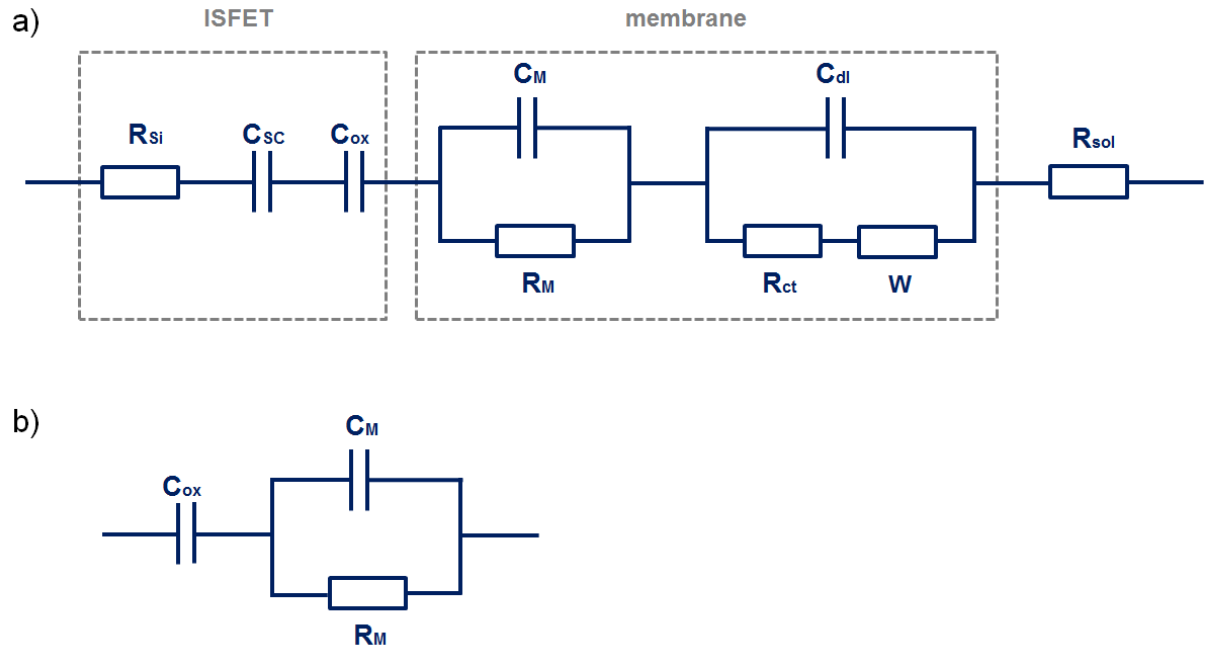

Figure 2-5 a) The equivalent circuit of the attached cell to the gate of the ISFET device. All elements of the circuit are described in the text. b) Simplified equivalent circuit of the attached cell to the gate of the ISFET device.

In the inversion regime, the space charge capacitance is smaller than the gate oxide capacitance and can therefore be neglected. Also, the silicon electrode resistance as well as the resistance of the electrolyte solution, which are small in comparison to the membrane resistance, can be neglected. At higher frequencies (≥5 Hz), the interfacial properties of the membrane have no important contribution to the impedance features of the system. Hence, the equivalent circuit shown in Figure 2-5a can be simplified to the equivalent circuit shown in Figure 2-5b consisting of three elements only.

The voltage applied between the gate and the source of the ISFET V_{GS} device leads to a drain-source current I_{DS}. The output voltage V_{out} is related to the drain-source current as follows:

$$V_{out} = -RI_{DS} = -Rg_mV_{GS} \tag{2.6}$$

where R is the electrical resistance in the measuring circuit and g_m the transconductance of the ISFET device.

When a cell membrane is attached to the gate of the ISFET device, the applied voltage between the gate and the source of the ISFET device V_{GS} is divided over the cell membrane and

the gate oxide layer. Therefore, the effective potential difference between the gate and the source is smaller than the applied voltage. The introduced transfer function H(j*w*) relates to the applied voltage and the output voltage as follows:

$$V_{out} = -Rg_m H(jw) V_{GS} \tag{2.7}$$

$$H(jw) = \frac{1+jwR_M C_M}{1+jwR_M(C_M+C_{ox})} \tag{2.8}$$

The frequency-dependent transfer function is defined by the three elements of the simplified equivalent circuit (Figure 2-5b). The theoretical dependence of the transfer function on the frequency *w* as well as the method to extrat the time constants τ_1 and τ_2 is shown in Figure 2-6.

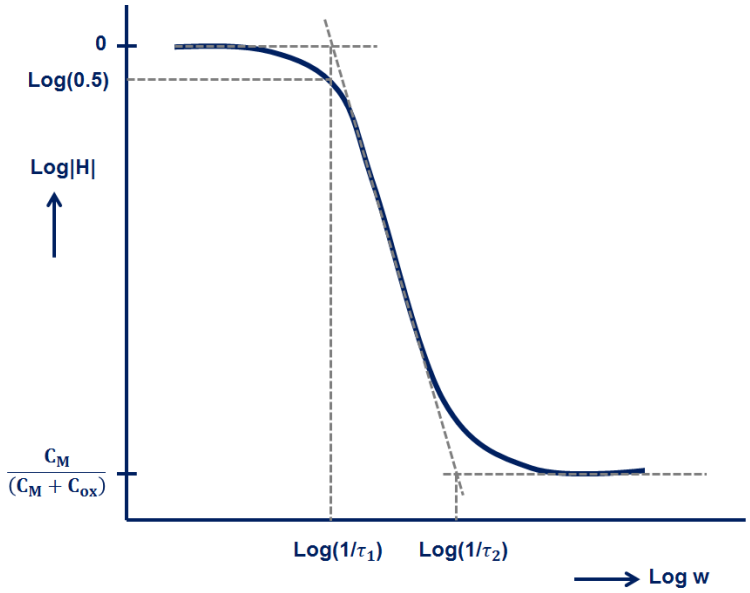

Figure 2-6 Theoretical transfer function and the graphical method to extract the time constants.

At low frequencies, the gate oxide capacitance is higher than the membrane capacitance, therefore the membrane capacitance can be neglected (equation (2.9)). At high frequencies, because of the dominated contribution of the membrane resistance and the membrane capacitance the gate oxide capacitance can be neglected (equation (2.10)):

$$\tau_1 = R_M(C_M + C_{ox}) \approx R_M C_{ox} \tag{2.9}$$

$$\tau_2 = R_M C_M \tag{2.10}$$

In this thesis (chapter 4) a much more detailed model was developed and it was shown, that in reality the recorded spectra are not so simple and many other parameters are influencing the recordings.

2.6 Transimpedance amplifier circuit

One central element influencing the recorded spectra is the choice of the first amplifier circuit. It is well known that the current of the ISFET device is responsive to changes in the surface potential of the electrolyte-exposed gate oxide. In order to measure this, a circuit is required, which converts the drain-source current I_{DS} of the transistor into a voltage, which can be further amplified and digitized. A simple circuit, which fulfills this task, is the transimpedance amplifier (Figure 2-7). The transimpedance amplifier is implemented by an operational amplifier (OPA) and a feedback resistor $R_{feedback}$.

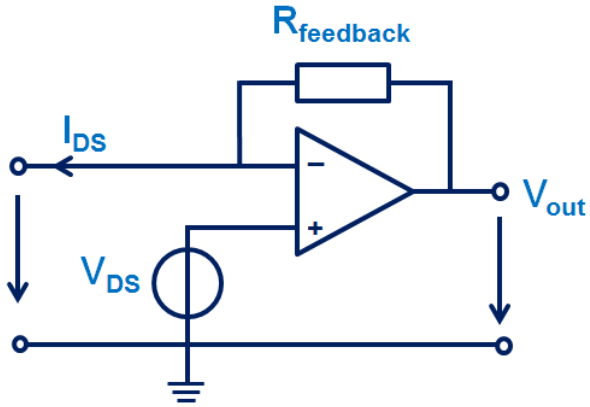

Figure 2-7 The transimpedance amplifier is implemented by an operational amplifier, a feedback resistor $R_{feedback}$ and a voltage source.

The output voltage V_{out} of the circuit shown in Figure 2-7 is calculated by:

$$V_{out} = V_{DS} + R_{feedback} I_{DS} \tag{2.11}$$

The frequency spectrum of this circuit is influenced by the choice of the OPA and the size of $R_{feedback}$. It is known that for such circuits a swing effect can occur, which can be observed when recording of the transfer functions. This could be damped by a feedback capacitor in parallel with the feedback resistor. However, in order to not loose too much information from the spectra we refrained from this.

2.7 Point contact model

The point contact model was developed by (Regehr et al., 1989) and was later applied to describe the electrical contact between cell and transistor for recording of action potentials from neurons and muscle cells. The schematic view of this model is shown in Figure 2-8. It includes a patch pipette, which is used to measure the intracellular voltage V_M. The patch pipette is represented by the pipette capacitance C_P and series resistance of pipette R_S. The cell is divided into the free membrane (FM) and the junction membrane (JM), each represented by Hodgkin-Huxley elements (Hodgkin and Huxley, 1952). The cleft between cell and transistor can in a first approach be represented by a seal resistor R_{seal}, respectively a junction conductance G_J. In addition, the model contains the junction potential V_J and the voltage applied to the source and the ground in the electrolyte solution.

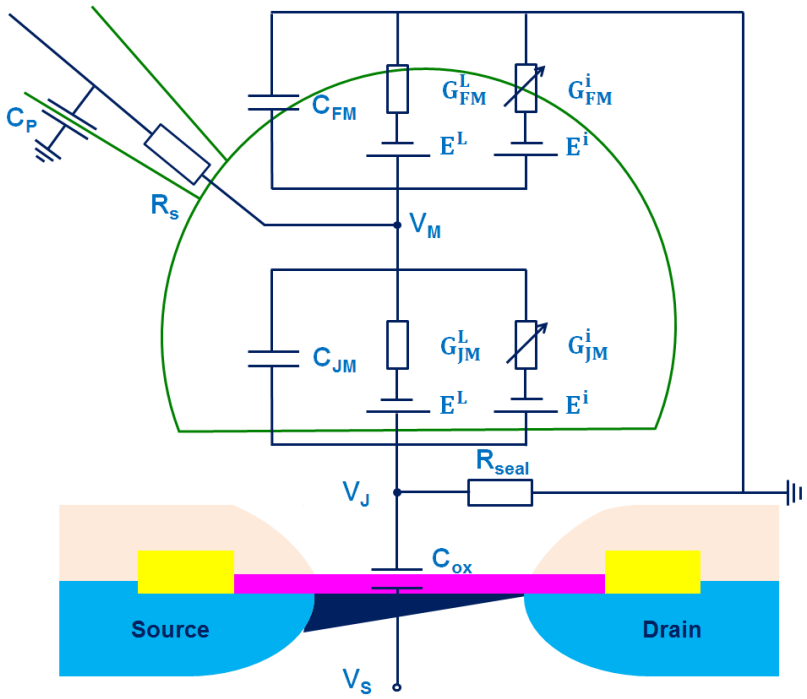

Figure 2-8 The point contact model for a patch-clamp contacted cell on top of a field-effect transistor device.

Such models were usually applied to explain fundamental experiments for cell-sensor contacts. In such cases an individual cell was contacted by a patch-clamp electrode in whole cell mode.

The junction potential for this particular configuration can be related to the intracellular membrane potential by following Kirchhoff's law in the point of contact:

$$C_{ox}\frac{dV_J(t)}{dt} + G_J V_J(t) = C_{JM}\frac{d\left(V_M(t)-V_J(t)\right)}{dt} + \sum_i G^i_{JM}\left(V_M(t) - V_J(t) - E^i_{J0}\right) \qquad (2.12)$$

where C_{ox} is the gate oxide capacitance, G^i_{JM} the conductivity for the ions of the junction membrane, and E^i_{J0} the reversal potential of the ions i in the cleft.

For modelling of recorded data this expression can be simplified (Ingebrandt et al., 2005). A first approximation is that the capacitive current tends towards zero $\left(C_{ox}\frac{dV_J(t)}{dt} \approx 0\right)$. This is of course valid when dealing with small frequencies. The junction potential is small compared to the membrane potential $\left(V_J(t) \ll V_M(t)\right)$ and can be neglected in the sum terms. The ion

concentration differences between cleft and the electrolyte solution can be neglected as well $\left(E_{J0}^{i} = E_{0}^{i}\right)$. Therefore, the equation (2.12) can be rewritten:

$$V_J(t) = R_J\left(C_{JM}\frac{dV_M(t)}{dt} + \sum_i G_{JM}^{i}\left(V_M(t) - E_0^{i}\right)\right) \quad (2.13)$$

This equation describes the junction potential in a first approximation (Ingebrandt et al., 2005).

2.8 Basics of semiconductors

Solid-state microelectronic devices, e.g. transistors, are fabricated from semiconductors. The two important semiconductors are silicon (Si) and germanium (Ge), while silicon is the most widely used semiconductor material for fabrication of modern devices. In this chapter, the fundamentals of conduction in semiconductors will be described.

A semiconductor is a material, which electrical conductivity lies between a conductor and an insulator. Typically, semiconductors have four valence electrons, which can contribute to the electrical conductivity of a material. When the valence electron gains sufficient energy from some outside source such as thermal energy, it can break away from the parent atom and become a free electron. When an electric field is applied to a material, the free electrons experience a net electrical force, which cause them to move. The movement of the electrons due to the applied electric field is called the electric drift current. The electrons have a certain mobility in the material μ_e. In the linear regime of transistors this effect is dominating over diffusion effects. This was the case for all experiments conducted in this thesis.

Semiconductors are mainly classified into two categories: intrinsic and extrinsic. An intrinsic semiconductor is a pure semiconductor without any dopant molecules. When a semiconductor is doped with impurities, the semiconductor becomes extrinsic.

When an electron in a semiconductor gets sufficient energy, it can go to the conduction band and leave behind a hole. Like free electrons, holes have a mobility μ_h and exhibit a drift velosity v_h, which produces a conduction current J under the influence of an applied eletric field E. For this total current, unlike as in metals, both charge carrier types need to be taken in account:

$$J = \rho_e v_e + \rho_h v_h = n_i(\mu_e + \mu_h)qE = \sigma E \quad (2.14)$$

The conductivity σ of the intrinsic semiconductor is given by:

$$\sigma = n_i(\mu_e + \mu_h)q \quad (2.15)$$

where n_i is the intrinsic concentrations, μ_e the electron mobility and μ_h the hole mobility. Because of the small number of free electrons, the conductivity of an intrinsic semiconductor is much lower than that of a metal. The conductivity can be increased by adding certain impurities. There are two classes of impurities: donor impurities (n-type semiconductor) and acceptor impurities (p-type semiconductor).

An intrinsic semiconductor doped with a donor impurity (in the case of silicon phosphorus (P) or arsenic (As)) is called an n-type semiconductor. In Figure 2-9a it is shown that a silicon atom in the crystal lattice is replaced by a phosphorus atom (donor). Each donor atom has five valence electrons. The phosphorus atom forms covalent bonds with its four neighboring silicon atoms. The fifth valence electron becomes a free electron, which can easily get activated into the conduction band. The number of free electrons donated by the donor atoms is much greater than the number of free electrons and holes in the intrinsic semiconductor. Therefore, the conductivity of the n-type semiconductor is greater that of the intrinsic semiconductor, which can be precisely controlled by the doping concentration. The semiconductor is called n-type because the majority carriers have a negative charge.

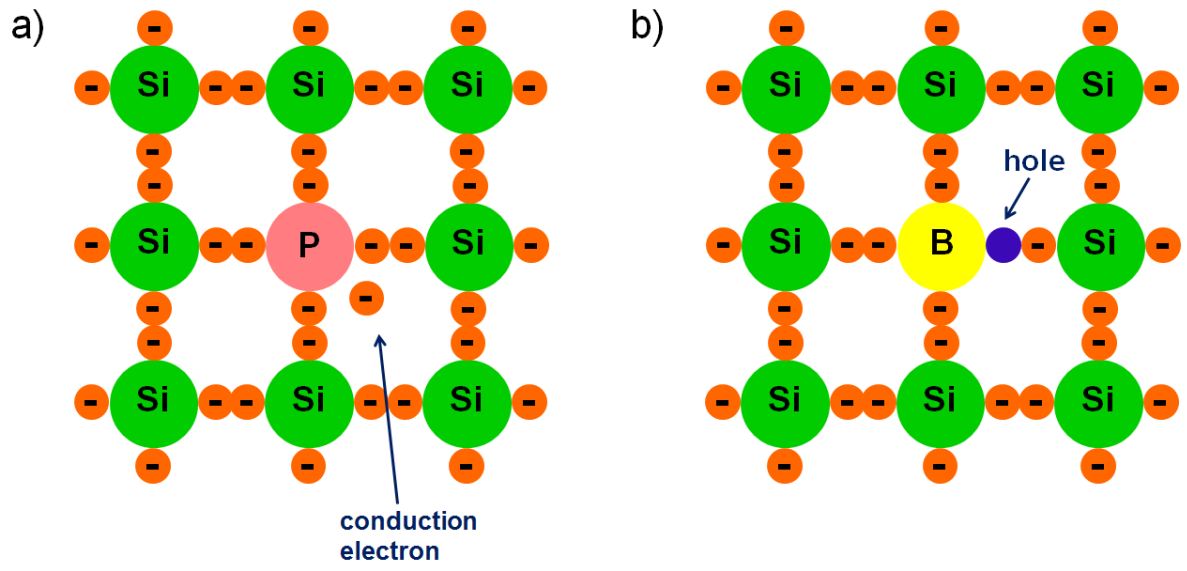

Figure 2-9 Schematic view of a) an n-type semiconductor and b) a p-type semiconductor.

An intrinsic semiconductor doped with an acceptor impurity (in the case of silicon boron (B) or aluminium (Al)) is called a p-type semiconductor. In Figure 2-9b it is shown that an atom in the silicon crystal lattice is replaced by a boron atom (acceptor). Each acceptor atom has three valence electrons. To form four covalent bonds around the boron, one of the electrons in the silicon valence band can easily get captured to the valence shell of one of the acceptor atoms, leaving a hole in the remaining silicon lattice behind. Again the number of holes created by the acceptor atoms is much greater than the number of free electrons and holes in the intrinsic semiconductor. Therefore, the conductivity of the p-type semiconductor is greater that of the intrinsic semiconductor. The semiconductor is called p-type because the majority carriers have a positive charge.

The conduction current density in a doped semiconductor is given by:

$$J= (n\mu_e + p\mu_h)qE = \sigma E \quad (2.16)$$

The conductivity σ of the extrinsic semiconductor is given by:

$$\sigma=(n\mu_e + p\mu_h)q \quad (2.17)$$

where n and p are the electron concentration and the hole concentration, respectively.

2.8.1 Fermi-Dirac distribution function and Fermi level

The probability that an electronic state with energy E is occupied by an electron is given by the Fermi-Dirac distribution function f(E) (Sze, 2002) (Sze, 1981):

$$f(E)=\frac{1}{1+exp((E-E_F)/kT)} \quad (2.18)$$

where k is the Boltzmann constant, T the absolute temperature, and E_F the Fermi energy. The Fermi energy is the energy at which the probability of occupation by an electron is exactly one half.

The electron density n (the number of electrons per unit volume) in the conduction band is given by:

$$n = N_C\, exp\left(-\frac{E_C-E_F}{kT}\right) \quad (2.19)$$

where N_C is the effective density of states in the conduction band and given by:

$$N_C = 2\left(\frac{2\pi m_n kT}{h^2}\right)^{3/2} \tag{2.20}$$

where m_n is the electron effective masse and h the Planck constant.

For silicon N_C is 2.8×10^{19} cm^{-3} at room temperature (300 K).

The hole density p in the valence band is given by:

$$p = N_V \exp\left(-\frac{E_F - E_V}{kT}\right) \tag{2.21}$$

where N_V is the effective density of states in the valence band and given by:

$$N_V = 2\left(\frac{2\pi m_p kT}{h^2}\right)^{3/2} \tag{2.22}$$

where m_p is the hole effective masse and h the Planck constant.

For silicon N_V is 1.04×10^{19} cm^{-3} at room temperature (300 K).

For an intrinsic semiconductor, the number of electrons in the conduction band is equal to the number of holes in the valence band. Hence, the Fermi level of an intrinsic semiconductor lies approximately in the middle of the bandgap. For an n-type semiconductor, there are more electrons in the conduction band than there are holes in the valence band. As a result the probability of finding an electron near the conduction band is larger than the probability of finding a hole near the valence band. Therefore, the Fermi level lies closer to the conduction band (Figure 2-10a). For a p-type semiconductor, there are more holes in the valence band than there are electrons in the conduction band. This means that the probability of finding an electron near the conduction band is smaller than the probability of finding a hole near the valence band. Therefore, the Fermi level lies closer to the valence band (Figure 2-10b). Hence, the Fermi-energy has an important influence on the electrical properties of a semiconductor material.

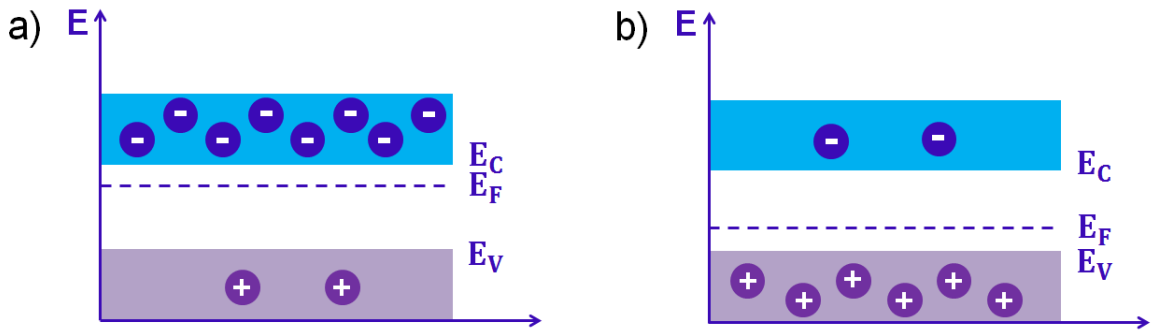

Figure 2-10 Fermi level E_F lies closer a) to the conduction band E_C for an n-type semiconductor and b) to the valence band E_V for a p-type semiconductor.

2.9 Metal-oxide-semiconductor field-effect transistor

The field-effect transistor is a transistor that uses an electric field to control the conductivity of a channel of one type of charge carrier in a semiconductor material. The most widely used type of the field-effect transistors is the metal-oxide-semiconductor field-effect transistor (MOSFET). The function of the transistor will be now discussed by considering the example of a p-channel MOSFET. A schematical view of a p-channel MOSFET is shown in Figure 2-11. A p-type MOSFET is a three-terminal device, which consists of an n-type semiconductor substrate and two doped p-type semiconductor regions called source and drain. A thin layer of oxide, called the gate oxide, is grown on top of the n-type substrate between source and drain. The metal contact separated from the semiconductor by the insulating gate oxide is called the gate.

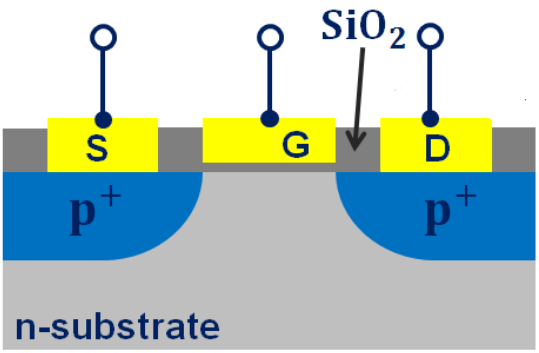

Figure 2-11 A p-type MOSFET is a three-terminal device, which consists of an n-type semiconductor substrate and two doped p-type semiconductor regions (source (S) and drain (D)). The metal contact is separated from the semiconductor by the gate oxide (SiO_2) and is called the gate (G).

When no voltage is applied to the gate, only a leakage current can flow from source to drain. This current is driven by electron diffusion through the channel and this conduction region is called subthreshold region of the transistor. When a negative voltage is applied to the gate, a surface inversion layer (channel) will be formed between the two p-doped regions. The source and drain are then connected by a conducting p-channel through which a large drift current can flow (Figure 2-12). The conductance of this channel can be modulated by varying the gate voltage.

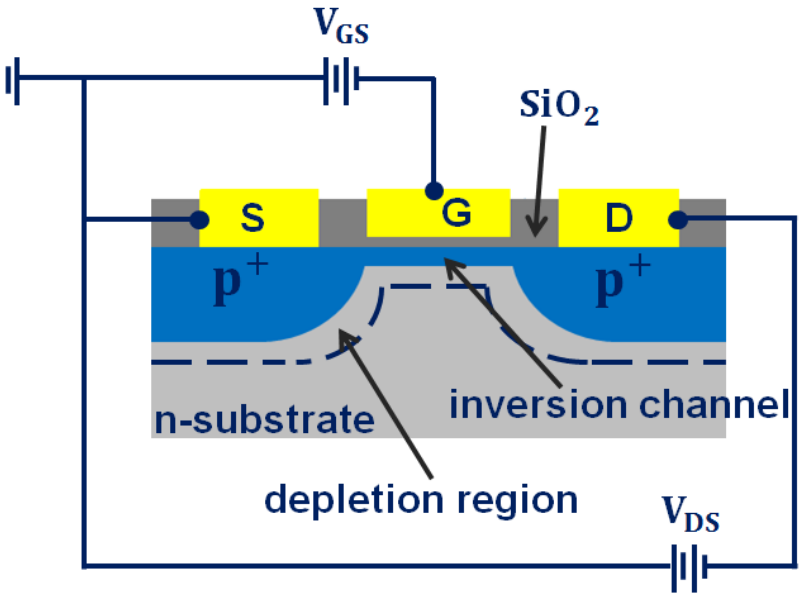

Figure 2-12 When a negative bias (V_{GS}) will be applied to the gate, an inversion channel will be formed between the two p^+ regions.

When a small drain voltage (V_{DS}) is applied, the charge carriers (holes) will flow from the source to the drain through the conducting channel. The drain current (I_{DS}) is proportional to the drain voltage. This called the linear region of the transistor operation.

When the drain voltage increases, it reaches a point at which the width of the channel is reduced to zero. This point is called the pinch-off point (Figure 2-13).

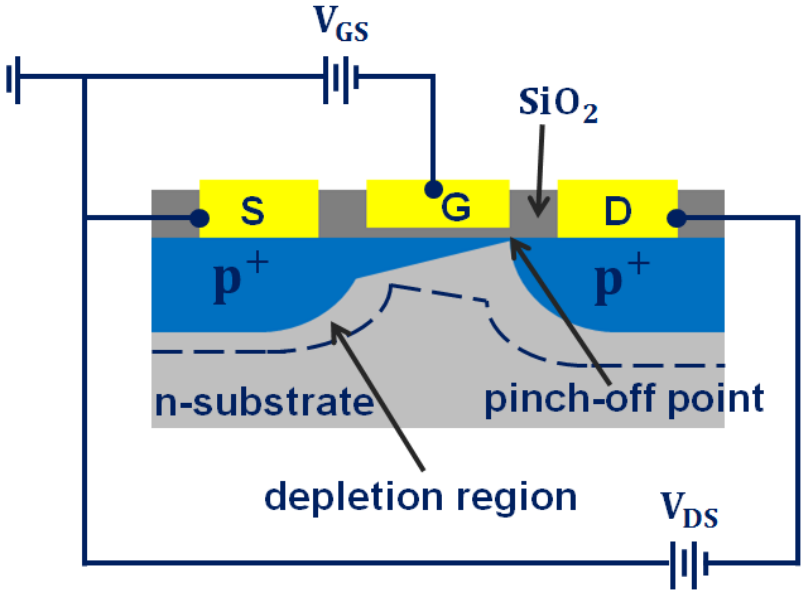

Figure 2-13 Schematic view of a p-channel MOSFET device in saturation region.

The total charge induced in the semiconductor per unit area Q_s at a distance x from the source is given by (Sze, 2002) (Sze, 1981):

$$Q_s(x) = -C_{ox}[V_{GS} - \Psi_0(x)] \tag{2.23}$$

where $\Psi_0(x)$ is the surface potential at *x* and $C_{ox}=\varepsilon_{ox}/d$ is the gate capacitance per unit area. The charge in the inversion layer Q_n is given by:

$$Q_n(x) = -C_{ox}[V_{GS} - \Psi_0(x)] - Q_{sc}(x) \tag{2.24}$$

where Q_{sc} is the charge in the surface depletion region, which is given by:

$$Q_{sc}(x) = -\sqrt{2\varepsilon q N_A[V(x) + 2\Phi_F]} \tag{2.25}$$

where ε is the permittivity, q is the elementary charge, N_A is the acceptor concentrations, V(x) is the reverse bias between the point *x* and the source electrode, and Φ_F the potential difference between the actual Fermi level in the silicon between source and drain and the Fermi level in the intrinsic silicon.

Substituting equation (2.25) in (2.24) and by assumption that $\Psi_0(x) = V(x) + 2\Phi_F$ yields:

$$Q_n(x) = -C_{ox}[V_{GS} - V(x) - 2\Phi_F] + \sqrt{2\varepsilon q N_A[V(x) + 2\Phi_F]} \tag{2.26}$$

The channel conductance g is given by:

$$g = \mu \frac{W}{L} |Q_n| \tag{2.27}$$

where $|Q_n|$ is the total charge per unit area in the inversion layer.

The channel resistance R of an elemental section dx is given by:

$$dR = \frac{dx}{W\mu|Q_n(x)|} \tag{2.28}$$

and the voltage drop across the elemental section is given by:

$$dV = I_{DS}dR = \frac{I_{DS}dx}{W\mu|Q_n(x)|} \tag{2.29}$$

where I_{DS} is the drain-source current. Substituting equation (2.26) into equation (2.29) and integrating from the source to the drain yields:

$$I_{DS} = \mu \frac{W}{L} C_{ox} \left\{ \left(V_{GS} - 2\Phi_F - \frac{V_{DS}}{2} \right) V_{DS} - \frac{2}{3} \frac{\sqrt{2\varepsilon q N_A}}{C_{ox}} \left[(V_{DS} + 2\Phi_F)^{3/2} - (2\Phi_F)^{3/2} \right] \right\} \tag{2.30}$$

For the case of a small drain-source voltage V_{DS} ($V_{DS} \ll (V_{GS} - V_{Th})$) equation (2.30) reduces to:

$$I_{DS} = \mu \frac{W}{L} C_{ox}(V_{GS} - V_{Th})V_{DS} \tag{2.31}$$

where V_{Th} is the threshold voltage given by:

$$V_{Th} = \frac{\sqrt{2\varepsilon q N_A (2\Phi_F)}}{C_{ox}} + 2\Phi_F \tag{2.32}$$

The transconductance g_m is given by:

$$g_m = \frac{dI_{DS}}{dV_{GS}} = \mu \frac{W}{L} C_{ox} V_{DS} \tag{2.33}$$

For drain-source voltages larger than the drain-source voltage at the pinch-off point V_{Dsat} we have the saturation region:

$$V_{Dsat} = V_{GS} - 2\Phi_F + \frac{\varepsilon q N_A}{C_{ox}^2}\left(1 - \sqrt{1 + \frac{2V_{GS}C_{ox}^2}{\varepsilon q N_A}}\right) \tag{2.34}$$

In this saturation region the drain-source current I_{Dsat} is given by:

$$I_{Dsat} = \mu \frac{W}{2L} C_{ox}(V_{GS} - V_{Th})^2 \tag{2.35}$$

The transconductance in this region g_m is then:

$$g_m = \mu \frac{W}{L} C_{ox}(V_{GS} - V_{Th}) \tag{2.36}$$

Throughout this thesis the sensors were always operated in this saturation region. Equations (2.35) and (2.36) are therefore important for later modelling of the recordings.

2.10 Ion-sensitive field-effect transistor

The ion-sensitive field-effect transistor (ISFET) was developed from the MOSFET by replacing the metal gate electrode with a liquid solution and a reference electrode (Figure 2-14) (Bergveld, 2003). Therefore, a very good and dense passivation layer on the source and drain contact lines is required for a reliable operation of the devices in the different electrolyte solutions.

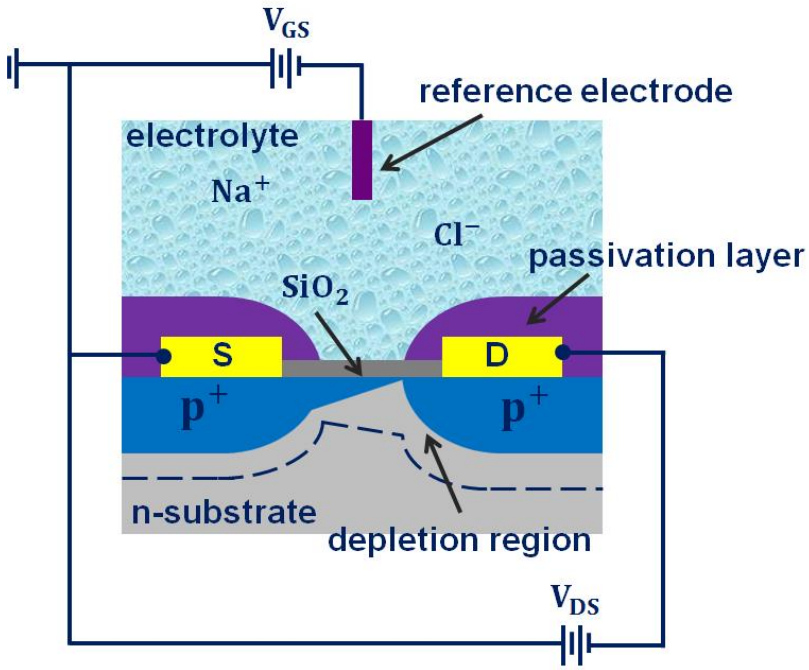

Figure 2-14 Schematic view of a p-channel ISFET device in saturation region. The metal gate electrode is replaced by a liquid solution (electrolyte) and a reference electrode immersed in the electrolyte.

The drain-source current I_{DS} in the unsaturated region is given by:

$$I_{DS} = \mu \frac{W}{L} C_{ox} \left\{ \left(V_{GS} - \left(E_{ref} - \Psi_0 + \chi_{sol} - \frac{\Psi_{Si}}{q} - \frac{Q_{SS}+Q_{ox}}{C_{ox}} - \frac{Q_B}{C_{ox}} + 2\Phi_F \right) \right) V_{DS} - \frac{1}{2} V_{DS}^2 \right\} \quad (2.37)$$

where μ is the average electron mobiliy in the channel, W the width of the gate, L the length of the gate, C_{ox} the capacitance of the gate oxide, E_{ref} the contribution of the reference electrode, Ψ_0 the electrostatic potential at the surface, χ_{sol} the surface dipole potential of the solution, Ψ_{Si} the silicon electron work function, q the elementary charge, Q_{SS} the charges located in surface states and interface states, Q_{ox} the charges located in the oxide, Q_B the depletion charge, and Φ_F the potential difference between the Fermi levels of the doped and the intrinsic silicon. All parameters are constant except the electrostatic potential Ψ_0 at the surface. Therefore, changes in the drain-source current I_{DS} are attributed to changes in the electrostatic potential (van Hal et al., 1995).

The threshold voltage of a MOSFET is determined by material properties such as the work-function and charge accumulation. It is therefore composed of much less parameters. The

threshold voltage of an ISFET contains terms which reflect the interfaces between the liquid and the gate oxide on the one side and the liquid and the reference electrode at the other side.

$$V_{Th} = E_{ref} - \Psi_0 + \chi_{sol} - \frac{\Psi_{Si}}{q} - \frac{Q_{SS}+Q_{ox}}{C_{ox}} - \frac{Q_B}{C_{ox}} + 2\Phi_F \qquad (2.38)$$

Compared to equation (2.32) this is a more complicated expression. For ISFETs, however, these interface effects are explained for sensing purposes.

2.10.1 The oxide-electrolyte interface

The surface of silicon dioxide contains SiOH groups, which may donate or accept a proton from the solution, leaving a negatively charged or a positively charged surface group respectively. The site-binding model describes the equilibrium between the amphoteric SiOH surface sites and the H^+ ions in the solution (Bergveld, 2003).

$SiOH \leftrightarrow SiO^- + H_B^+$

$SiOH_2^+ \leftrightarrow SiOH + H_B^+$

where H_B^+ are the protons in the bulk solution (van Hal et al., 1995) (Bergveld, 2003).

The activity of the bulk protons $a_{H_B^+}$ is related to the activity of the protons in the direct vicinity of the oxide surface $a_{H_S^+}$:

$$a_{H_S^+} = a_{H_B^+} exp\left(-{}^{q\Psi_o}/_{kT}\right) \qquad (2.39)$$

The relation between the activity of the protons at the oxide surface $a_{H_S^+}$ and the surface charge density σ_0 is given in terms of the total number of available sites N_S and the intrinsic dissociation constants K_a and K_b:

$$\sigma_0 = qN_S\left(\frac{a_{H_S^+}^2 - K_aK_b}{K_aK_b + K_b a_{H_S^+} + a_{H_S^+}^2}\right) \qquad (2.40)$$

The effect of a small change in the surface proton activity on the surface charge density is given by:

$$\frac{d\sigma_0}{dpH_S} = -q\frac{dB}{dpH_S} = -q\beta_{int} \tag{2.41}$$

where the change in $a_{H_S^+}$ is expressed in its corresponding pH_S, the resulting change in σ_0 in the change in the net number B of basic groups and β_{int} is the buffer capacity of the oxide surface.

The two opposite charges, the surface charge σ_0 and the charge in the electrolyte σ_{dl}, form the integral double-layer capacitance $C_{dl,i}$:

$$\sigma_{dl} = -\sigma_0 = -C_{dl,i}\Psi_0 \tag{2.42}$$

The integral double-layer capacitance $C_{dl,i}$ can be calculated using the Gouy-Chapman-Stern model (van Hal et al., 1995) (Bergveld, 2003). In this model, the double-layer capacitance comprises a series network of a Helmholtz-layer capacitance (the Stern capacitance) and a diffuse–layer capacitance.

The charge in the diffuse layer σ_{dl} is given by:

$$\sigma_{dl} = -\sqrt{8kT\varepsilon_r\varepsilon_0 n^0}\,\sinh\left(\frac{zq\Psi_1}{2kT}\right) \tag{2.43}$$

where Ψ_1 is the potential at the distance x_H, a plane of closest approach for the centres of the ions, n^0 the concentrations of each ion in the bulk solution in number, z the valence of the ions.

The difference between the potential Ψ_1 at x_H and the surface potential Ψ_0 is the potential difference across the Stern capacitance C_{Stern}:

$$\Psi_1 = \Psi_0 - \frac{\sigma_0}{C_{Stern}} = \Psi_0 - \frac{\sigma_0 x_H}{\varepsilon_r\varepsilon_0} \tag{2.44}$$

With equations (2.43) and (2.44), the integral double-layer capacitance can be calculated as a function of Ψ_0 and the electrolyte concentration:

$$\frac{d\sigma_0}{d\Psi_0} = -\frac{d\sigma_{dl}}{d\Psi_0} = C_{dif} \tag{2.45}$$

where C_{dif} is the differential double-layer capacitance.

$$\frac{1}{C_{dif}} = \frac{d\Psi_0}{d\sigma_0} = \frac{1}{C_{Stern}} + \frac{1}{\sqrt{\frac{2\varepsilon_r\varepsilon_0 z^2 q^2 n^0}{kT}}\cosh\left(\frac{zq\Psi_1}{2kT}\right)} \tag{2.46}$$

Combining equations (2.41) and (2.45) shows the effect of a small change in the surface pH (pH_S) on the change in the surface potential:

$$\frac{d\Psi_0}{dpH_S} = \frac{d\Psi_0}{d\sigma_0} \cdot \frac{d\sigma_0}{dpH_S} = \frac{-q\beta_{int}}{C_{dif}} \tag{2.47}$$

The general expression for the pH sensitivity of an ISFET is given by:

$$\frac{d\Psi_0}{dpH_B} = -2.3\frac{kT}{q}\alpha \tag{2.48}$$

with

$$\alpha = \frac{1}{1+\frac{2.3kTC_{dif}}{q^2\beta_{int}}} \tag{2.49}$$

where α is a dimensionless sensitivity parameter that varies between 0 and 1. If α=1 meaning an ideal pH sensor, the ISFET has a sensitivity of − 59.2 mV/pH at 298 K, which is the maximum achievable sensitivity (Bergveld, 2003).

For the experiments done in this thesis always physiological buffer solutions were used. In this case the double layer capacitance becomes large compared to the capacitance of the gate oxide. Therefore the double layer capacitance could be excluded for the modelling of the spectra in chapter 4.

2.11 Organic semiconductor materials

Organic semiconductors are generally divided into semiconducting small molecules and organic polymers (Brütting and Rieß, 2008) (Brütting, 2005). Both have a conjugated π-electron system. This exists if in a hydrocarbon double or triple bonds between the carbon atoms occur. The simplest instance is the ethylene molecule, which has a double bond between the carbons. A double bond consists of one σ bond and one π bond. In ethylene each carbon atom has three sp^2 orbitals, which is the combination of one s-orbitals with only two p-orbitals (p_x and p_y), and one p orbital. The three sp^2 orbitals lie in a plane with an angle of 120°. By overlapping of two of the sp^2 orbitals forms a σ bond while two p_z orbitals together form a π bond.

The π bond is significantly weaker than the σ bond. Consequently, for unsaturated hydrocarbons the energy gap between the Highest Occupied Molecular Orbital (HOMO) and the Lowest Unoccupied Molecular Orbital (LUMO) is significantly smaller than for saturated bonds. Typical values of this energy gap lie in the range from 1.5 to 3 eV. Organic semiconductors are van-der-Waals bonded in comparison to covalently bonded inorganic semiconductors. Usually, the electronic excited states are located on one molecule, what leads to peculiarities in optical features and charge carrier transport. The lowest optical transition is the excitation of an electron from the occupied π orbital into an unoccupied π* orbital (Figure 2-15). As a result, the emerged electron-hole pair is strongly bound and is located on one and the same molecule, which is denoted as Frenkel exciton.

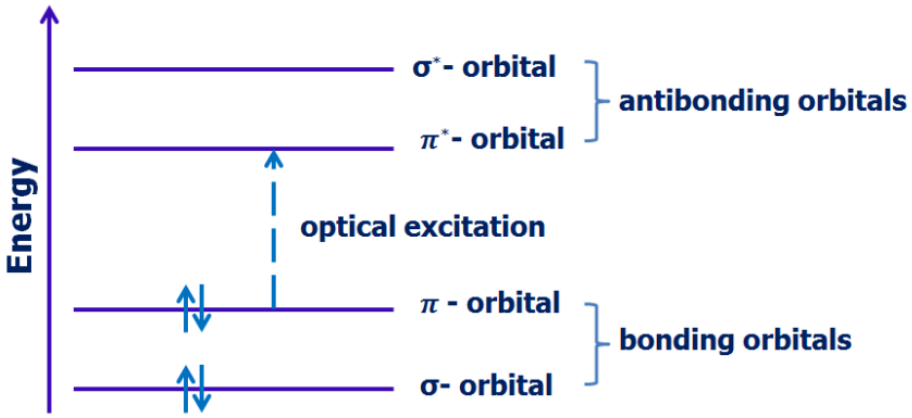

Figure 2-15 Energy level scheme of a π conjugated molecule. The lowest electronic excitation is between the bonding π orbital and the antibonding **π*** orbital.

The binding energy of this exciton is typically 0.5 eV. This value is large in contrast to the thermal energy at room temperature so that the absorption of light in organic semiconductors leads initially to Frenkel exciton. In order to separate the excitons, an electric field must remove the positive and negative charges as far from each other that the Coulomb force will be smaller than the thermal energy. Beside excitons in organic semiconductors there are also charged states, which are movable and thus allow electrical current flow. However, this charge carrier transport is by many orders smaller compared to inorganic semiconductors.

Organic semiconductors show lattice vibrations at relatively small energy levels, which are excited much stronger as in inorganic semiconductors and contribute to the distribution of the charge carriers.

In addition, there are well-defined spin states in organic semiconductors. The ground state is a singlet state with total spin 0, while in the first electronic excited state the total spin could be 0 (singlet S_1) or 1 with the multiplicity 3 (triplet T_1). Because of the Pauli exclusion principle the energy of the T_1 state is usually less as the energy of the S_1 state (Figure 2-16). The transition from the singlet state S_1 to the triplet state T_1 by intersystem crossing is spin forbidden, equally the transition from the triplet state T_1 into the ground state S_0. Therefore, optical transitions are possible only within the singlet systems. The absorption factor for the transition $S_0 \rightarrow S_1$ is large and the fluorescence period for the reverse process $S_1 \rightarrow S_0$ is very short and lies in the nanosecond range. If a molecule is located in the triplet state, the transition to the ground state, also called the phosphorescence, is normally not allowed. The lifetime of this state is essential longer (in the millisecond range).

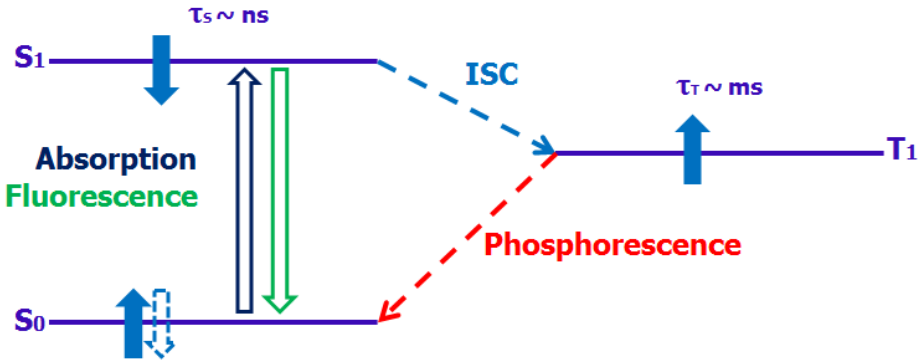

Figure 2-16 Energy level scheme for singlet and triplet states in an organic molecule with the respective optical transitions. The scheme contains absorption (blue), fluorescence (green) and phosphorescence (red) energy levels.

Generally, organic semiconductors are low-molecular weight organic materials and polymers with a conjugated π-electron system. This exists if in one hydrocarbon element between the C atoms a double or triple bond occurs. Organic semiconductor materials differ from inorganic materials in optical, charge carrier transport, electronic, chemical and structural properties.

The fundamental difference between inorganic and organic semiconductor materials is the bonding. In organic semiconductors, the bonding is van der Waals, which is considerably weaker as compared to the covalent bonding prevailing in inorganic semiconductors. As a consequence, organic semiconductors differ from inorganic in optical properties and charge carrier transport. In comparison to inorganic semiconductor materials, organic semiconductors

have two important characteristics. One of the differences is the existence of the spin states (singlet and triplet) and another one is that optical excitations are localized on one molecule. As a result they have a considerable binding energy. Band transport will be observed in molecular solids at low temperatures. Because the bandwidth is small, the mobility values are in the range 1 to 10 $cm^2/V{\cdot}s$. For amorphous organic solids hopping transport prevails, which leads to even smaller mobility values of 10^{-3} $cm^2/V{\cdot}s$.

2.12 Transistor devices based on organic semiconductor materials

The use of organic semiconductors for sensors fabrication is a very interesting option because of the potential for much cheaper processing as printed electronic devices. They showed excellent performance in different electronic devices, including organic light-emitting diodes (OLEDs), organic solar cells, and organic thin-film transistors (OTFTs) (Lin and Yan, 2012). OTFTs can be divided into two types of transistors: organic field-effect transistors (OFET) and organic electrochemical transistors (OECT).

2.12.1 Organic field-effect transistor devices

An organic field-effect transistor (OFET) device is composed of source, drain and gate electrodes, a gate dielectric and an organic semiconductor. This is very similar to the previously discussed MOSFET. By application of the drain-source voltage V_{DS} the channel current I_{DS} of an OFET device flows through the organic semiconductor due to the charge carrier transport. The channel current I_{DS} of an OFET can be modulated by the gate voltage due to the field-effect doping and is given by (Lin and Yan, 2012):

$$I_{DS} = \mu \frac{W}{L} C_i (V_{GS} - V_{Th}) V_{Ds} \qquad \text{when } V_{DS} \ll V_{GS} - V_{Th} \qquad (2.50)$$

and

$$I_{DS} = \mu \frac{W}{2L} C_i (V_{GS} - V_{Th})^2 \qquad \text{when } V_{DS} > V_{GS} - V_{Th} \qquad (2.51)$$

where μ is the carrier mobility, W the width and L the length of the channel, C_i the capacitance of the gate insulator, V_{GS} the gate-source voltage, and V_{Th} the threshold voltage, which is related to the dopping level of the channel. The threshold voltage is changed due to doping effect of the analytes. The carrier mobilityof the OFET can be changed due to the diffusion of analyte through the semiconductor grain boundaries (Lin and Yan, 2012) (Roberts et al., 2008).

2.12.2 Organic electrochemical transistor devices

An organic electrochemical transistor (OECT) device is composed of source and drain electrodes, which are connected via an organic polymer. The third electrode, the gate, is in contact with the organic polymer by an electrolyte (Kergoat et al., 2012). OECT devices operate at low voltages (below 1 V). The channel current I_{DS} of an OECT device can be modulated by the gate voltage due to the electrochemical doping and de-doping of the organic polymer by the electrolyte (Lin and Yan, 2012). The channel current I_{DS} is given by:

$$I_{DS} = \frac{q\mu p_0 tW}{LV_p}\left(V_p - V_g^{eff} + \frac{V_{DS}}{2}\right)V_{DS} \qquad \text{when } |V_{DS}| \ll |V_p - V_g^{eff}| \qquad (2.52)$$

where q is the electronic charge, μ the hole mobility, p_0 the initial hole density in the organic semiconductor when gate voltage is zero, W the width and L the length of the channel, t the thickness of the active layer, V_p the pinch-off voltage, which is given by:

$$V_p = \frac{qp_0 t}{C_i} \qquad (2.53)$$

where C_i is the effective gate capacitance of the transistor.

The effective voltage V_g^{eff} in equation (2.52) is given by:

$$V_g^{eff} = V_G + V_{offset} \qquad (2.54)$$

where V_{offset} is the offset voltage related to potential drop at the gate/electrolyte interface and the electrolyte/channel interface.

2.13 PEDOT:PSS

Poly(3,4-ethylenedioxythiophene) poly(styrenesulfonate) (PEDOT:PSS) is the mostly used organic polymer for biological and chemical sensing applications (Kergoat et al., 2012). PEDOT:PSS is composed of two components: polystyrene sulfonate, which carries a negative charge, and poly(3,4-ethylenedioxythiophene), which is based on polythiophene and carries a positive charges (Figure 2-17).

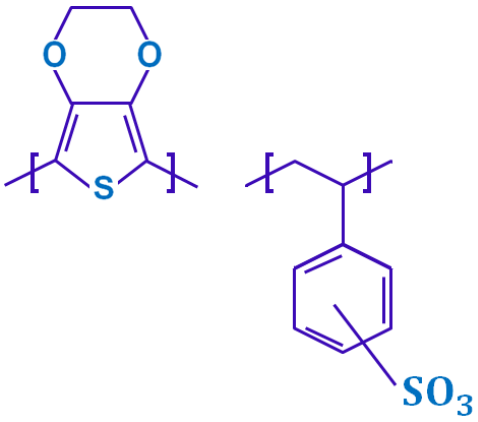

Figure 2-17 The schemical structure of PEDOT:PSS.

2.13.1 The operation principle of the PEDOT:PSS based transistors

PEDOT:PSS is able to conduct both electrons and ions (Basiric, 2012). When the PEDOT:PSS film is in contact with an electrolyte, the ions (predominantly cations) from this electrolyte enter the PEDOT:PSS film and the conduction of the material increases.

By application of a small positive gate voltage, cations from the electrolyte enter the PEDOT:PSS film and reduce the PEDOT component to its neutral state (equation (2.55), direction from left to right). This results in the electrochemical de-doping of the PEDOT:PSS film, thus in the decrease of the channel current. In this thesis, an electronic circuit in conjunction with an ionic circuit was used to describe the device behavior. The density and mobility of the holes have an influence on the electronic transport. The ions in the electrolyte determine the ionic transport.

The reduction of the highly conducting form of $PEDOT^+$ to the less conducting form of $PEDOT^0$ is reversible and given by (Nikolou and Malliaras, 2008):

$$PEDOT^+ : PPS^- + M^+ + e^- \leftrightarrow PEDOT^0 + M^+ : PSS^- \quad (2.55)$$

where M^+ is a cation in the electrolyte and e^- is an electron (Nikolou and Malliaras, 2008). The reduction of the PEDOT:PSS film is operated by the migration of cations into the channel. When a small positive gate voltage will be removed, the cations diffuse back into the electrolyte (equation (2.55), direction from right to left).

2.13.2 Conductivity of PEDOT:PSS

PEDOT:PSS is a water-soluble, conductive polymer. Therefore its usage for ISFET applications is delicate. Some studies showed that treatment of a PEDOT:PSS film with organic solvents, such as ethylene glycol (Ouyang et al., 2004) (Basiricò et al., 2012) (Basiric, 2012) or glycerol (Tsukada et al., 2012), leads to its insolubility in water. (Ouyang et al., 2004) explained the solubiliy change of the PEDOT:PSS film after treatment with ethylene glycol (EG) by an increase of the interchain interaction. By means of Raman spectroscopy it was shown that a change of the PEDOT chains from the coil to linear structure occurs. Figure 2-18 shows the changes of the structure of the PEDOT chains from a benzoid to a quinoid structure, where the benzoid structure is favorable for a coil conformation and the quinoid structure is favorable for a linear structure, respectively.

The benzoid structure is favored for a coil conformation of the PEDOT chain, while the quinoid structure is favored for a linear or expanded-coil conformation. Since the interaction forces among the PEDOT chains in the linear structure are stronger than those in the coil structure, such transformation leads to an increase of the interchain interaction, resulting in both conductivity enhancement and insolubility of PEDOT:PSS film coated with EG.

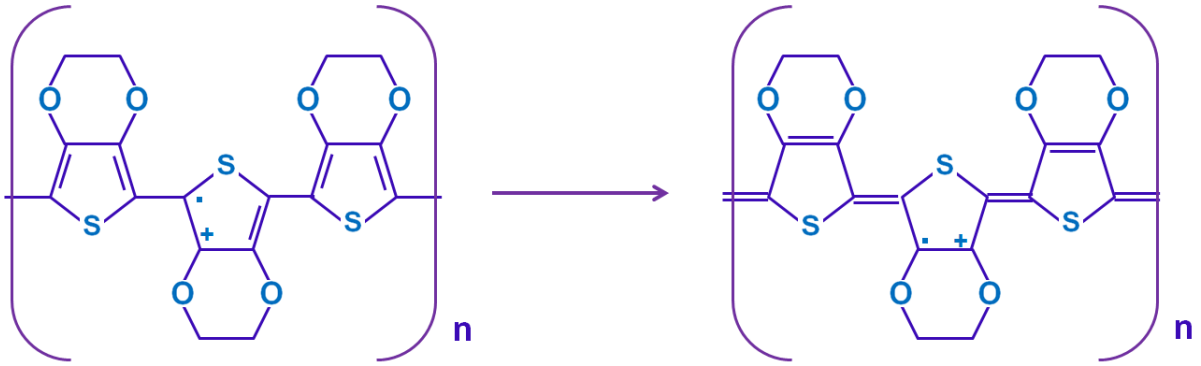

Figure 2-18 Scheme of transformation of the PEDOT chain from the benzoid to the quinoid structure. The ‘dot’ and ‘plus’ represents the unpaired electron and positive charge on the PEDOT chain, respectively.

(Yamashita et al., 2011) explained the influence of the organic solvent (ethylene glycol) on the carrier density and mobility in the PEDOT:PSS film through the combination of terahertz time-domain spectroscopy and the broadband reflectance spectroscopy.

Chapter 3

3 Materials and methods

In this chapter, the silicon-based as well as the organic field-effect transistor devices, the measurement setups for recording of the transfer functions (impedance spectra) of the individual cells adhered on top of the FET devices, the chip encapsulation and the chip cleaning protocols, as well as the cell types used in this work will be introduced.

3.1 Design of the silicon-based field-effect transistor devices

In this section, two generations of silicon-based p-channel open-gate field-effect transistor devices used to study the single cell-substrate adhesion will be presented. During the period of implementation of this thesis a new generation of the FET devices was designed and fabricated in due consideration of the results, which were obtained from the simulations performed for optimization of the device performance. These simulations will be presented in chapter 4 (section 4.4). For optimized device performance the ratio of gate width to gate length was increased, the thickness of the gate silicon dioxide was downscaled, as well as the thickness of the silicon oxide passivation layer on the contact lines was decreased. This enabled an almost flat surface of the FET devices for single cell adhesion experiments and for single cell migra-

tion studies. The topography of the gate areas in both FET designs will be compared by atomic force microscopy measurements (Dimension 3100, Digital Instruments Veeco Metrology, Santa Barbara, USA) and scanning electron microscopy measurements (Carl Zeiss AG, Supra 40, Germany). The measurements were carried out in tapping mode with a scanned area of about 50×50 µm^2. The detailed fabrication process of these devices can be found in the appendix.

3.1.1 Previous generation of the FET devices

The previous generation of the FET devices was fabricated at the Max-Planck Institute for Polymer Research Mainz, Germany in an earlier project. The FETs were arranged in a 4×4 array with a distance of 200 µm between individual transistors (pitch) in the center of a 5×5 µm^2 silicon chip. The gate dimensions were 5 µm in length, 16 µm in width, and the thickness of the gate silicon dioxide was 8 nm (Krause, 2000). In Figure 3-1 the colored scanning electron microscope (SEM) image of a single gate structure of this chip design is presented.

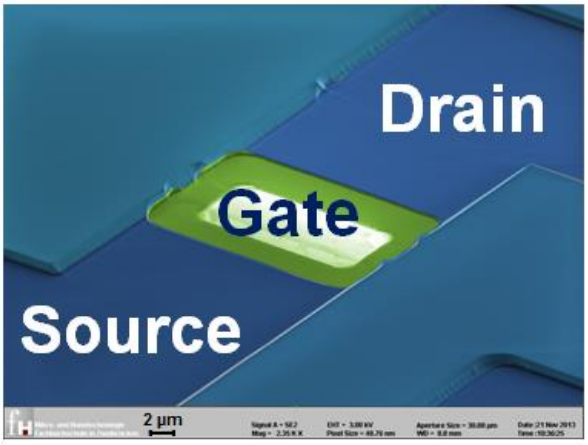

Figure 3-1 Colored scanning electron microscope image of a single gate structure of the previous chip design. The gate dimension of this layout is 5×16 µm^2.

In Figure 3-2 the atomic force microscopy (AFM) image of the gate structure of the previous FET device and the line scans along (blue line) and across (green line) the gate structure are shown. The line scan along the gate structure gives the information about the edge heights

between the field oxide layer (pale blue area on Figure 3-1), the ONO (silicon oxide layer - silicon nitride layer - silicon oxide layer) passivation layer (the green area on Figure 3-1 is the opening of this ONO stack) and the gate oxide layer (pale green area on Figure 3-1). Thus, the thickness of the field oxide layer amounts to 1.3 µm and the thickness of the passivation layer 290 nm in the measurement. This step height is a combination of the remaining field oxide layer and the deposited nitride and oxide layers. Details can be found elsewhere (Krause, 2000). The line scan across the gate structure gives the information about the edge heights between the conducting lines for source and drain (dark blue area on Figure 3-1), the ONO-stack passivation layer (green area on Figure 3-1) and the gate oxide layer (pale green area on Figure 3-1). Thus, the height of the conducting lines for source and drain amounts to 480 nm. The values achieved by these AFM measurements correspond the proposed values for fabrication process (appendix). This results in a quite large topography on the chip surface. Therefore, cells preferentially adhered to edges and grooves of this chip design (Figure 4-36a).

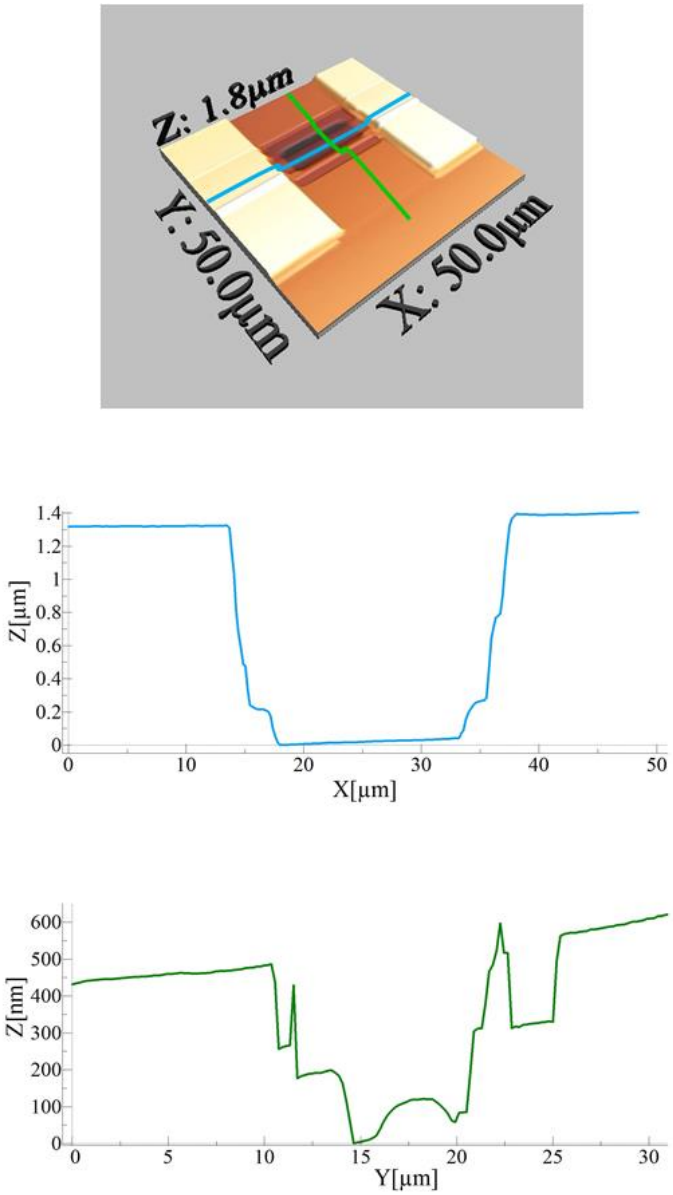

Figure 3-2 Atomic force microscopy image of the gate area of the previous FET design. The scanning area was about 50×50 µm^2. The thickness of the field oxide layer amounts to 1.3 µm and the thickness of the passivation layer 290 nm (the values were achieved from the scan along the gate structure (blue line)). The height of the conducting lines for source and drain amounts to 480 nm (the value was achieved from the scan across the gate structure (green line)).

3.1.2 New generation of the FET devices

The new generation of the FET devices was fabricated at the University of Applied Sciences Kaiserslautern in Zweibrücken, Germany during the time of this thesis. The FETs were arranged in a 4×4 array with a distance of 200 µm between individual transistors (pitch) in the center of a 7×7 μm^2 chip. The gate dimensions were 5 µm in length, 25 µm in width, and the thickness of the gate silicon oxide was reduced to 6 nm. In Figure 3-3 the colored SEM image of a single gate structure of the new chip design is shown.

Figure 3-3 Colored scanning electron microscope image of a single gate structure of the new chip design. The gate dimension is 5×25 μm^2.

Also, for the new FET device design AFM measurements were performed (Figure 3-4). The line scan along the gate structure gives the information about the passivation layer (pale blue area on Figure 3-3) and the gate oxide layer (green area on Figure 3-3). Thus, the thickness of the passivation layer amounts to 220 nm. The line scan across the gate structure gives the information about the edge heights between the conducting lines for source and drain (dark blue area on Figure 3-3) and the gate oxide layer (green area on Figure 3-3). Thus, the height of the conducting lines for source and drain amounts to about 200 nm as well. The values achieved by AFM measurement correspond the proposed values for the fabrication process (appendix). As it can be seen, a much flatter chip surface for the new FET devices was achieved in this process. Therefore, cells adhered uniformly on the whole surface of these devices (Figure 4-36b).

For cell–substrate adhesion and migration experiments, the surface topography is very important because it has an influence on the general cell morphology and thus the seal resistance R_{seal}. The flatter the transistor surface the stronger is the electronic coupling strength as well (Voelker and Fromherz, 2006).

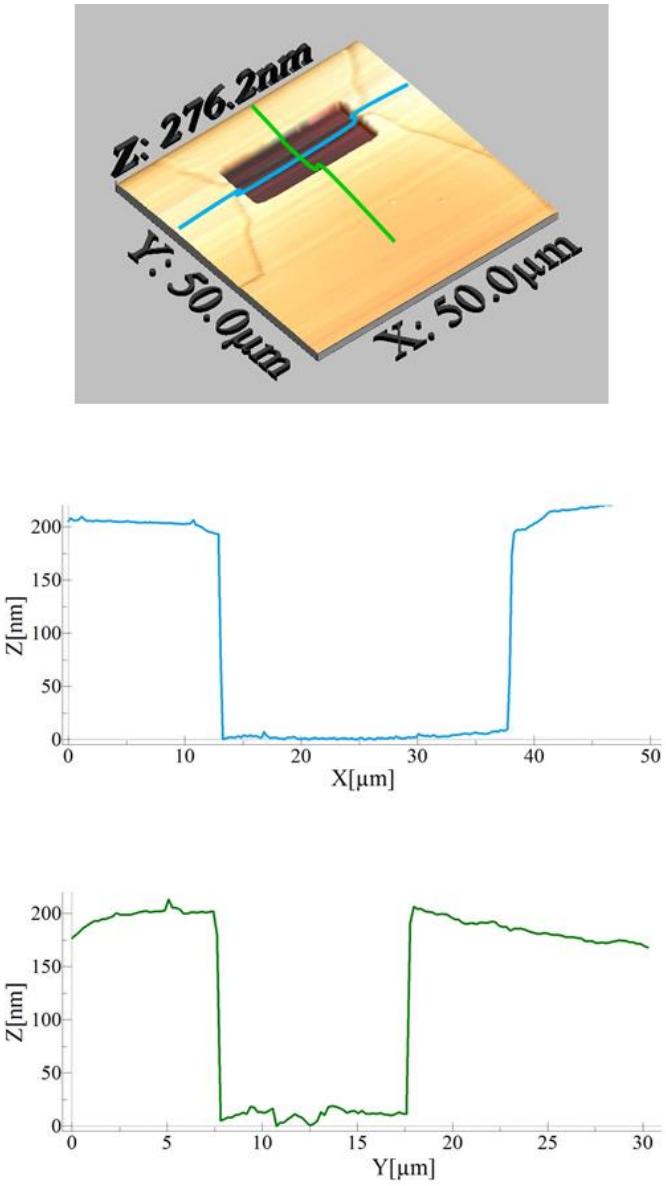

Figure 3-4 Atomic force microscopy image of the gate area of the new FET design. A scanning area is about 50×50 µm^2. The thickness of the passivation layer is 220 nm (the value was achieved from the scan along the gate structure (blue line)), the height of the conducting lines for source and drain about 200 nm (the value was achieved from the scan across the gate structure (green line)).

3.2 Design of the organic electrochemical transistor devices

The organic electrochemical transistor (OECT) devices were fabricated at the University of Applied Sciences Kaiserslautern in Zweibrücken, Germany.

Due to the fact that the carrier mobility and respective the conductivity (equation (2.15)) of the organic semiconductor materials is essentially smaller than the carrier mobility of inorganic semiconductor materials (for comparison μ_{Si} = 450 $cm^2/V \cdot s$ and $\mu_{PEDOT:PSS}$ = 0.15 $cm^2/V \cdot s$ and after treatment with ethylene glycol (EG) $\mu_{PEDOT:PSS}$ = 3.6 $cm^2/V \cdot s$ (Yamashita et al., 2011)), the drain and source electrodes were designed in form of interdigitated electrodes (IDEs) in order to increase the transconductance and respectively to improve the bandwidth of the devices.

The interdigitated sensor structure is explained in Figure 3-5 by taking the example of a multi-finger design (two interdigitated electrodes on each side). The distance between the drain and source electrodes was denoted as gap, the width on which the drain and source electrodes are opposing each other is denoted as W (the finger width) and the width of the interdigitated electrode is denoted as L (the finger length). For such multi-finger design, the finger width W is the sum about each individual channel.

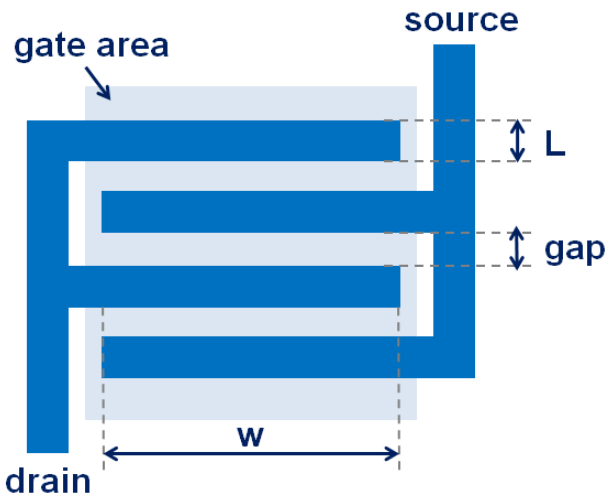

Figure 3-5 The interdigitated sensor structure of two interdigitated source and drain electrodes with defining channel length L and width W dimensions.

The interdigitated sensor structures were arranged in a 4×4 array with a distance of 500 µm between individual IDEs (pitch) in the center of a 7×7 µm^2 glass chip. Different designs of the IDEs (single- and multi-finger designs) were used to find out the optimal structure for cell adhesion measurements. In Figure 3-6 the layout of the OECT devices with the finger length of 5 µm, the gap of 6 µm, different number of IDEs, and different gate areas are presented.

3.3 New design of the organic electrochemical transistor devices

In due consideration of the results obtained from the performed measurements of the cell adhesion on the fabricated OECT devices (chapter 5, section 5.4), the new generation of the OECT devices was designed during the time of this thesis.

Compared to the FET devices based on silicon, the OECT devices have a small cutoff frequency (chapter 5, section 5.3 and section 5.4). For the FET devices based on silicon, in order to increase the cutoff frequency the channel length should be scaled-down:

$$f_{cutoff} = \frac{\mu_n(V_{GS}-V_{Th})}{2\pi L^2} \quad (3.1)$$

A smaller channel length L will improve the performance of the transistor by increasing the transconductance (L^{-1}) and the cutoff frequency (L^{-2}). For the OECT devices this will be determined.

In the new design, the interdigitated sensor structures were arranged in a 8×8 array and in a 2×16 array (for monitoring of the cell migration) with a distance of 200 µm between individual IDEs (pitch) in the center of a 7×7 µm^2 glass chip. Moreover, the gate area was decreased to the size of an individual cell, the number of IDEs was increased whereas the finger length was downscaled. In Figure 3-7 the layout of the new generation of the OECT devices with the finger length similar the gap of 0.3 µm and the gate area of 50×50 µm^2 and 30×30 µm^2 are presented.

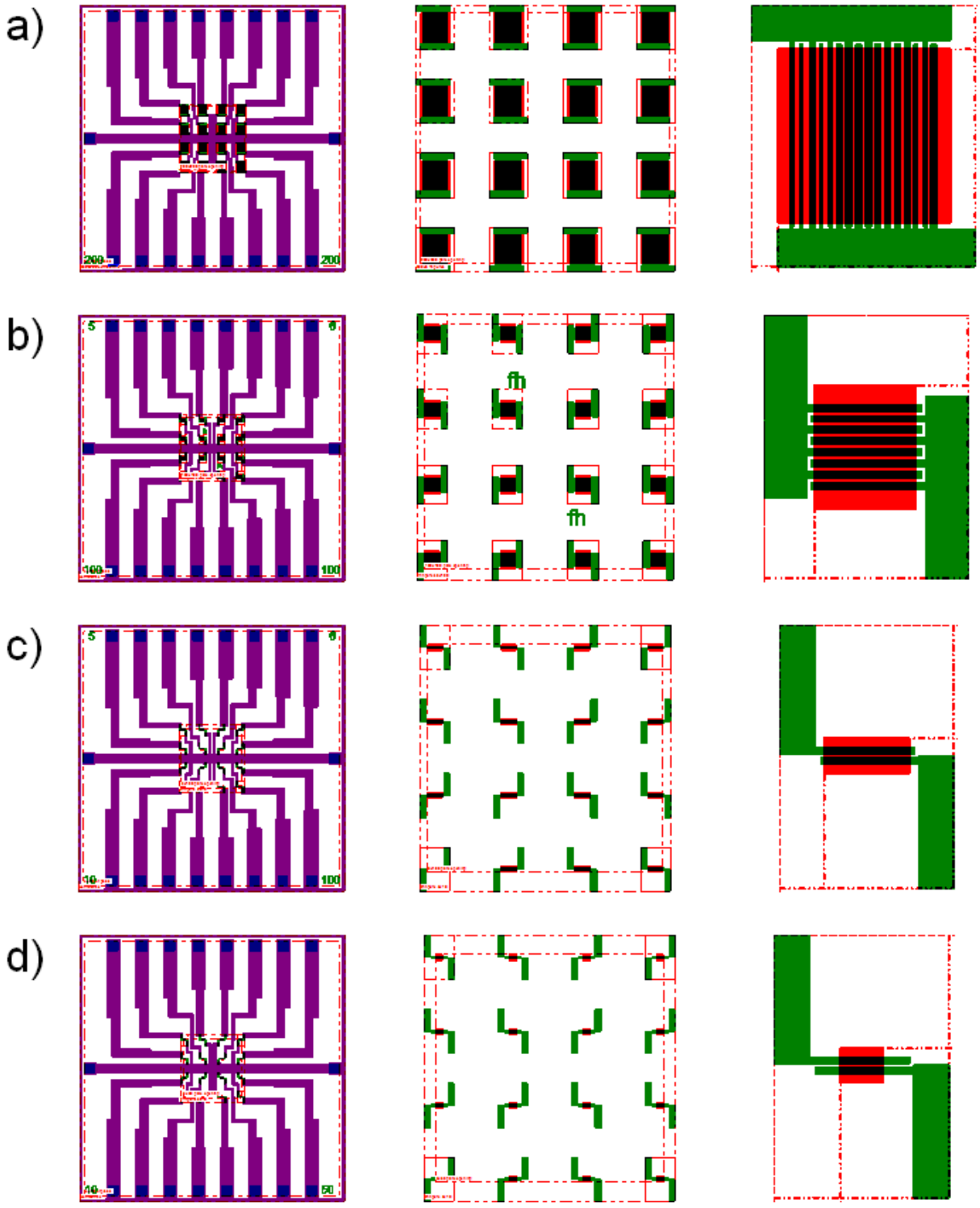

Figure 3-6 Layout of the 16 channel organic electrochemical transistor (OECT) arrays. a) 8 interdigitated source and drain electrodes with the gate area (red area) of 200×200 μm^2 b) 4 interdigitated source and drain electrodes with the gate area of 100×100 μm^2 c) single interdigitated source and drain electrode with the gate area of 100×10 μm^2 d) single interdigitated source and drain electrode with the gate area of 50×50 μm^2.

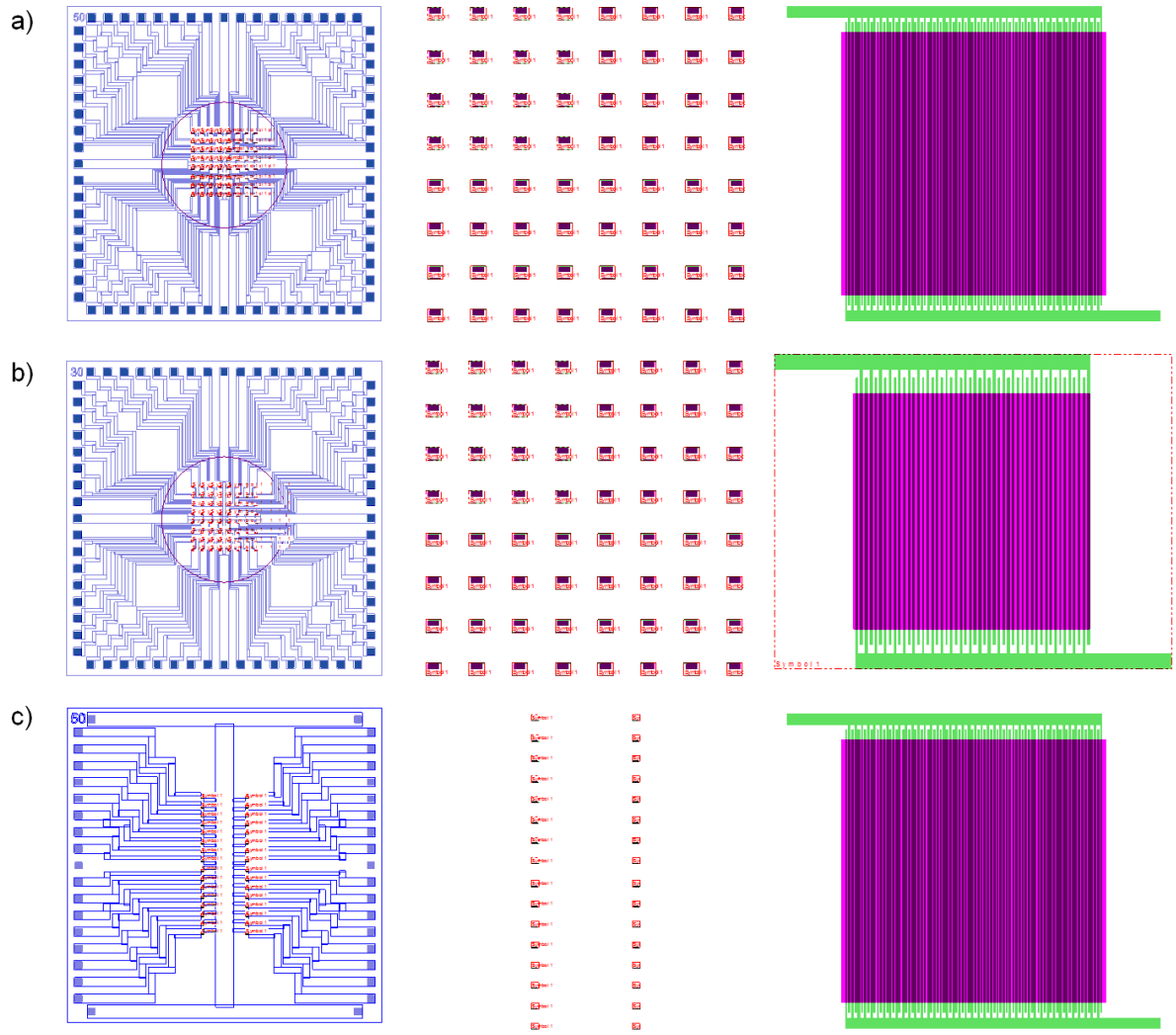

Figure 3-7 a) Layout of the 64 channels organic electrochemical transistor (OECT) array with 40 interdigitated source and drain electrodes and the gate area of 50×50 μm^2 b) Layout of the 64 channel organic electrochemical transistor (OECT) array with 25 interdigitated source and drain electrodes and the gate area of 30×30 μm^2 c) Layout of the 32 channel organic electrochemical transistor (OECT) array with 40 interdigitated source and drain electrodes and the gate area of 50×50 μm^2.

3.4 Fabrication process of the OECT devices

The OECT devices were fabricated on glass substrates at the University of Applied Sciences Kaiserslautern in Zweibrücken, Germany, during this thesis. Poly(3,4-ethylenedioxythiophene) doped with poly(styrene sulfonate) (PEDOT:PSS) was used as an active layer.

Figure 3-8 shows a schematic cross-section of the fabricated OECT devices.

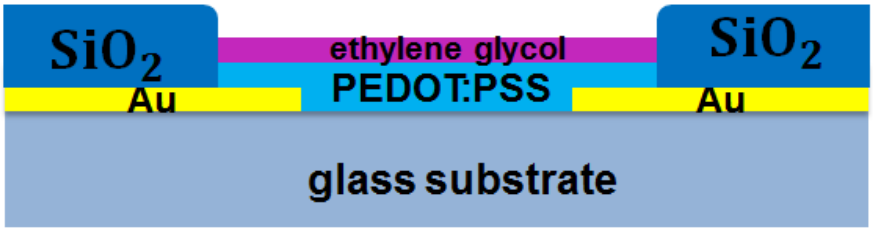

Figure 3-8 Schematic view of the cross-section of the fabricated OECT devices.

First, a 4×4 array of gold interdigitated source and drain electrodes were patterned onto the glass substrates by a lift-off process. After passivation of the gold contact lines by plasma-enhanced chemical vapor deposition (PECVD) (600 nm of silicon dioxide), the interdigitated electrode areas were opened and used as the electric contact to the polymer layer. The PEDOT:PSS solution (Orgacon IJ-1005, Sigma Aldrich, Germany) was inkjet-printed on top of the interdigitated electrodes by a material printer Fujifilm Dimatix Material Printer 2800 (DMP-2800) using a DMC-16610 cartridge (Figure 3-9). Before printing the PEDOT:PSS solution was filtered with a 0.45 µm syringe filter in order to avoid eventual blockage of the cartridge nozzles. Two subsequent layers of PEDOT:PSS (the thickness of one layer was about 60 nm) with a drop spacing of 20 µm were inkjet-printed. After printing, devices were subsequently annealed in vacuum environment at 120° C for four hours. A thin layer of ethylene glycol (Sigma Aldrich, Germany) was then spin coated on top of the PEDOT:PSS film and subsequently annealed at 120° C for 14 hours as well.

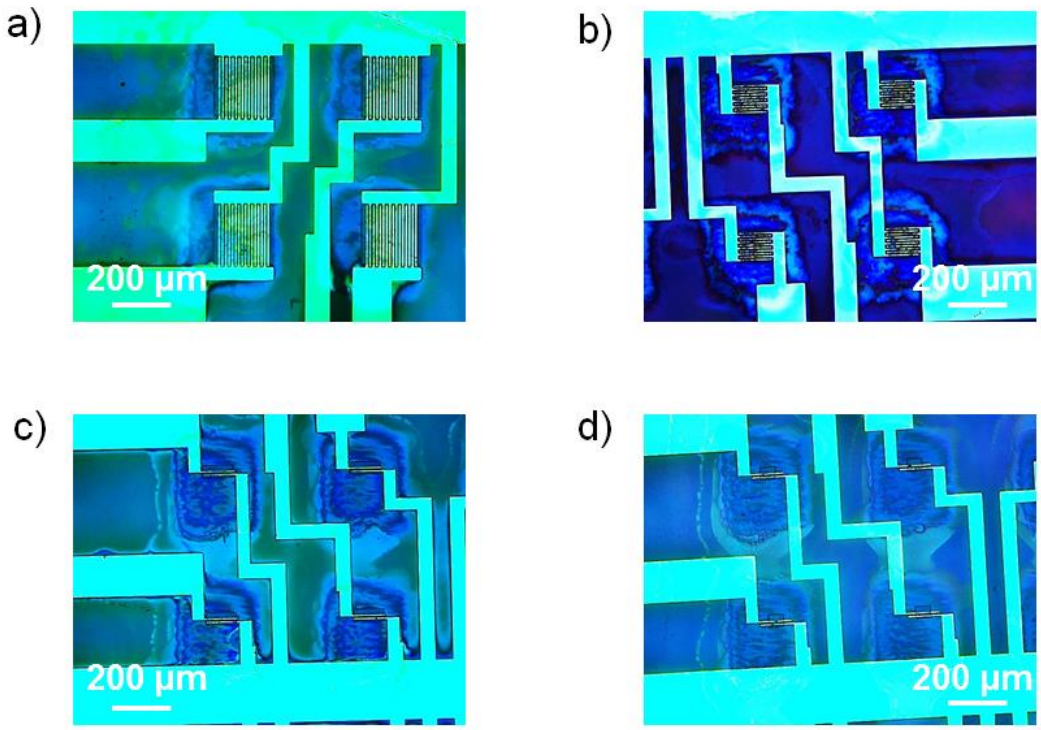

Figure 3-9 Microscopic image of the printed PEDOT:PSS solution on top of the interdigitated electrodes (IDEs) a) 8 IDEs, gate area of 200×200 µm^2 b) 4 IDEs, gate area of 100×100 µm^2 c) 1 IDE, gate area of 100×10 µm^2 d) 1 IDE, gate area of 50×50 µm^2.

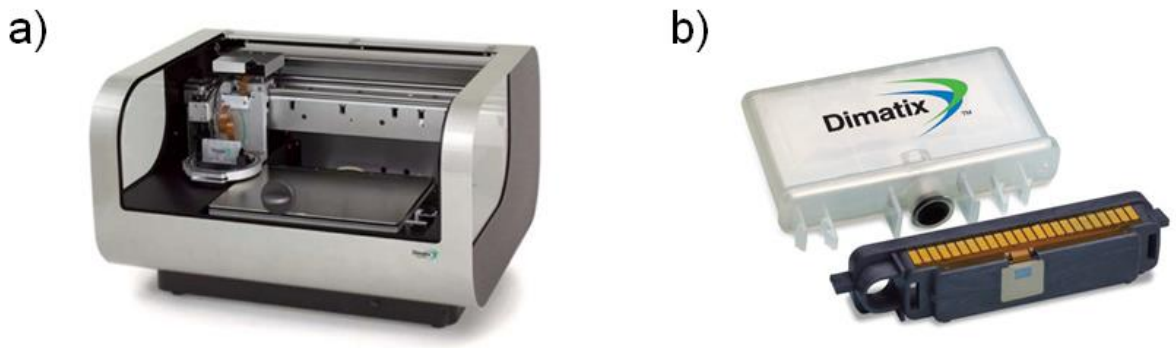

Figure 3-10 a) Picture of the Dimatix Materials Printer 2800 (DMP-2800) was adapted from ("FUJIFILM Dimatix Materials Printer DMP-2800 Series User Manual," 2010) b) Picture of the cartridge (DMC-16610), which consists of a plastic bag acting as ink reservoir and the printhead, was adapted from ("FUJIFILM Dimatix Materials Printer DMP-2800 Series User Manual," 2010).

3.4.1 Dimatix Materials Printer

The inkjet printer (Dimatix Materials Printer 2800 (DMP-2800), FUJIFILM, USA) used for the fabrication of OECT devices is shown in Figure 3-10a. The system is controlled by an application software and allows the deposition of fluidic materials on substrates, utilizing a piezo inkjet cartridge. The cartridge consists of a plastic bag which acts as ink reservoir and a printhead, where 16 nozzles linearly spaced at 254 microns with typical drop sizes of 1 and 10 picoliters (Figure 3-10b).

The printer can create and define patterns over an area of about 200×300 mm^2 and handle substrates up to 25 mm thick with an adjustable height. The DMP-2800 offers a variety of patterns using a pattern editor program. Additionally, a waveform editor and a drop-watch camera system allows manipulation of the electronic pulses to the piezo jetting device for optimization of the drop characteristics as it is ejected from the nozzle ("FUJIFILM Dimatix Materials Printer DMP-2800 Series User Manual," 2010). It was therefore ideally suited for fabrication of the PEDOT:PSS OECT devices in a swift and easy manner.

Monitoring and adjusting the ink jets was possible by using the Drop Watcher Camera System. This system allowed viewing of the jetting if the jets have single, spherical drop, their direction was perpendicular to the nozzle plate and parallel to each another.

The Fluidical Camera is a tool consisting of a camera, mounted on the print carriage able to frame all parts of the substrate. For OECT fabrication the camera was used to align a pattern on a substrate and after printing to check the print quality.

3.5 Encapsulation of the FET devices

All devices were encapsulated for cell culture as previously described by (Offenhäusser et al., 1997) (Ingebrandt et al., 2003). First, the FET devices were cleaned in an ultrasonic bath by three steps (twice in acetone and then in isopropyl, 5 min in each case). Then, the chips were glued with two components of epoxy glue (EPO-TEC 377 1LB Kit, Epoxy Technology Inc., USA) to 68-pin LCC (Leaded Chip Carrier) carriers (Global chip Materials, LLC, USA).

Next, the contacts from chip to carrier were done by wirebonding with aluminium wire (Al/Si 1%, 25 µm in diameter) using the wedge-wedge wire bonding machine (West Bond Inc., USA). Afterwards, the glass rings were glued onto the carriers and the funnels (2.8 mm in diameter) onto the chips. Hence, the area for cell culture experiments was provided. The funnels were made by mould technique using two components of the adhesive (SYLGARD 184, Dow Corning, Germany). The free volume between glass ring and funnel was filled with isolating polydimethylsiloxan (PDMS) glue (SYLGARD 184, Dow Corning, Germany) to prevent shortcuts between bondwires and electrolyte bath. The complete encapsulated FET chip is shown in Figure 3-11b.

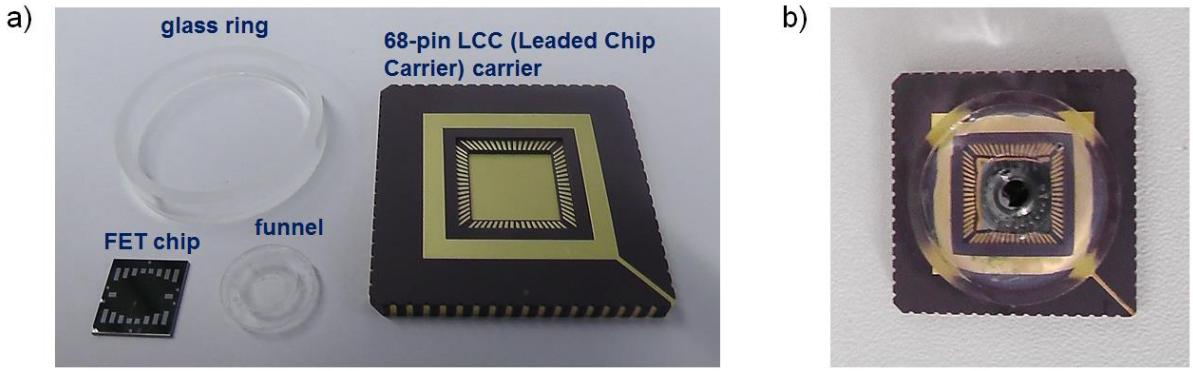

Figure 3-11 a) Parts for encapsulation: 68-pin LCC carrier, FET chip, glass ring and the funnel. b) The complete encapsulated FET chip.

3.6 Reference electrode

A self-made silver/silver chloride (Ag/AgCl) wire was used as a reference electrode in this thesis.

The Ag/AgCl electrode was produced by means of electrolysis. The purpose of the chlorination is to reduce the characteristic impedance of the electrode to a minimum. In the Ag/AgCl electrode occur only minimal resistance or voltage efficient changes (Ziersch, 1999).

A reference electrode should ideally maintain a constant potential in a solution preferably independent of external influences over the longest period. This ensures that all the observed potential changes occur at the working electrode due to electrochemical processes (Wiest,

2008). The stability of the reference electrode is very important for all electrochemical measurements. A high stability of electrode reference potentials can be achieved using a redox system with constant concentrations of the participants of the redox reaction (Santoro et al., 2012). The salt concentration in an extracellular solution is maintained roughly at a constant value. Therefore, the silver chloride electrode exhibits a stable potential for electrical cell measurements.

3.7 Measurement setups

In this section, two measurement setups, namely the transistor transfer function (TTF) amplifier system and the within the scope of this work newly developed amplifier system with a fast lock-in amplifier (HF2LI, Zürich Instruments, Switzerland) (Figure 3-12) are described. The main goal of the development of the new amplifier system was the achievement of the higher bandwidth.

The transfer functions (impedance spectra) measured with the TTF amplifier system show only the real part of the transfer function:

$$H(jw)\cos\big(\varphi(w)\big) \tag{3.2}$$

The transfer functions (impedance spectra) measured with the lock-in amplifier system are represented as bode plots with frequency-dependent amplitude |H(jw)| and phase $e^{j\varphi(w)}$ components.

The HF2LI gives the transfer function of a device in the form of a Bode plot. The measured spectrum is saved in cartesian components ("HF2 User Manual," 2014). By data evaluation the cartesian components (x and y) will be converted to the polar components (r and φ) by:

$$\mathrm{r} = \sqrt{\mathrm{x}^2 + \mathrm{y}^2} \tag{3.3}$$

$$\varphi = \arctan\left(\frac{\mathrm{y}}{\mathrm{x}}\right) \tag{3.4}$$

where r is the amplitude of the transfer function and φ the phase of the transfer function.

Figure 3-12 Lock-in amplifier HF2LI. The image is accepted from ("HF2 User Manual," 2014)

3.7.1 Transistor transfer function amplifier system

The transistor transfer function (TTF) amplifier system was already described in previous works (Ingebrandt et al., 2005) (Ingebrandt et al., 2007) (Schäfer et al., 2009). This portable, 16-channel amplifier system, which can be operated in potentiometric and impedimetric mode, was used to characterize the FET devices, to measure the frequency-dependent transistor transfer functions and to record the time-dependent data by selection of only one fixed frequency.

Potentiometric readout

A 16-channel amplifier system is composed of a preamplifier, a main amplifier and a microprocessor. The schematic view of the amplifier circuit for potentiometric readout is shown in Figure 3-13 (Han, 2006).

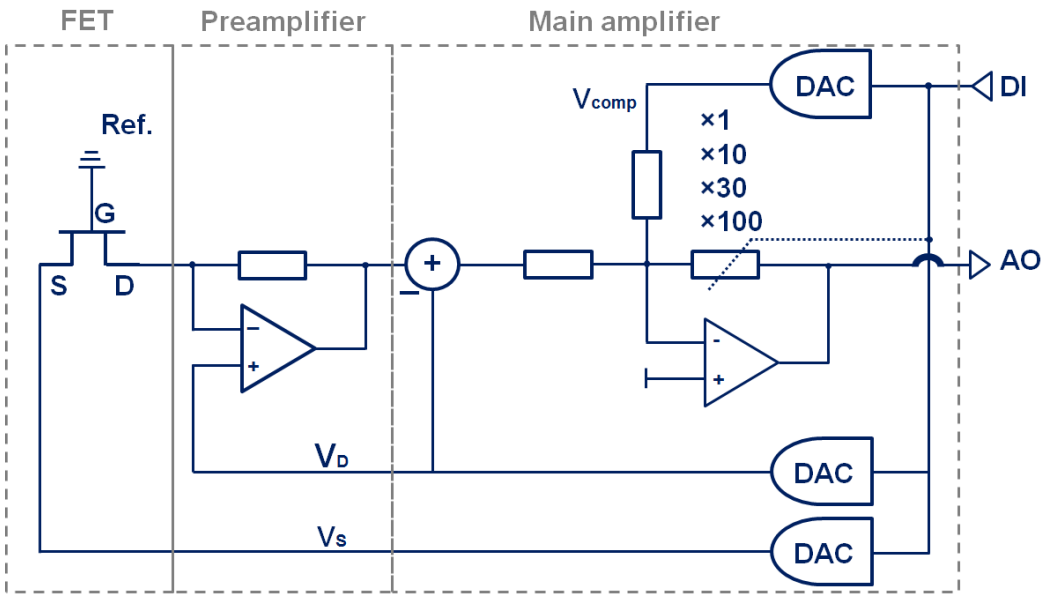

Figure 3-13 The schematic view of the amplifier circuit for potentiometric readout. In the schematic view, digital to analog convertes (DAC) are providing the source voltage V_S, the drain voltage V_D and the compensation voltage V_{comp}.

By a first stage in the preamplifier, changes in the drain-source current ΔI_{DS} will be converted into voltages:

$$\Delta V_{out} = -R_{feedback}\Delta I_{DS} \tag{3.5}$$

By a second stage in the main amplifier, the signals will be amplified by selecting ×1, ×10, ×30 or ×100 amplification factor, respectively. At the beginning of the time-dependent potentiometric readout, the constant drain-source current of the 16 transistors will be compensated by applying individual compensation voltage V_{comp} for each channel, separately (Ingebrandt et al., 2007).

Impedimetric readout

The schematic view of the amplifier circuit for impedimetric readout is shown in Figure 3-14. The system is based on a phase-selective amplifier system composed of a Direct Digital Synthesis (DDS) device and a multiplier followed by a low pass filter for all 16 channels in parallel (Han, 2006).

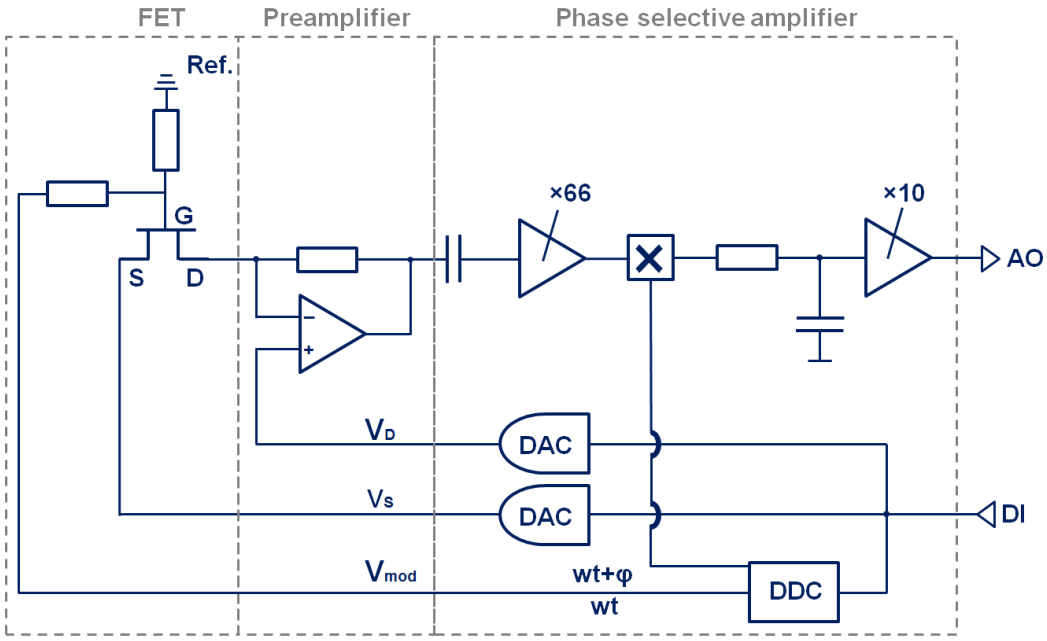

Figure 3-14 The schematic view of the amplifier circuit for impedimetric readout. The system is based on a phase-selective amplifier system composed of a Direct Digital Synthesis (DDS) device and a multiplier (box denoted with ×) followed by a low pass filter. The modulation voltage V_{mod} is provided by a direct digital synthesis (DDS) device to the reference electrode.

After setting of the transistors to a working point of maximum transconductance, the transfer functions were measured by applying a sinusoidal signal with 10 mV amplitude and varying frequency from 1 Hz to 1 MHz to the reference electrode. Test signals of exact amplitude, frequency and phase were provided by a DDC device. Frequency-selective amplification was confirmed via a frequency multiplier device, which was built-in into a capacitive de-coupled amplification cascade (Ingebrandt et al., 2007) (Schäfer et al., 2009).

The amplifier unit was operated by a microprocessor and the acquired data were transferred via an USB connection to the computer. All measurements were controlled by means of a read-out software implemented in Delphi 5.0 (Borland Software Corporation).

3.7.2 The new amplifier system with a fast lock-in amplifier

In the context of this work, a new amplifier system including a fast lock-in amplifier was developed. In Figure 3-15 a schematic diagram of this measurement setup is depicted.

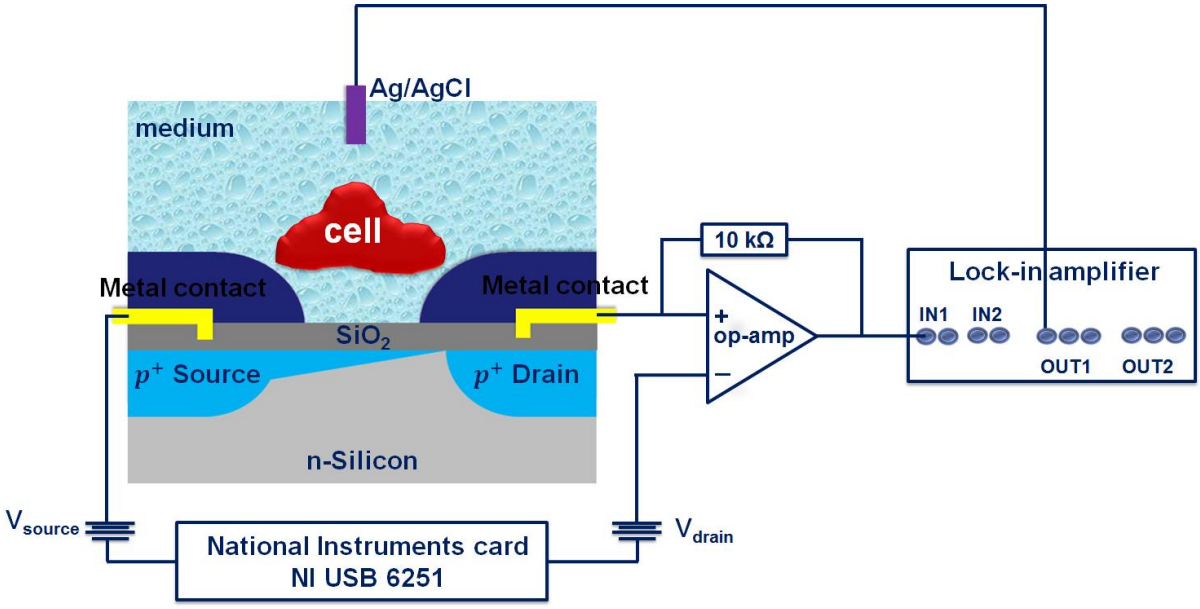

Figure 3-15 Schematic view of the measurement setup with a fast lock-in amplifier.

A preamplifier stage for the FETs, which uses a transimpedance amplifier (section 2.6), was connected to one of the two high-frequency input of a fast lock-in amplifier (HF2LI, Zürich Instruments, Switzerland). By using one of the analogue outputs, it was possible to apply a sinusoidal signal to the reference electrode, which was immersed into the electrolyte solution at a fixed position. The drain-source and gate-source voltages of the FET devices were controlled via the analogue outputs of a data acquisition card (USB 6251, National Instruments, Inc., Germany) using self-developed programs implemented in LabView. With these programs, it was possible to measure the output and transfer characteristics of the FET devices (Figure 3-16). From the available data, the transconductance was calculated in order to set the transistors to a working point with maximum transconductance. Transfer function measurements were done by applying a sinusoidal signal with 10 mV amplitude and varying frequency from 1 Hz to 50 MHz to the reference electrode. The transfer function of all 16 transistors on a chip needed to be measured consecutively with this setup.

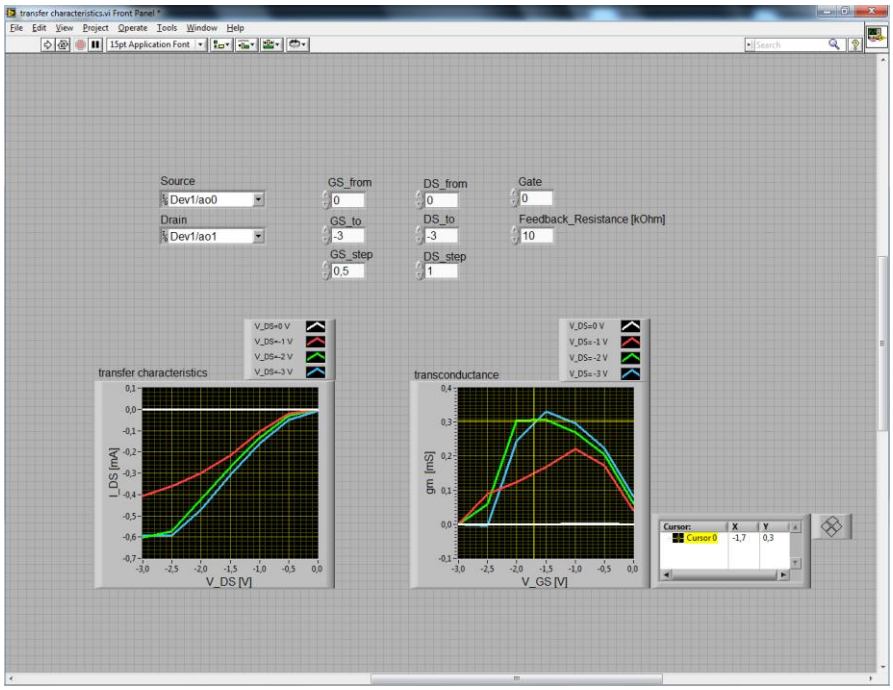

Figure 3-16 The self-developed program implemented in LabView for measuring of the transfer characteristics of the FET devices $I_{DS}(V_{DS})$ and setting of the transistors to a working point with maximum transconductance g_m.

With this new measurement setup, it was possible to characterize the FET devices, to measure the frequency-dependent transfer functions, and to record time-dependent data at multiple frequencies, simultaneously. In comparison to the TTF amplifier system, this new system had the following advantages: the bandwidth of the readout system was increased and the impedance spectra could be measured at higher frequencies (up to 50 MHz). In addition, time-dependent readout was achieved with the HF2LI system at several different frequencies, simultaneously. Since each analogue input of the HF2LI lock-in amplifier can record data at three different frequencies, the recording of the time-dependent data was possible at six different frequencies for one channel or at three different frequencies for two channels, respectively.

3.8 Transfer functions measured with two different measuring systems

The transfer functions (impedance spectra) recorded with one or the other measurement setup differ in a high-pass effect at low frequency and in the low-pass effect at high frequency. For the transfer functions measured with the TTF amplifier system, the low-pass effect is smoothed by internal switches in the formerly fabricated system, while for the transfer functions measured with the lock-in amplifier system developed in this thesis the high-frequency components were unfiltered.

In the following, the typical shapes of the transfer functions (impedance spectra) measured for cell-free as well as for cell-covered transistor gates of an FET device with two different measurement setups will be demonstrated. For this purpose, the H441 cells as well as the HEK 293 cells were cultured in low density on the FET devices. Before the impedance spectra were measured, the surface of the FET devices was controlled optically and the microscopic images of the cells cultured on the surface of the FET devices were taken in differential interference contrast mode (Axiotech Vario, Carl Zeiss AG, Germany) (Susloparova et al., 2013).

In Figure 3-17a the microscopic image of H441 cells cultured on an FET device is presented. For better viewing and distinguishing, only 4 from 16 transistor gates of an FET device are depicted. As it can be seen, some of the transistor gates are covered with cell (Figure 3-17a: chan2 and chan5), while others are cell-free (Figure 3-17a: chan1 and chan6). Firstly, the transfer functions were measured using the TTF amplifier system. Figure 3-17b shows the measured transfer functions of four transistor gates, which correlate to the transistor gates in Figure 3-17a (Susloparova et al., 2013).

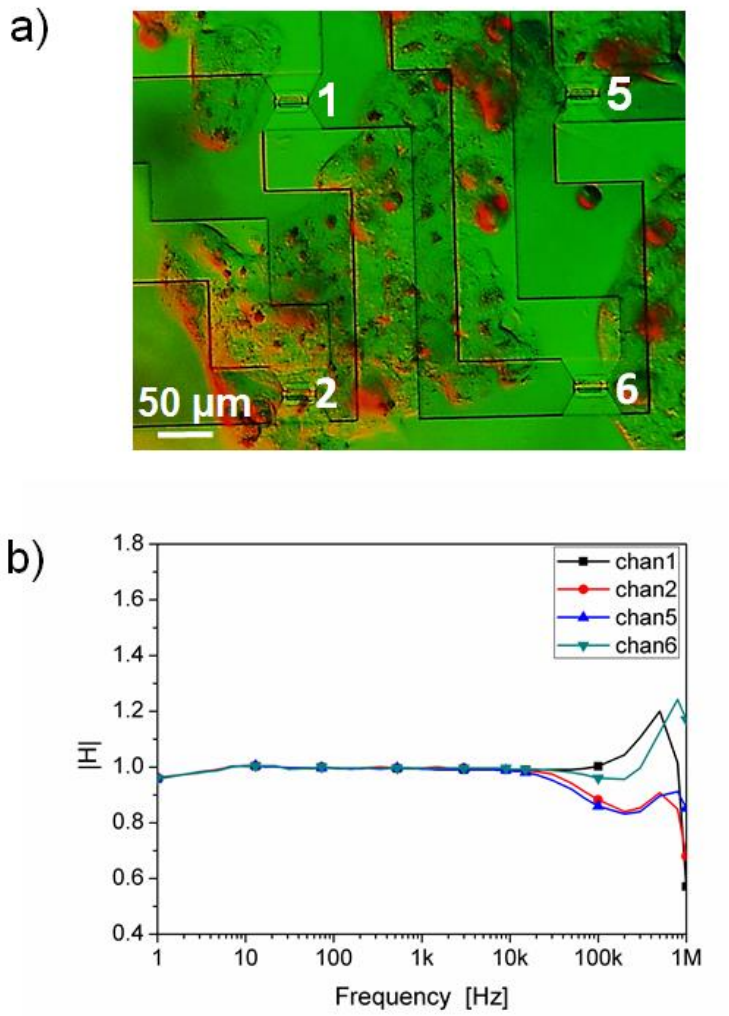

Figure 3-17 a) Microscopic image of 4 from 16 transistor gates of an FET device covered by H441 cells. Transistor gates 2 and 5 were cell-covered, whereas transitor gates 1 and 6 were cell-free. b) The transfer functions measured by the TTF amplifier system.

Afterwards, the transfer function measurements of the same FET device were performed with the newly developed amplifier system with the lock-in amplifier as well. The measured impedance spectra are plotted as bode diagrams with amplitude (Figure 3-18a) and phase (Figure 3-18b) components, respectively. In the case of cell-free transistor gate the amplitude of the transfer function increases in the frequency range between 200 and 400 kHz before approaching zero. In the case of cell-covered transistor gate the amplitude of the transfer function decreases in the frequency range between 30 and 100 kHz and in the frequency range between 100 and 400 kHz stays at a lower level and then goes down towards zero as well.

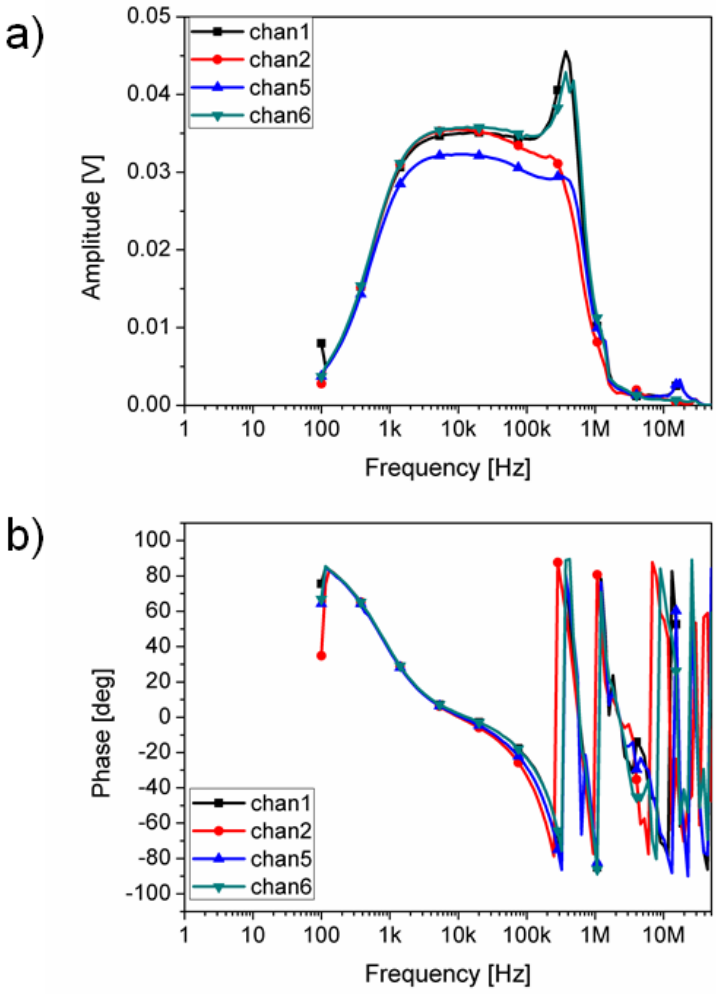

Figure 3-18 Recorded transfer functions in the range from 1 Hz to 50 MHz using the new amplifier system with a fast lock-in amplifier can be presented in form of a Bode plot with frequency-dependent a) amplitude and b) phase components.

The impedance spectra can be measured from 1 Hz to 50 MHz (Figure 3-18). Because of the fact that no changes appear in impedance spectra above frequencies of 1 MHz and due to a high-pass effect at low frequency ("HF2 User Manual," 2014), in the following the transfer functions measured with the lock-in amplifier system will be presented in the range of 1 kHz to 1 MHz. Moreover, the amplitude of the transfer functions will be normalized at frequency of 3 kHz (Figure 3-19).

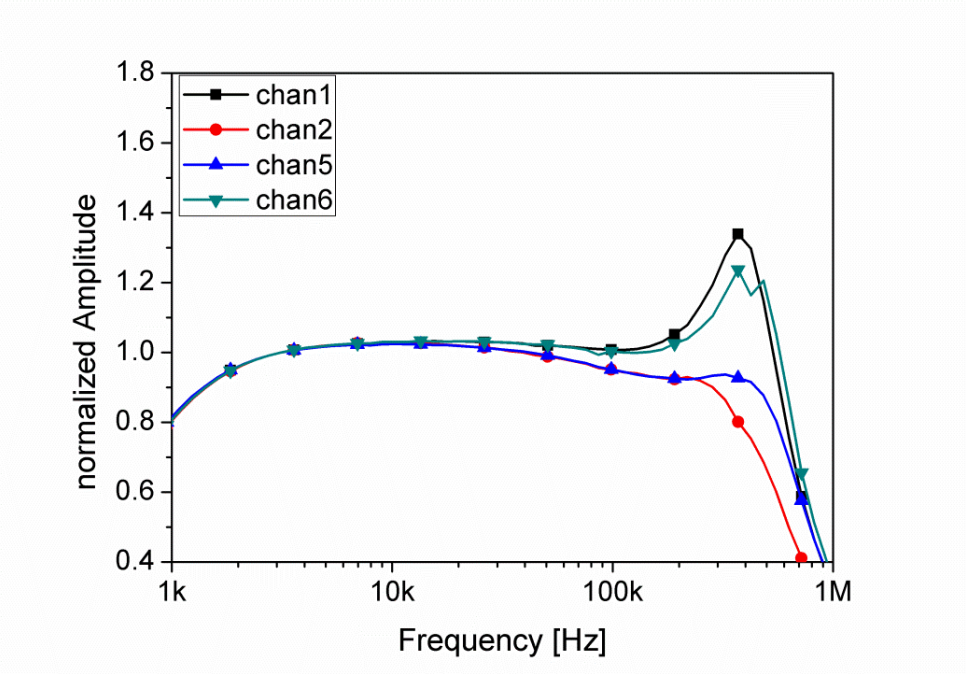

Figure 3-19 Normalized amplitude of the transfer functions at frequency of 3 kHz measured by the experimental setup with a fast lock-in amplifier in the range from 1 kHz to 1 MHz.

3.9 Influence of the transimpedance amplifier circuit on the impedance spectra

In this section, the influence of the transimpedance amplifier (section 2.6) on the impedance spectra measured with the lock-in amplifier system will be demonstrated. For this purpose, different operational amplifiers (op-amps) were tested, which differ from each other in bandwidth and slew rate. In Figure 3-20 the impedance spectra measured using two different operational amplifiers, namely OP97 (Distrelec Schuricht GmbH, Germany) and OPA627 (Distrelec Schuricht GmbH, Germany), in the transimpedance amplifier circuit are compared. The op-amp OP97 has the bandwidth of 0.9 MHz and the op-amp OPA627 of 16 MHz, respectively. The spectra were recorded using test-solutions of different concentrations of sodium chloride (1 mM NaCl, 10 mM NaCl, and 100 mM NaCl). As it can be seen in Figure 3-20, the selection of the operational amplifier has a strong influence on the recorded spectra. The bandwidth of the developed system was increased using the op-amp OPA627. In general, an operational amplifier with a higher bandwidth is preferred in order to increase the bandwidth

of the readout system and obtain the information about the condition of cells at higher frequency (Susloparova et al., 2013).

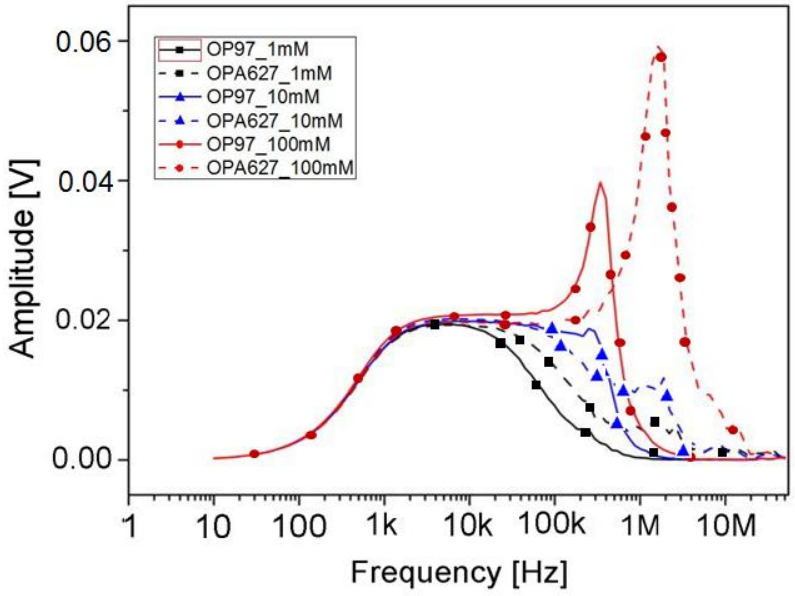

Figure 3-20 Comparison of the impedance spectra measured with the lock-in amplifier system using two different operational amplifiers, namely OP97 and OPA627, in the transimpedance amplifier circuit. The spectra were recorded using the electrolyte solutions of different concentrations of sodium chloride (NaCl). This image was adapted from (Susloparova et al., 2013).

3.10 Chip cleaning and surface modification

Before cells were cultured on the FET devices, these were cleaned and their surfaces were activated (Meyburg et al., 2007) (Wrobel et al., 2005). The FET devices are robust and can be re-used many times. First, the residues of the previous cell culture were removed from the chip surface with ethanol. Then, the chips were cleaned in an ultrasonic bath by two steps (in 2% Helmanex II (Hellma Analytics, Germany) and in distilled water, 5 min in each case). Afterwards the chip surfaces were activated by 20% sulfuric acid (H_2SO_4) (AppliChem GmbH, Germany) at 80° C for 30 min, subsequently rinsed with distilled water, and kept in 70% ethanol for 5 min for sterilization. Each FET surface was coated with 10 µl of 1 mg/ml

fibronectin (AppliChem GmbH, Germany) and incubated at 37 °C for 3 hours (NuAire Inc.). Before plating the cells, the surfaces were rinsed with distilled water.

3.11 Cell culture, drug treatment and chemicals

Two different cell lines, the human lung adenocarcinoma epithelial cell line H441 and the Human Embryonic Kidney HEK293 cell line, were used in this thesis. The H441 cells were grown in Roswell Park Memorial Institute medium (RPMI1640) supplemented with 1% L-glutamine, 10% Fetal Calf Serum (FCS) and 1% Penicillin/Streptomycin. The HEK293 cells were grown in standard Minimal Essential Medium (M10) supplemented with 10% FCS, 1% Non-Essential Amino Acid (NEAA), 1% Penicillin/Streptomycin and 1% L-glutamine. All chemicals were purchased from PAN Biotech GmbH, Germany. For the single cell experiments, a very low density of cells (3000 cells per FET device) was plated onto the device surface (2.8 mm in diameter). After 1 h of initial adherence, the chips were filled up with 200 µl of culture medium. All cell cultures were kept in an incubator at 37 °C with 5% CO_2. The measurements were typically performed after one day in vitro (DIV).

In order to induce detachment of the cells, trypsin (PAN Biotech GmbH, Germany) with a concentration of 5 µg/ml was used. For a second experiment this was lowered to 1 µg/ml in order to achieve a slower detachment process.

For drug-related experiments, cultured cells were treated with the apoptosis-inducing chemotherapeutic drug topotecan hydrochloride (Sigma Aldrich, St. Louis, Missouri, USA). To induce apoptosis of the cells, 200 µl of culture medium were exchanged by 200 µl of drug containing medium with a concentration of 10 µg/ml

Chapter 4

In this chapter, an electrically equivalent circuit (EEC) model, which describes the cell-sensor contact, will be introduced. This model is based on the so-called point contact model (Pancrazio et al., 1999) (Sprössler et al., 1999) (Regehr et al., 1989), which is described in section 2.7. For a full description of the transfer functions (impedance spectra) recorded in this work, the parasitic values of the devices feed lines and the frequency bandwidth of the transimpedance amplifier were included in the model. Thus, the developed EEC model is composed of cell-related, device-related and the transimpedance circuit parameters. By implementation of this EEC model in a PSpice simulation program for electrical circuits, the transfer functions (impedance spectra) of individual cells adhered on top of the FET devices can be simulated. The effect of the circuit parameters on the impedance spectra can be investigated by different simulations. Thus, the EEC model was utilized for investigation of the device-related parameters to optimize the FET device performance. Moreover, an analytical expression, which represents the transfer function of the EEC model, was proposed. By means of the derived analytical expression the measured impedance spectra can be fitted and the cell-related parameters can be extracted.

4 Electrically equivalent circuit model

In Figure 4-1 an electrically equivalent circuit (EEC) model is presented, which describes an FET device in contact with an adherent cell on top of the transistor gate and

includes a transimpedance amplifier stage. The cell membrane is typically divided into two parts, the free membrane (FM) and the junction membrane (JM) part, each represented by the membrane capacitance and the membrane resistance in a parallel configuration ($C_{FM,}$ R_{FM} and $C_{JM,}$ R_{JM}, respectively) (Ingebrandt et al., 2005) (Schatzthauer, 1998). Both parts are connected by an inner resistance R_{in} of the cell's interior. The electrolyte-filled cleft between the junction membrane and the transistor surface is forming a resistive path, which is represented by the seal resistance R_{seal}. The FET device is described by the gate oxide capacitance C_{ox}, the transconductance g_m, and the output resistance R_{DS}. The parasitic parameters of the FET device like contact line capacitances and series resistances of source and drain are contributing to the EEC with C_{source}, C_{drain}, and R_{source}, R_{drain}, respectively. The reference electrode and the electrolyte solution contribute in an ideal case only as resistive path to the circuit with a combined series resistance R_{el}. The transimpedance amplifier stage is represented by an operational amplifier and the feedback resistor $R_{feedback}$.

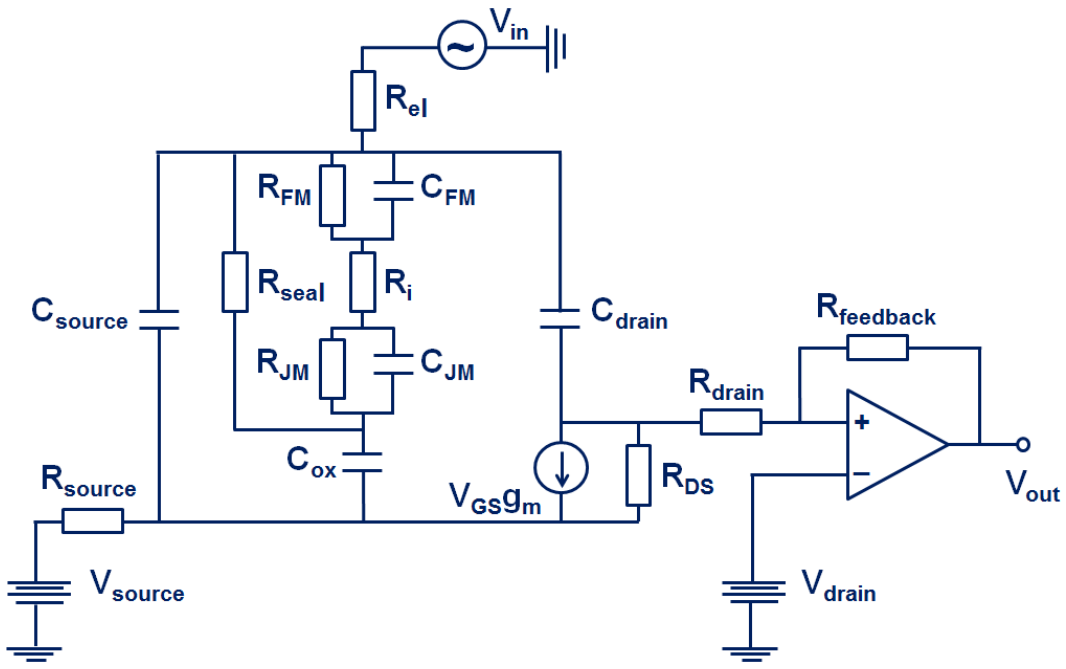

Figure 4-1 An electrically equivalent circuit, which describes an FET device in contact with an adherent cell on top of the transistor gate and which includes a transimpedance amplifier stage. All elements of the circuit are described in the text.

Typical values of the distance between the junction membrane and the transistor surface (cleft height) are in the range of several tens to 100 nm depending on the cell type and surface coating (Wrobel et al., 2008). These cleft height values correspond to values of 0.5–2 MΩ for the seal resistance. Compared to the typical membrane resistance values, which are in the range of several GΩ (Ingebrandt et al., 2005), the seal resistance value is usually much smaller. Therefore, the resistive path through the cell (R_{FM}, R_{in}, R_{JM}) can be neglected. The capacitances of both membrane parts connected in series can then be combined to:

$$C_M = \frac{C_{FM} \cdot C_{JM}}{C_{FM} + C_{JM}} \tag{4.1}$$

This combined capacitance C_M should, however, not be confused with the total membrane capacitance, which is typically measured by patch-clamp pipettes from inside to outside of a whole cell. The combined capacitance C_M is usually smaller than the typical whole-cell membrance capacitances of cells because of the serial combination of both membrane parts. Due to the facts stated above, the cell membrane can be composed of a resistive part through the cell-sensor cleft (R_{seal}) and a capacitive part through the cell (C_M) (Figure 4-2).

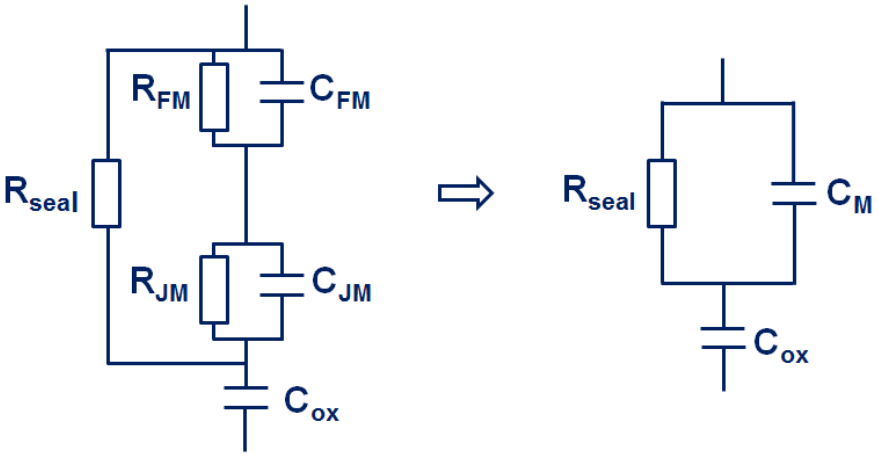

Figure 4-2 The part of the complete EEC, where the cell membrane is simplified into only two elements C_M and R_{seal}.

4.1 Analytical expression representing the transfer function

In this section, the detailed derivation of an analytical expression representing the transfer function of the simplified EEC model (Figure 4-3) will be presented. The analytical expression can be derived by applying Kirchhoff's laws and considering rules for combining of impedances in series and in parallel.

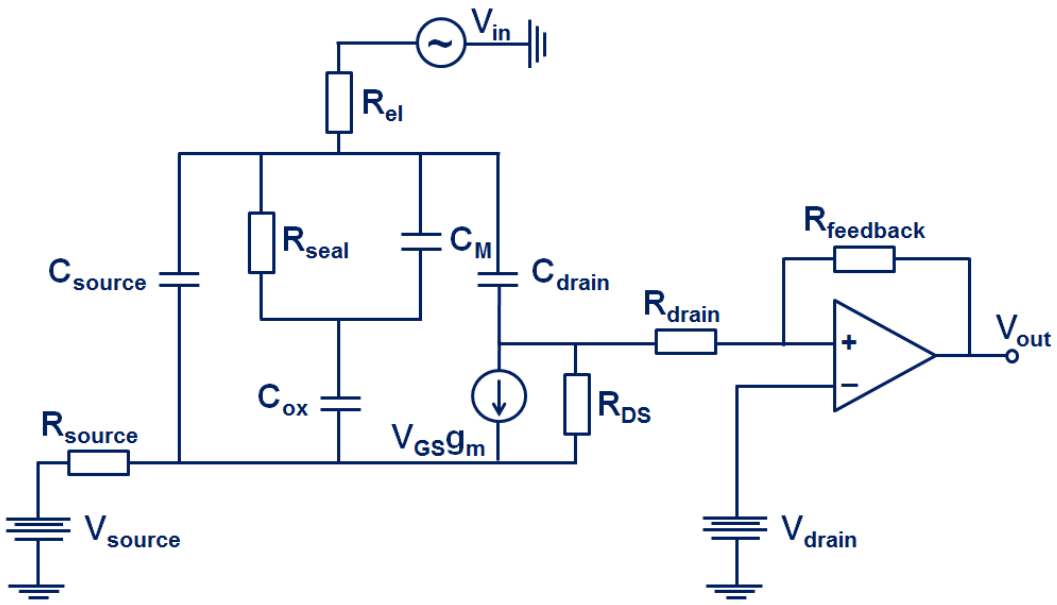

Figure 4-3 The simplified EEC model, which describes an FET device in contact with an adherent cell. The adherent cell can be modeled by two elements namely the combined membrane capacitance C_M and the seal resistance R_{seal}.

Unfortunately, this circuit cannot be further simplified since all elements play a role of the frequency responses.

A small sinusoidal signal V_{in} (jw) is applied to the reference electrode and the signal output V_{out} (jw) is measured after the transimpedance amplifier stage. Thus, the transfer function H(jw) is given by:

$$H(jw) = \frac{V_{out}(jw)}{V_{in}(jw)} \tag{4.2}$$

The output voltage is then given by:

$$V_{out}(jw) = -R_{feedback} I_{DS}(jw) \tag{4.3}$$

where $R_{feedback}$ is the feedback resistance in the transimpedance amplifier stage, $I_{DS}(jw)$ the drain-source current, w the angular frequency and j the imaginary unit.

In the following, an expression for $I_{DS}(jw)$ will be derived, which will then provide an analytical solution for the measured impedance spectra.

For reasons of clarity and comprehensibility, the gradually new inserted parameters will be entered in EEC model and denoted. Based on Kirchhoff's first law the drain-source current $I_{DS}(jw)$ is equal to:

$$I_{DS}(jw) = g_m V_{GS}(jw) - jwC_{drain} V_1(jw) \tag{4.4}$$

where $V_1(jw)$ is the voltage across the drain contact line capacitance C_{drain} (Figure 4-4).

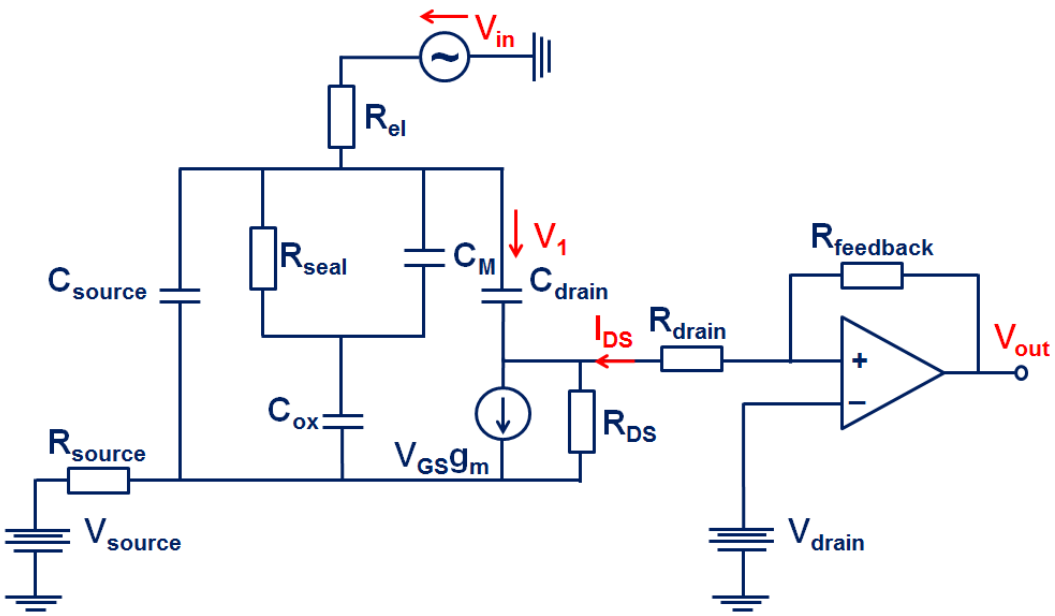

Figure 4-4 The simplified EEC model with the indicated drain-source current I_{DS} and the voltage V_1 across the drain contact line capacitance C_{drain}.

Two electrical components connected in parallel representing the cell membrane, the combined membrane capacitance C_M and the seal resistance R_{seal}, were combined to the impedance of the adherent cell Z_1 (Figure 4-5):

$$Z_1 = \frac{R_{seal}}{1 + jwR_{seal}C_M} \tag{4.5}$$

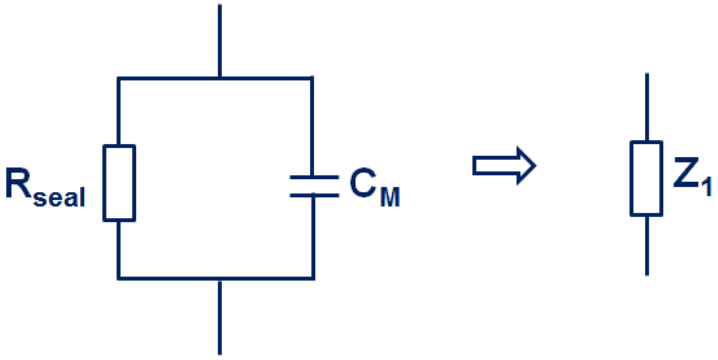

Figure 4-5 The combined membrane capacitance C_M and the seal resistance R_{seal} in a parallel configuration are combined to the impedance of the adherent cell Z_1.

Next, an electrical network (divider) composed of two electrical impedances in series, the impedance of the adherent cell Z_1 and the impedance of the gate oxide capacitance C_{ox}, was considered (Figure 4-6).

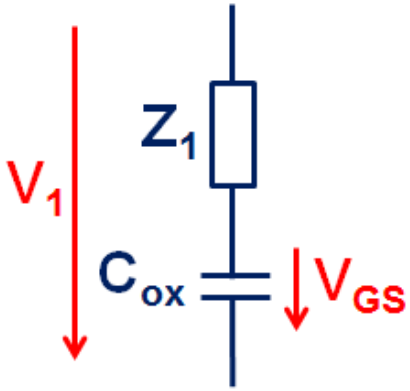

Figure 4-6 A divider composed of the impedance of the adherent cell Z_1 and the impedance of the gate oxide capacitance C_{ox} is shown in this graph.

This divider (Figure 4-6) has the voltage ratio:

$$\frac{V_1(jw)}{V_{GS}(jw)} = \frac{Z_1 + 1/jwC_{ox}}{1/jwC_{ox}} \tag{4.6}$$

From equation (4.6) and substituting equation (4.5), the gate-source voltage $V_{GS}(jw)$ can be found:

$$V_{GS}(jw) = V_1(jw)\frac{1+jwR_{seal}C_M}{1+jwR_{seal}(C_M+C_{ox})} \tag{4.7}$$

The resulting expression for the gate-source voltage can then be included into equation (4.4):

$$I_{DS}(jw) = V_1(jw)\left(g_m\frac{1+jwR_{seal}C_M}{1+jwR_{seal}(C_M+C_{ox})} - jwC_{drain}\right) \tag{4.8}$$

By performing simple mathematical conversions, the expression for the drain-source current is given by:

$$I_{DS}(jw) = g_m V_1(jw)\left(\frac{1+jw\left(R_{seal}C_M-\frac{C_{drain}}{g_m}\right)+w^2R_{seal}\frac{C_{drain}}{g_m}(C_M+C_{ox})}{1+jwR_{seal}(C_M+C_{ox})}\right) \tag{4.9}$$

This expression can be included into equation (4.3) and hence, the expression for the output voltage V_{out}(jw) can be found:

$$V_{out}(jw) = R_{feedback}g_m V_1(jw)\left(\frac{1+jw\left(R_{seal}C_M-\frac{C_{drain}}{g_m}\right)+w^2R_{seal}\frac{C_{drain}}{g_m}(C_M+C_{ox})}{1+jwR_{seal}(C_M+C_{ox})}\right) \tag{4.10}$$

Hence, the transfer function H(jw) (equation (4.2)) can be written as following:

$$H(jw) = R_{feedback}g_m\frac{V_1(jw)}{V_{in}(jw)}\left(\frac{1+jw\left(R_{seal}C_M-\frac{C_{drain}}{g_m}\right)+w^2R_{seal}\frac{C_{drain}}{g_m}(C_M+C_{ox})}{1+jwR_{seal}(C_M+C_{ox})}\right) \tag{4.11}$$

Next, the electrical components connected in parallel, the impedance of the source contact line capacitance $C_{source,}$ the impedance of the drain contact line capacitance C_{drain} and the impedance consisting of the impedance of the adherent cell Z_1 and the impedance of the gate oxide capacitance C_{ox} in series, are combined to one impedance Z_2 (Figure 4-7).

$$\frac{1}{Z_2} = jw(C_{source}+C_{drain}) + \frac{jwC_{ox}(1+jwR_{seal}C_M)}{1+jwR_{seal}(C_M+C_{ox})} \tag{4.12}$$

$$Z_2 = \frac{1+jwR_{seal}(C_M+C_{ox})}{jw(C_L+C_{ox})-w^2R_{seal}(C_L(C_M+C_{ox})+C_MC_{ox})} \tag{4.13}$$

where the capacitances of the source and drain contact lines can be combined to $C_L=C_{source}+C_{drain}$.

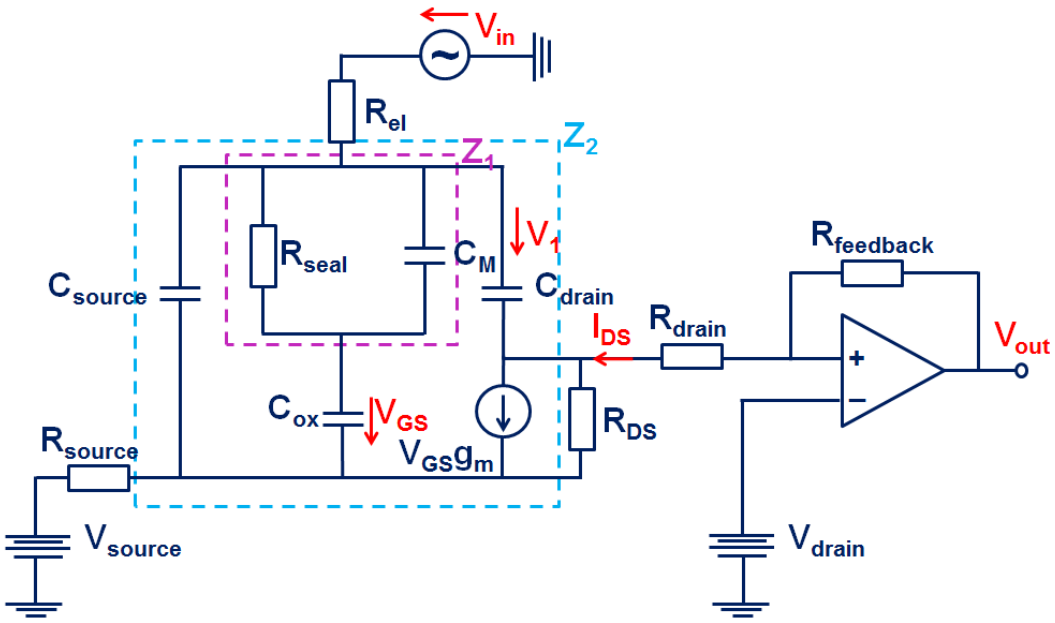

Figure 4-7 The electrical components connected in parallel, the impedance of the source contact line capacitance C_{source}, the impedance of the drain contact line capacitance C_{drain} and the combined impedance consisting of the impedance Z_1 and the impedance of the gate oxide capacitance C_{ox} in series, were combined to one impedance Z_2 across these the same voltage V_1 drops.

An electrical network (divider) composed of two electrical impedances in series, the impedance Z_2 and the impedance of the series resistance of the reference electrode and electrolyte solution R_{el}, was considered (Figure 4-8).

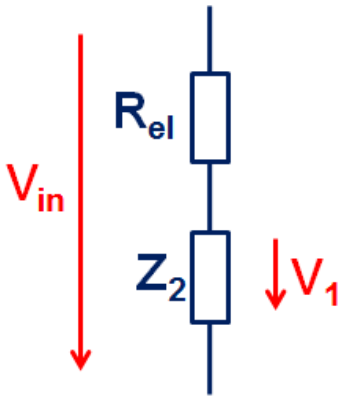

Figure 4-8 A divider composed of the impedance of the series resistance of the reference electrode and electrolyte solution R_{el} and the impedance Z_2 shown in this graph.

This divider has the voltage ratio:

$$\frac{V_{in}(jw)}{V_1(jw)} = \frac{R_{el}+Z_2}{Z_2} \tag{4.14}$$

The sum of two impedances R_{el} and Z_2 yields:

$$Z = R_{el} + Z_2 = \frac{1+jw\left(R_{el}\left((C_L+C_{ox})\right)+R_{seal}(C_M+C_{ox})\right)-w^2R_{el}R_{seal}(C_L(C_M+C_{ox})+C_MC_{ox})}{jw(C_L+C_{ox})-w^2R_{seal}(C_L(C_M+C_{ox})+C_MC_{ox})} \tag{4.15}$$

$$\frac{V_1(jw)}{V_{in}(jw)} = \frac{Z_2}{Z} = \frac{1+jwR_{seal}(C_M+C_{ox})}{1+jw\left(R_{el}\left((C_L+C_{ox})\right)+R_{seal}(C_M+C_{ox})\right)-w^2R_{el}R_{seal}(C_L(C_M+C_{ox})+C_MC_{ox})} \tag{4.16}$$

Finally, we need to consider the low pass characteristics of the first amplifier stage.

The equation (4.16) can be included into equation (4.11), which results in an analytical solution for the impedance spectra of a single cell in contact to an FET sensor:

$$H(jw) = R_{feedback}g_m \frac{1+jw\left(R_{seal}C_M-\frac{C_{drain}}{g_m}\right)-w^2\frac{R_{seal}C_{drain}}{g_m}(C_M+C_{ox})}{1+jw\left(R_{el}(C_L+C_{ox})+R_{seal}(C_M+C_{ox})\right)-w^2R_{el}R_{seal}(C_L(C_M+C_{ox})+C_MC_{ox})} \frac{1}{\sqrt{1+\left(\frac{f}{f_g}\right)^2}} \tag{4.17}$$

where f_g is the cutoff frequency of the operational amplifier, which takes the low pass effect of the transimpedance amplifier into account. This equation can now be used to fit the resulting TFF spectra in our experiments and to extract the adhesion-related data R_{seal} and C_M out of these spectra.

In the equation several parameters need to be considered, which result in the typical shape of the measured impedance spectra. These parameters can be divided in chip-related parameters, transimpedance circuit parameters, and cell-related parameters:

- device-related parameters: FET transconductance g_m, gate oxide capacitance C_{ox}, contact line capacitance C_L, which is a parallel combination of the drain and source capacitances C_{drain} and C_{source}
- transimpedance circuit parameters: series resistance of the reference electrode and electrolyte solution R_{el}, feedback resistance $R_{feedback}$ and cutoff frequency f_g of the operational amplifier
- cell-related parameters: combined membrane capacitance C_M and seal resistance R_{seal}

From equation (4.17) it can be seen that the relevant cell-related parameters are hidden inside a quite complicated expression. In our experiments we typically compare 'before' and 'after' measurements having either a cell attached to the FET gate or a completely free FET gate. Therefore, if the cell is completely detached, R_{seal} and C_M both become zero and the equation (4.17) condenses to:

$$H(jw) = R_{feedback} g_m \frac{1 - jw\frac{C_{drain}}{g_m}}{1 + jwR_{el}(C_L + C_{ox})} \frac{1}{\sqrt{1 + \left(\frac{f}{f_g}\right)^2}} \tag{4.18}$$

Using these two equations (4.18) and (4.17) the experimentally measured impedance spectra without and with cell on top of the transistor gate can be fitted and the cell-related parameters can be obtained.

4.2 Fitting procedure of the measured impedance spectra

In this section, the fitting procedure for the measured impedance spectra (without and with a single adhered cell on top of the transistor gate) will be demonstrated. The measured impedance spectra were fitted using the software Origin (OriginPro 9.0, OriginLab Corporation, Germany).

The measured impedance spectra without an adherent cell on top of the transistor gate can be fitted using equation (4.18). Thereby, some parameters of the EEC in this particular experiment can be extracted. For the fitting procedure realistic start values of the device-related parameters as well as the transimpedance circuit parameters were evaluated. Thus, the dimensions of the parasitic capacitances of source and drain contact lines C_{source} and C_{drain} can be estimated from the simple plate capacitor equation:

$$C_{source/drain} = \frac{\varepsilon_0 \varepsilon_{ox} A_{source/drain}}{d} \tag{4.19}$$

where ε_0 is the absolute permittivity of the vacuum ($\varepsilon_0 = 8.8542 \cdot 10^{-12}$ A·s/V·m), ε_{ox} is relative permittivity of silicon dioxide ($\varepsilon_{ox} = 3.9$), $A_{source/drain}$ is the area of the source or drain contact lines, and d is the respective thickness of the passivation layer, which are known from the fabrication process of the devices.

In a similar manner the gate oxide capacitance C_{ox} can be estimated by:

$$C_{ox} = \frac{\varepsilon\varepsilon_0 WL}{d_{ox}} \tag{4.20}$$

where W is the gate width, L is the gate length and d_{ox} is the thickness of the gate silicon oxide, which are all known from the fabrication process of the devices.

The transconductance value g_m of the FET device at its working point is known from the device characterization prior to each experiment.

The series resistance of the reference electrode and electrolyte solution R_{el} was estimated to 1 kΩ. The cutoff frequency f_g depends on the operational amplifier, which is used in the transimpedance circuit and on the value of the feedback resistor $R_{feedback}$ in the feedback loop. In the transimpedance amplifier circuit an operational amplifier OP97 (Distrelec Schuricht GmbH, Germany) and a feedback resistor of $R_{feedback}$ = 10 kΩ were used, which resulted in a value for f_g of 750 kHz.

Using these start values in the equation (4.18) the exemplary impedance spectrum measured for a cell-free transistor can be fitted (Figure 4-9). Thereby, one of the three device-related parameters (the gate oxide capacitance C_{ox}) as well as the transimpedance circuit parameters were fixed by fitting of the measured impedance spectrum for a cell-free transistor gate (Table 4-1) and two device-related parameters, namely, the contact line capacitance C_L = 92.19 pF ± 8.90 pF and the transconductance g_m = 0.194 mS ± 0.015 mS were obtained from the fit (error ranges are resulting from the fitting procedure).

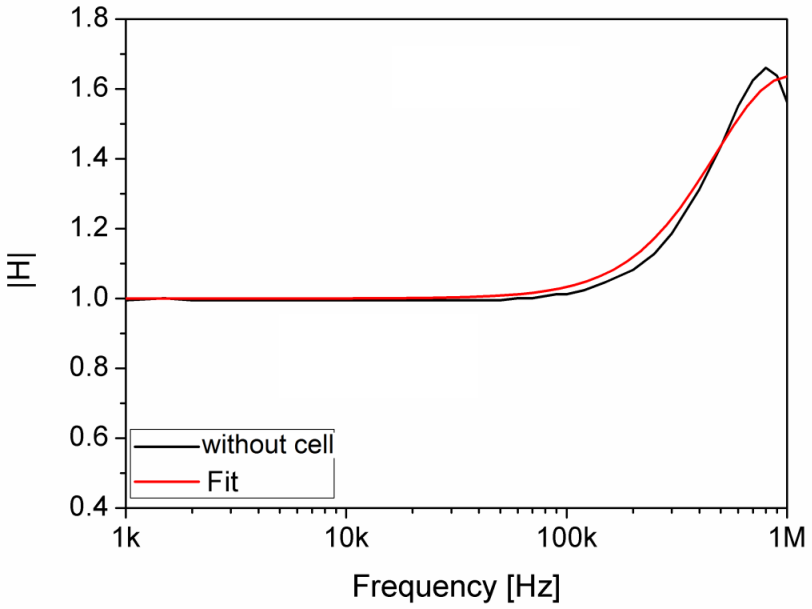

Figure 4-9 Exemplary fit of a measured impedance spectrum for a cell-free transistor gate using equation (4.18). The values of the contact line capacitance and the FET transconductance can be extracted to C_L = 92.19 pF ± 8.90 pF and g_m = 0.194 mS ± 0.015 mS, respectively, whereas the transimpedance circuit parameters were fixed (Table 4-1).

C_{ox} [pF]	R_{el} [kΩ]	$R_{feedback}$ [kΩ]	f_g [kHz]
0.28	1	10	750

Table 4-1 One of the three device-related parameters (namely the gate oxide capacitance C_{ox}) as well as the transimpedance circuit parameters (the series resistance of the reference electrode and electrolyte solution R_{el}, the feedback resistance $R_{feedback}$, and the cutoff frequency f_g of the operational amplifier OP97) were fixed during fitting of the measured impedance spectrum for a cell-free transistor gate (Figure 4-9).

Now the measured impedance spectrum of the same transistor covered with one HEK 293 cell can be fitted using equation (4.17). Thereby, the device-related parameters and the transimpedance circuit parameters were fixed (Table 4-2) and the cell related parameters (C_M and R_{seal}) for this single cell can be obtained. The fitted values of the seal resistance R_{seal} = 1.868 MΩ ± 0.149 MΩ and the cell membrane capacitance C_M = 1.211 pF ± 0.072 pF are in the ex-

pected range. As it can be seen in Figure 4-9 and Figure 4-10 the measured data and the fitted curves are in a good agreement.

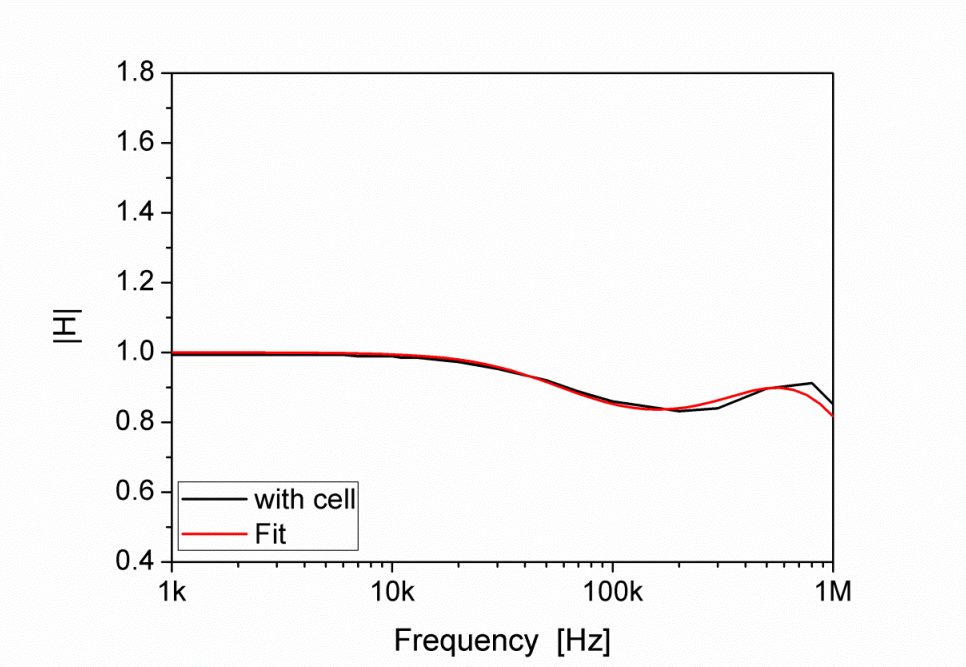

Figure 4-10 Exemplary fit of a measured impedance spectrum for a cell-covered transistor gate using equation (4.17). The values of the seal resistance and the cell membrane capacitance can be extracted to R_{seal} = 1.868 MΩ ± 0.149 MΩ and C_M = 1.211 pF ± 0.072 pF, respectively, whereas the device-related and the transimpedance circuit parameters were fixed (Table 4-2).

C_{ox} [pF]	g_m [mS]	C_L [pF]	R_{el} [kΩ]	$R_{feedback}$ [kΩ]	f_g [kHz]
0.28	0.2	92.2	1	10	750

Table 4-2 The values of the device-related parameters (the gate oxide capacitance C_{ox}, the transistor transconductance g_m and the contact line capacitance C_L) and transimpedance circuit parameters (the series resistance of the referene electrode and electrolye solution R_{el}, the feedback resistance $R_{feedback}$ and the cutoff frequency f_g of the operational amplifier OP97) were fixed during fitting of the measured impedance spectrum for a cell-covered transistor gate (Figure 4-10).

Such a combination of R_{seal} and C_M is characteristic for a typical cell-transistor contact and will vary with adhesion strength and cell shape, respectively.

4.3 Investigation of the effect of the cell-related parameters on the impedance spectra

In this section, the influence of the cell-related parameters on the impedance spectra in two idealized scenarios was systematically studied by simulations. The material contained in this section is based on a publication (Susloparova et al., 2015). For this purpose, the developed EEC model was implemented in PSpice, a program for electrical circuit simulation (OrCad Version 9.1, Cadence Design System Inc., San Jose, CA, USA). This is a much faster and easier procedure than the fitting procedure with the analytical expression as described in the last paragraph. Again two cases, namely, cell-free and cell-covered transistor gates were considered (Figure 4-11). The model for the ISFET device and the model for the respective operational amplifier were taken from a standard PSpice library (berkeley.lib and anlg_dev.lib, respectively). Typical values of the device-related and transimpedance circuit parameters used for all simulations in the following are displayed in Table 4-3, while the cell-related parameters were varied in a wide range.

C_{source} [pF]	C_{drain} [pF]	R_{source} [Ω]	R_{drain} [Ω]	W [µm]	L [µm]	g_m [mS]	C_{ox} [pF]	R_{el} [kΩ]	$R_{feedback}$ [kΩ]	operational amplifier
51	19	230	145	16	5	0.22	0.35	2	10	OP97

Table 4-3 The values of the device-related (the contact line capacitances and series resistances of source C_{source}, R_{source} and drain C_{drain}, R_{drain}, the gate width W, the gate length L, the transistor transconductance g_m, and the gate oxide capacitance C_{ox}) and transimpedance circuit parameters (the series resistance of the referene electrode and electrolye solution R_{el}, the feedback resistance $R_{feedback}$, and the operational amplifier OP97), which were kept constant for all performed simulations.

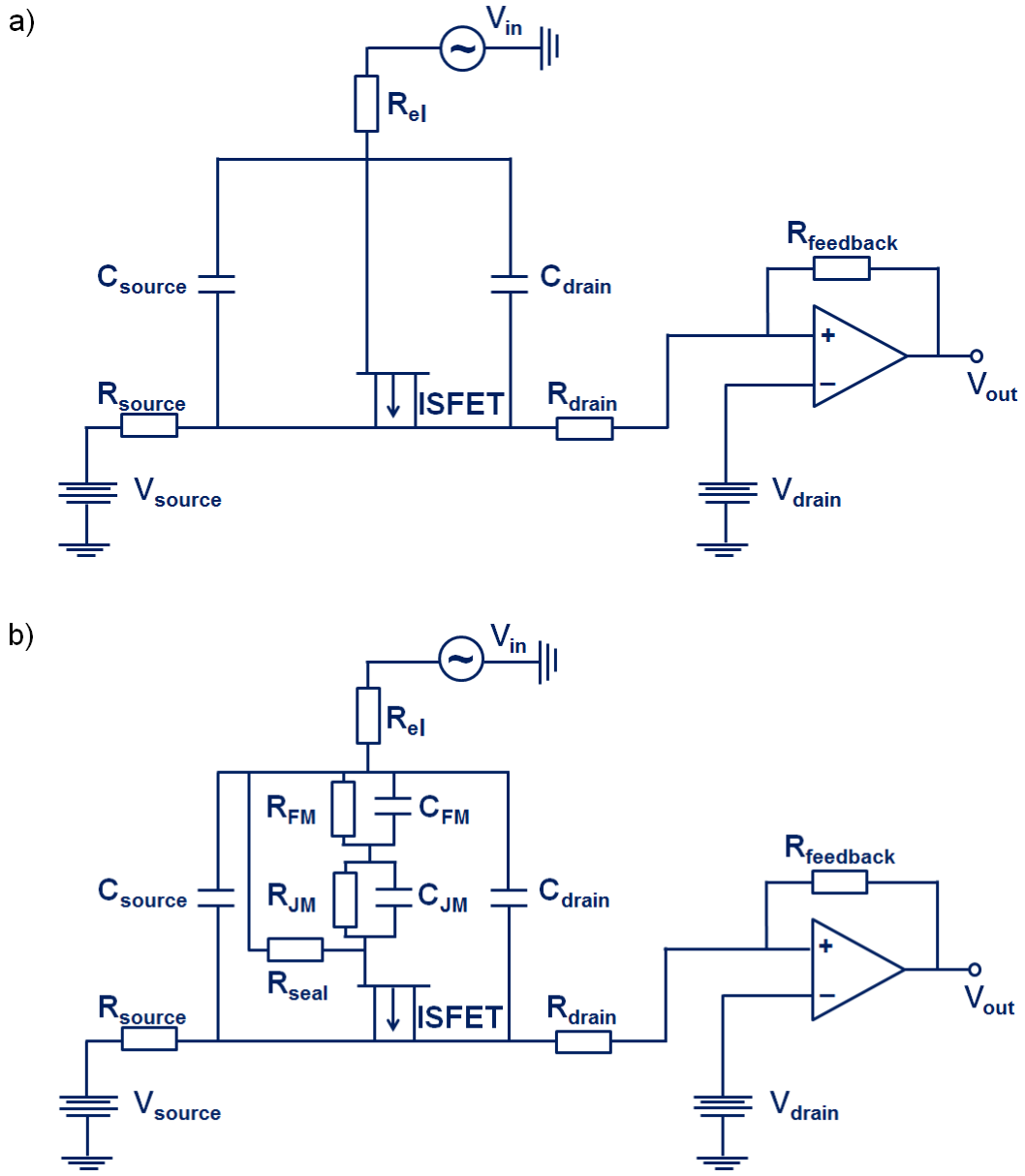

Figure 4-11 The electrically equivalent circuit model a) without and b) with cell on top of the transistor gate implemented in the PSpice simulation program.

4.3.1 Influence of the seal resistance R_{seal}

In Figure 4-12 modelling of an idealized cell detachment process from the transistor surface is shown. In this model the cell doesn't change its shape during the detachment process and is lifted up, stepwise.

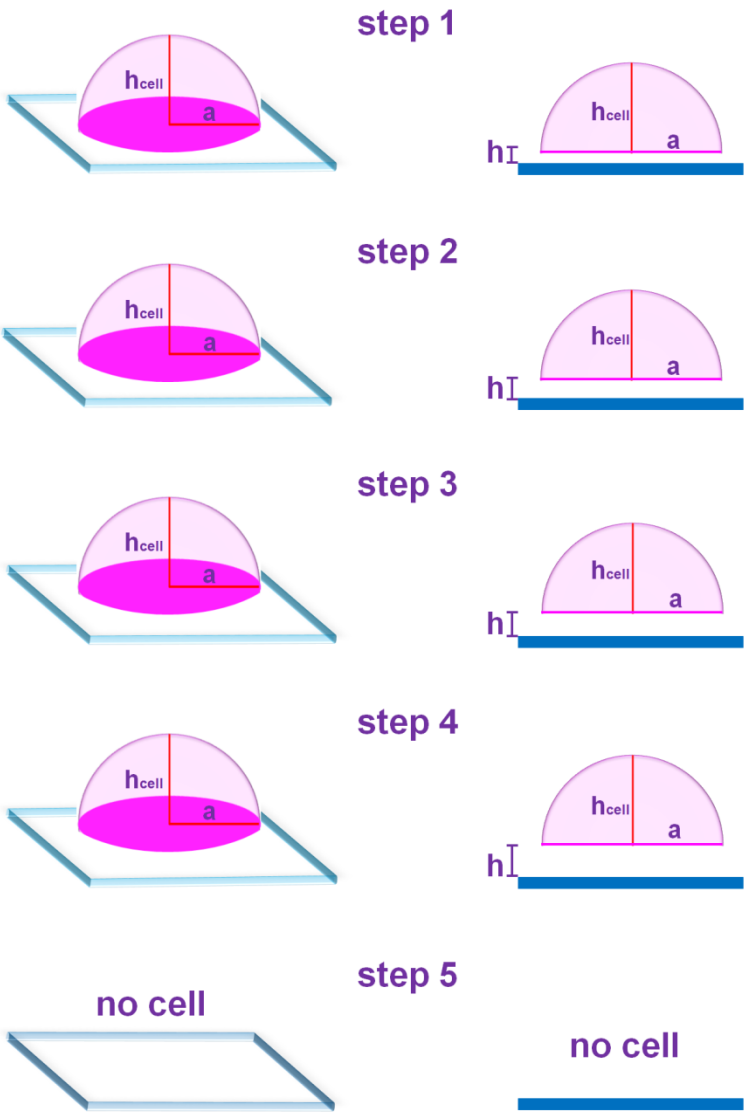

Figure 4-12 Modelling of the cell detachment process from the transistor surface in an idealized case. The cell doesn't change its shape during the detachment process, whereas the cleft height h was gradually increased.

The distance between the cell and the transistor surface (cleft height) h was gradually increased. As a result, the seal resistance R_{seal} was stepwise decreased in the circuit simulation. The values estimated for the steps can be obtained by following analytical equation (Pabst et al., 2007):

$$R_{seal} = \frac{k_B T}{4\pi e_0^2 n_{tot}^B D_{K^+} h}\left[1 + 4\frac{L_D^2}{r^2}\left(\frac{1}{I_0(r/L_D)} - 1\right)\right] \qquad (4.21)$$

where k_B is the Boltzmann constant (k_B = 1.38064852(79)·10^{-23} J/K), T the absolute temperature (T = 273.15 K), e_0 is the elementary charge (e_0 = 1.60217662·10^{-19} C), n_{tot}^B a particle

density of the surrounding bath solution (n_{tot}^{B} = $1.75 \cdot 10^{26} \cdot m^{-3}$), D_{K^+} the diffusion coefficient (D_{K^+} = $2.0 \cdot 10^{-9} \cdot m^2 \cdot s^{-1}$), h the cleft height, r the cell radius, I_0 the modified Bessel function, and L_D the Debye length.

In order to calculate the seal resistance values R_{seal} (Table 4-4), the bulk conductivity in the cell-surface adhesion cleft was assumed using the "bulk resistivity in cell adhesion" (BRICA) model. The BRICA model implies that the electrical properties of a cell-solid contact are determined by the geometry of contact and by the resistivity of the bath electrolyte (Gleixner and Fromherz, 2006).

By application of the equation (4.21) to the developed EEC, the ionic strength of the electrolyte solution was considered, which will result in a different value of n_{tot}^{B} and an average diffusion coefficient D for all ions carrying the test signal (K^+, Na^+, Cl^+). In a first approximation, the second term in the brackets of equation (4.21) can be neglected. In this case, the seal resistance R_{seal} primarily depends on the cleft height h, which is typically less than 100 nm for this cell type (Braun and Fromherz, 1998) (Wrobel et al., 2008).

step no.	**h [nm]**	**R_{seal} [kΩ]**
1	35	1051
2	50	735
3	70	525
4	90	408

Table 4-4 The seal resistance values R_{seal} depend directly on the cleft height h (Figure 4-12). Values were calculated using equation (4.21).

Figure 4-13 shows the simulated impedance spectra by varying R_{seal} in a range from 1 MΩ to 400 kΩ. As it can be seen, the increase of the seal resistance is leading to a regular increase of the signal amplitude in the frequency range between 20 and 200 kHz, while the complete removal of the cell can be clearly distinguished. This is very consistent with the spectral changes observed in the detachment experiments (section 4.7).

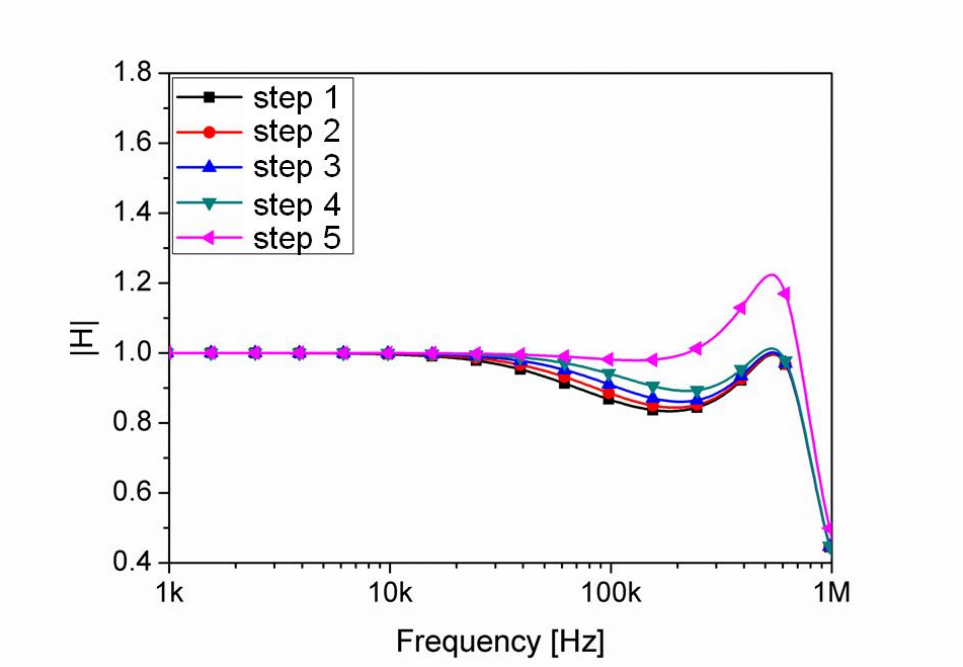

Figure 4-13 The simulated impedance spectra by varying of the seal resistance values in a wide range (from 1 MΩ (step 1) to 400 kΩ (step 4) (Table 4-4) (Figure 4-12), step 5 is for the case of a cell-free transistor (Figure 4-12)).

4.3.2 Influence of the combined membrane capacitance C_M

Changes in the combined membrane capacitance C_M can be estimated by simple geometrical considerations. This has been described earlier for HEK 293 cells. The amount of membrane area attached to the surface was reported to lie in the range of 30–45% depending on the coating material used (Sommerhage et al., 2008).

In Figure 4-14 a cell adhered to the transistor surface is approximated by a hemisphere and a gradually detaching cell from the transistor surface as different spherical caps. A morphological change of the cells led to an increase of the free membrane and a decrease of the attached membrane part, whereby the total surface area of the cell membrane was kept constant. In this simple model eventual swelling or shrinking of the cell which can of course also occur were neglected.

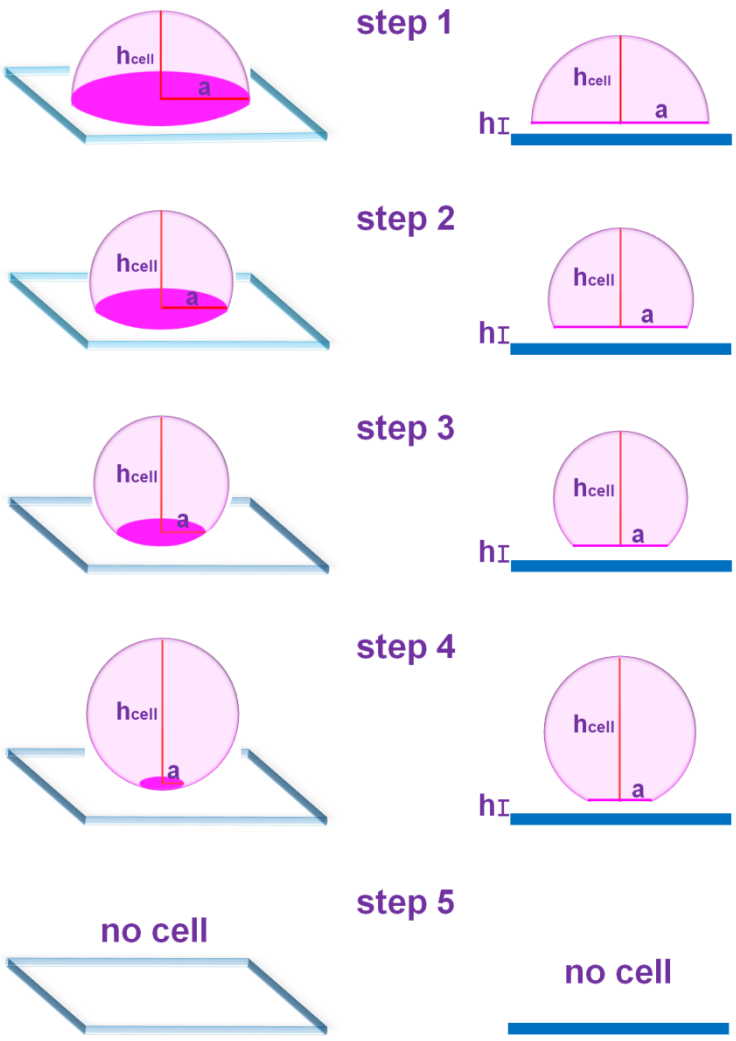

Figure 4-14 Modelling of an adherent cell to the transistor surface is shown in step 1. The gradually detached cell from the transistor surface is approximated by simple geometrical shapes (step 2 − step 4). The cell-free transistor surface is shown in step 5.

The area of the attached membrane part can be calculated with:

$$A_{JM} = \pi r^2 \tag{4.22}$$

where r is the radius of the flat disc in the attached membrane part.

The area of the free membrane part can be calculated with:

$$A_{FM} = \pi(a^2 + h_{cell}^2) \tag{4.23}$$

where a is the radius of the base of the cap and h_{cell} is the height of the cap.

The values for capacitance of the free and the attached membrane parts were calculated by using a specific membrane capacitance of 1 µF/cm^2 and the area of the attached membrane part A_{JM} or the free membrane part A_{FM} as follows:

$$C_{FM/JM} = 1\frac{\mu F}{cm^2}A_{FM/JM} \quad (4.24)$$

In Table 4-5 the calculated values for the radius of the flat disc attached to the surface (r), the radius of the base of the cap (a), the height of the cap (h_{cell}), as well as the area values (A_{FM} and A_{JM}), the capacitance values of the free and the attached membrane (C_{FM} and C_{JM}), and the corresponding values of the combined membrane capacitance (C_M) in each step are shown. The calculations were performed assuming that the diameter of the model cell is 20µm, which is resulting in a total membrane surface area of 942 µm^2. This value was kept constant for all detachment steps.

step no.	**r [µm]**	**a [µm]**	**h_{cell} [µm]**	**A_{JM} [µm^2]**	**A_{FM} [µm^2]**	**C_{JM} [pF]**	**C_{FM} [pF]**	**C_M [pF]**
1	10	10	10	314	628	3.14	6.28	2.09
2	7.5	7.5	13.7	176.63	765.38	1.77	7.65	1.44
3	5	5	15.8	78.5	863.5	0.79	8.64	0.72
4	2.5	2.5	19.9	19.63	922.38	0.19	9.22	0.19

Table 4-5 The capacitance values depend on the geometry of the cell. All elements are described in the text.

In Figure 4-15 the simulated impedance spectra for the gradually deformed cell are presented. The stepwise smaller capacitance values C_M for the cell membrane (Table 4-5) are leading to smaller absolute values in the spectra, which is an opposite effect compared to the seal resistance decrease during attachment. In addition, it can be seen that changes in the seal resistance generally have a larger effect on the shape of the impedance spectra.

In real experiments, of course both cell-related parameters will never vary independently. Therefore a fit to the EEC circuit model should be taken into account in any case extracting a combination of C_M and R_{seal} at particular time point during the detachment process (Susloparova et al., 2015).

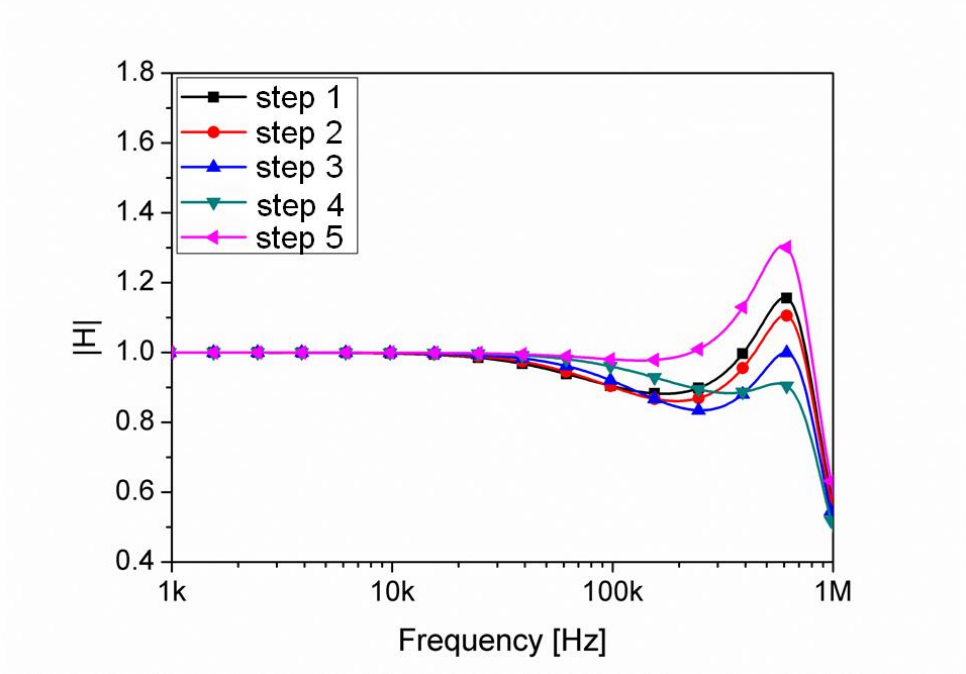

Figure 4-15 The simulated impedance spectra by varying of the capacitance values of the cell membrane for cell-covered transistor gate (step 1, C_{JM} = 3.14 pF, C_{FM} = 6.28 pF (Figure 4-14, Table 4-5)), transistor gate with the gradually detached cell (step 2 − step 4, C_{JM} = 1.77 pF, C_{FM} = 7.65 pF; C_{JM} = 0.79 pF, C_{FM} = 8.64 pF; C_{JM} = 0.19 pF, C_{FM} = 9.22 pF (Figure 4-14, Table 4-5)) and for cell-free transistor gate (step 5, (Figure 4-14)) are presented in the graph.

4.4 Investigation of the device-related parameters for optimization of the FET device performance

In this section, the application of the developed EEC model for optimization of a future chip design for better performance in cell-substrate adhesion experiments is described. The content shown in this section is based on a publication (Susloparova et al., 2014). The influence of the device-related parameters on the impedance spectra, like the transconductance value of the FET devices, the parasitic capacitances and resistances of source and drain contact lines as well as the influence of the surface topography, were investigated in different simulations.The obtained simulation results were used as design route for development and fabrication of a new generation of the FET devices in the framework of this thesis (subsection 3.1.2). Fabrication of the devices in the clean room facilities of the University of Applied Sciences Kaisers-

lautern in Zweibrücken, Germany, was done by Dr. Xuan Thang Vu according to a design obtained from these simulations.

4.4.1 Influence of the transistor transconductance g_m

It is commonly known, that a high transconductance value g_m of an FET device is significantly important for optimum signal transmission and amplification. In turn the transistor transconductance g_m is dependent on the electron mobility in the channel μ_p, the gate oxide thickness d_{ox}, the channel dimensions length L and width W, and the drain-source voltage V_{DS} as follows:

$$g_m = \mu_p C_{ox} \frac{W}{L} V_{DS} \qquad (4.25)$$

Firstly, the influence of the gate oxide capacitance C_{ox} on the transistor transconductance g_m and consequently on the impedance spectra with and without cell on top of the transistor gate was considered. For the simulations a simplified cell model as described in section 4.1 was used. The gate oxide capacitance is inversely proportional to the thickness of the silicon dioxide d_{ox} (equation (4.20)). This means that with a thinner gate oxide, higher gate oxide capacitance and consequently a higher transconductance of the FET devices is obtained. However, since the devices should stably operate in an electrolyte solution, a lower limit of the gate oxide thickness of about 6 nm dry oxide was used. In Table 4-6 the calculated gate oxide capacitance values using equation (4.20) for different gate oxide thicknesses and the corresponding transconductance values are presented. The transconductance values were obtained from the performed simulations of the transfer characteristics for a typical FET device with the channel length of 5 µm and the channel width of 16 µm and the indicated gate oxide thicknesses.

d_{ox} [nm]	C_{ox} [pF]	g_m [mS]
12	0.23	0.236
10	0.28	0.243
8	0.35	0.248
6	0.46	0.251

Table 4-6 The calculated gate oxide capacitance C_{ox} values for different gate oxide thicknesses d_{ox} and the transconductance g_m values obtained from the performed simulations for an FET device with the channel length of 5 µm and the channel width of 16 µm.

In Figure 4-16 the simulated impedance spectra with and without model cell on top of the transistor gate with different gate oxide thicknesses (from 12 nm to 6 nm) are compared. The simulations were performed by varying only one EEC model parameter, namely the gate oxide capacitance, while all other EEC model parameters were kept constant (Table 4-7). For simulations of the EEC, a standard cell with a seal resistance R_{seal} = 1 MΩ, an attached membrane capacitance of C_{JM} = 3.14 pF, and a free membrane capacitance of C_{FM} = 6.28 pF was included. The comparison is started with the PSpice model of an FET device from the previous design, for which the parameters were known from earlier experiments (gate area 5×16 μm^2, parameters for contact lines extracted from the design: C_{source} = 34 pF, C_{drain} = 13 pF, R_{source} = 230 Ω, R_{drain} = 145 Ω).

C_{FM} [pF]	C_{JM} [pF]	R_{seal} [MΩ]	C_{source} [pF]	C_{drain} [pF]	R_{source} [Ω]	R_{drain} [Ω]	W [µm]	L [µm]	R_{el} [kΩ]	$R_{feeedback}$ [kΩ]	op-amp
6.28	3.14	1	34	13	230	145	16	5	2	10	OP97

Table 4-7 The values of the EEC model parameters, which were kept constant for the simulations of the impedance spectra by varying of the gate-oxide capacitance values. The model cell is represented by typical values of a hemispherical cell with 20 µm diameter and about 35 nm cleft height (step 1 of the model described in Figure 4-12).

As it can be seen from the Figure 4-16, the values of the inflection point as well as the peak of the transfer functions get smaller (Table 4-8). Thereby the difference in impedance spectra with and without cell on top of the transistor gate increases in size.

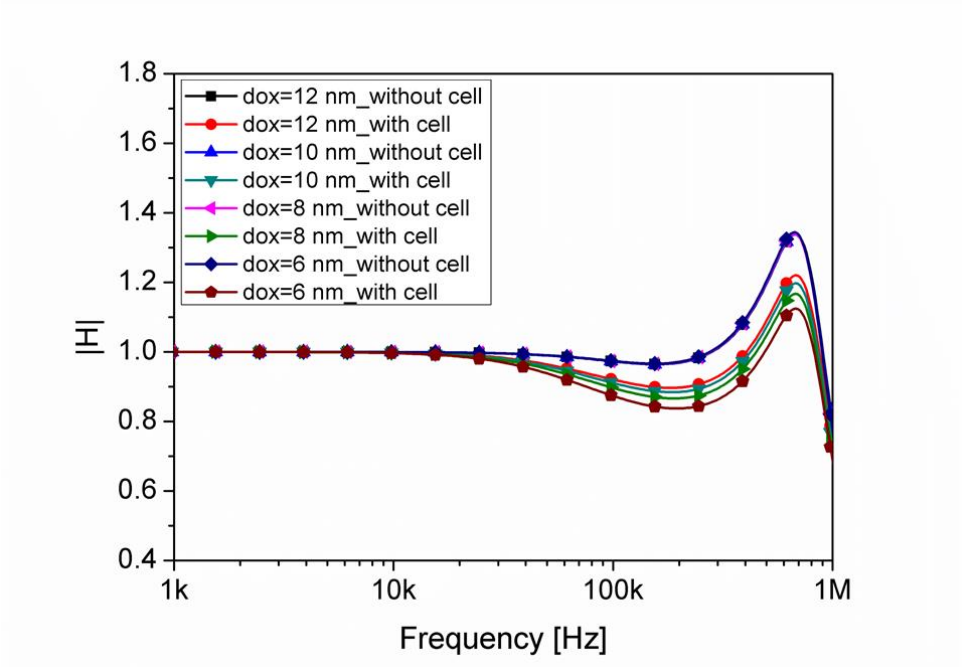

Figure 4-16 The simulated impedance spectra with and without cell on top of the transistor gate for an FET device with the channel length of 5 µm and the channel width of 16 µm by varying of the gate oxide thicknesses d_{ox}.

d_{ox} [nm]	inflection point	peak
12	0.898	1.219
10	0.886	1.197
8	0.865	1.167
6	0.835	1.123

Table 4-8 The values of the inflection point and the peak of the transfer functions for the corresponding gate oxide thickness d_{ox} (Figure 4-16).

In the following, the effect of the gate dimensions on the transistor transconductance and consequently on the impedance spectra with and without cell on top of the transistor gate was investigated. In Figure 4-17 and Figure 4-18 the simulated transfer characteristics $I_{DS}(V_{GS})$ and the corresponding transconductance g_m of two FET devices with different gate areas

namely 5×16 μm^2 and 5×25 μm^2 are presented, respectively. The transfer characteristic curves result from the FET model implemented in PSpice.

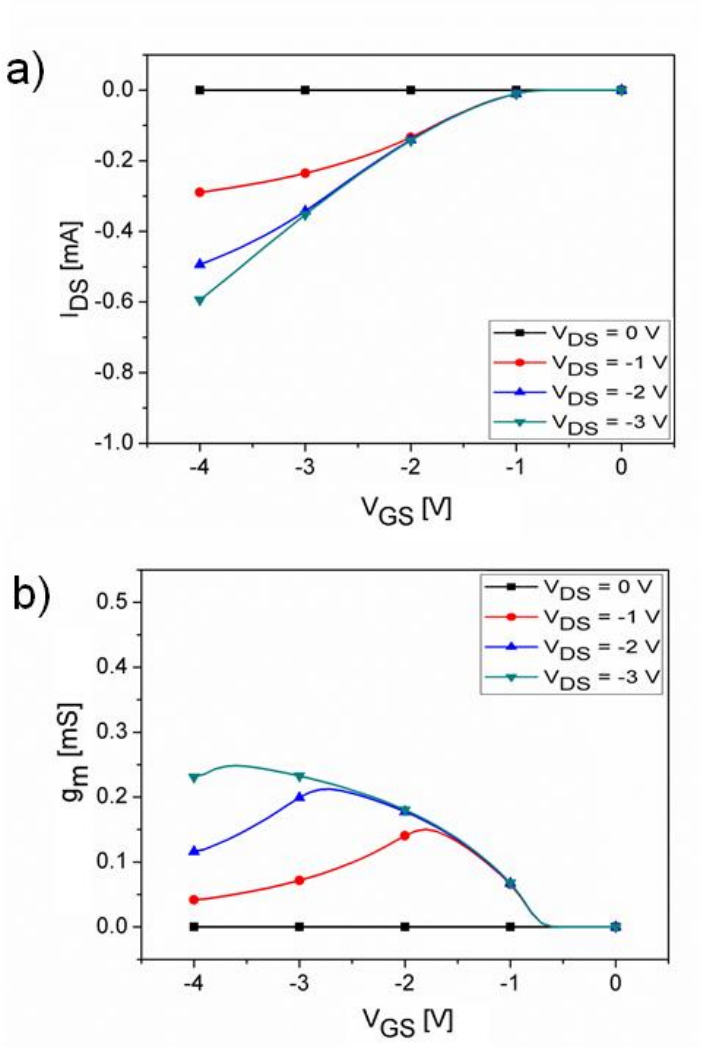

Figure 4-17 The simulated a) transfer characteristics $I_{DS}(V_{GS})$ of an FET device with the channel length of 5 μm and the channel width of 16 μm and the corresponding b) transconductance g_m.

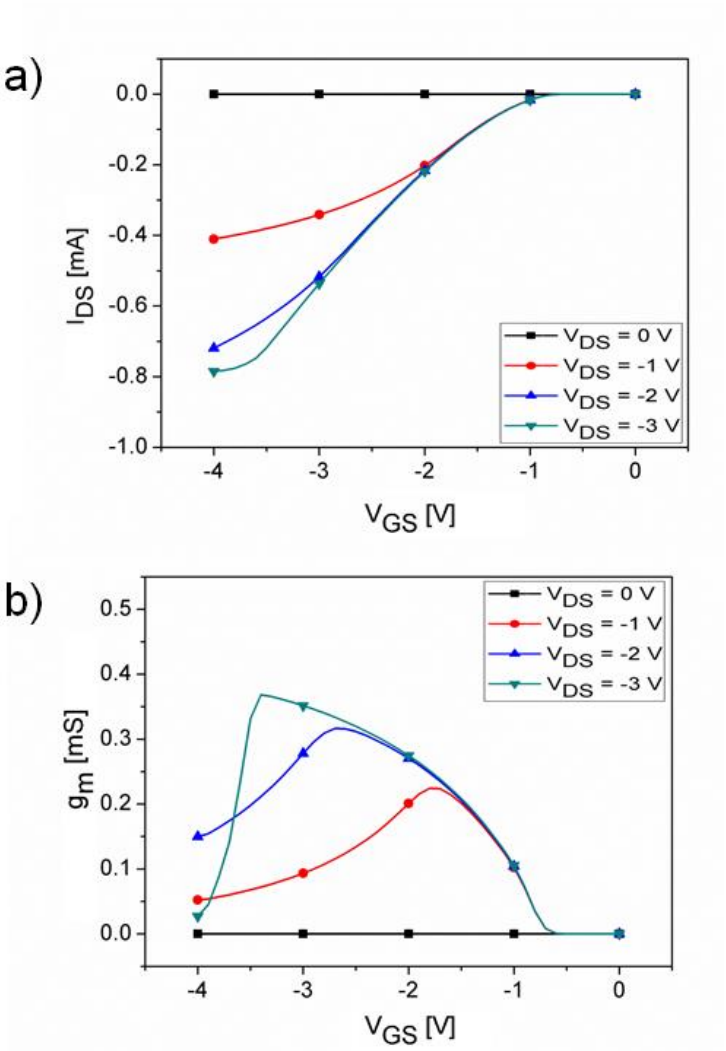

Figure 4-18 The simulated a) transfer characteristics $I_{DS}(V_{GS})$ for an FET device with the channel length of 5 µm and the channel width of 25 µm and the corresponding b) transconductance g_m.

The increase of the ratio of gate width to gate length (W/L ration from 3.2 to 5) leads to the increase of the transistor transconductance g_m from 0.22 mS (W = 16 µm, L = 5µm, V_{DS} = − 2 V, V_{GS} = − 2.8 V) to 0.33 mS (W = 25 µm, L = 5µm, V_{DS} = − 2 V, V_{GS} = − 2.8 V). The simulations were performed by varying of the transistor dimensions, while the other EEC model parameters were kept constant refer to (Table 4-9).

C_{FM} [pF]	C_{JM} [pF]	R_{seal} [kΩ]	C_{source} [pF]	C_{drain} [pF]	R_{source} [Ω]	R_{drain} [Ω]	R_{el} [kΩ]	$R_{feeedback}$ [kΩ]	op-amp
6.28	3.14	1	34	13	230	145	2	10	OP97

Table 4-9 The values of the EEC model parameters, which were kept constant for the simulations of the impedance spectra by varying of the transistor gate dimensions.

In Figure 4-19 the simulated impedance spectra with and without cell on top of the transistor with different gate areas, namely 5×16 µm^2 and 5×25 µm^2, are compared. As a result the spectra are shifting to lower frequencies and the difference in the impedance spectra simulated for the case of the cell-free as well as the cell-covered transistor gates is increasing. From our simulations we can conclude that for optimum impedance performance of our ISFETs for cell adhesion experiments, we need to increase the transconductance value g_m by either a thinner gate oxide layer d_{ox} or by increasing the W/L value of the design.

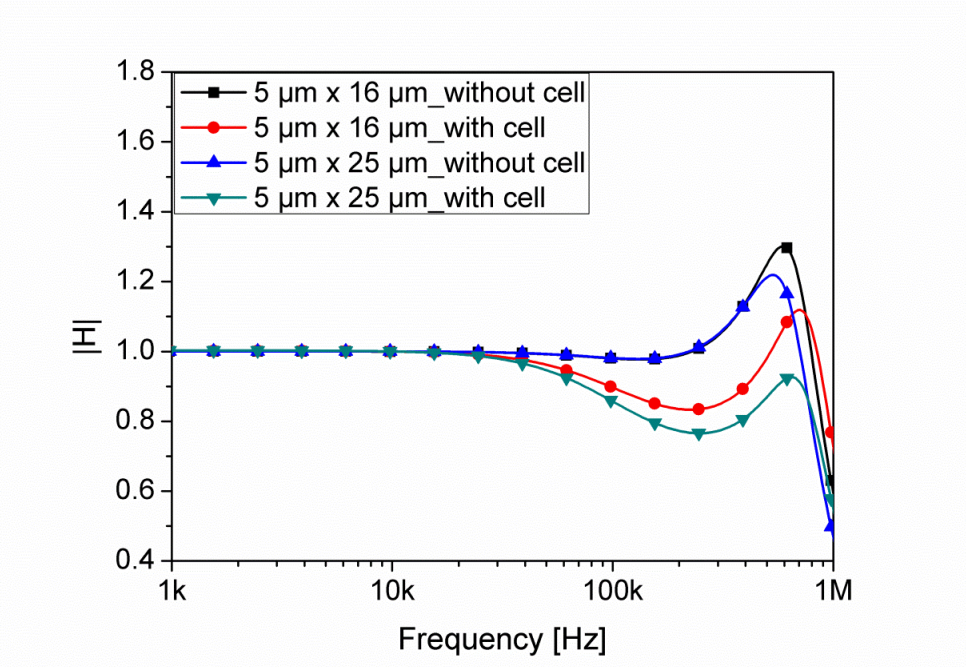

Figure 4-19 Simulated impedance spectra with and without cell on top of the transistor gate considering different transistor gate dimensions, namely 5×16 µm^2 and 5×25 µm^2.

4.4.2 Influence of the contact line capacitances C_{source} and C_{drain}

In the following paragraph, the effect of the contact line capacitances on the impedance spectra was considered. The parasitic capacitances of source and drain contact lines (C_{source} and C_{drain}) can be calculated from the contact line areas of source and drain (A_{source} and A_{drain}**)**, which are usually known from the design, and the thickness of the passivation layer d using equation (4.19). In Table 4-10 the calculated capacitance values for different thicknesses of the passivation layer and the indicated contact line areas for source and drain are displayed.

d [nm]	**A_{source} [µm^2]**	**A_{drain}[µm^2]**	**C_{source} [pF]**	**C_{drain} [pF]**
450	448 000	165 000	34	13
220	448 000	165 000	67	25

Table 4-10 The capacitance values of the contact lines for source C_{source} and drain C_{drain} for different thicknesses of the passivation layer d. Values were calculated based on the contact line areas A_{source} and A_{drain} and the passivation layer thicknesses d of both designs.

In Figure 4-20 the simulated impedance spectra with different silicon dioxide thicknesses for the passivation layer are presented. As it can be seen from the Figure 4-20, with increase of the contact line capacitances the peak of the transfer function after the inflection point shifts to lower frequency and to lower amplitude values. However, the difference between the cell-adhered and the cell-free case is decreasing as well. Therefore, generally higher contact line capacitances and hence thinner passivation layers are preferred, if we intend to work with low-frequency electronics.

C_{FM} [pF]	**C_{JM} [pF]**	**R_{seal} [kΩ]**	**W [µm]**	**L [µm]**	**C_{ox} [pF]**	**R_{el} [kΩ]**	**$R_{feeedback}$ [kΩ]**	**op-amp**
6.28	3.14	1	16	5	0.35	2	10	OP97

Table 4-11 The values of the EEC model parameters, which were kept constant for the simulations of the impedance spectra by varying of the contact line parameters.

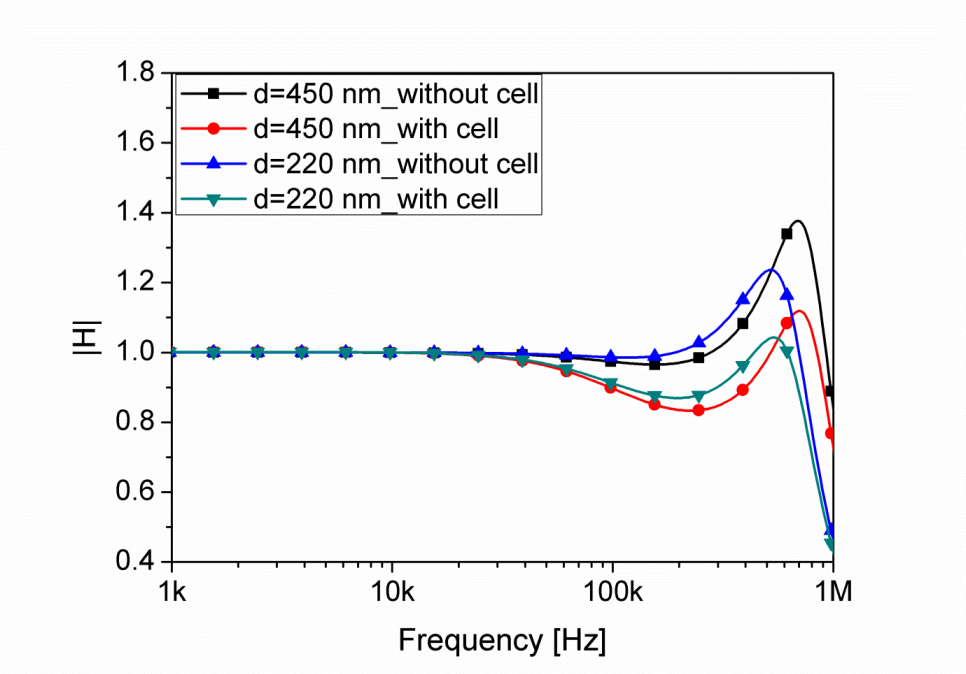

Figure 4-20 The simulated impedance spectra with and without cell on top of the transistor gate considering different thicknesses of the passivation layer d are presented in this graph.

Based on these simulation results we decided to increase the implantation dose of the contact lines, to decrease the passivation layer thickness to 220 nm silicon oxide and to use only 6 nm gate oxide thickness for the new generation of the FET devices.

4.4.3 Influence of the surface topography

For cell adhesion and migration experiments, the surface topography is very important. The flatter the transistor surface is, the stronger the electronic coupling strength becomes (Voelker and Fromhertz, 2006). A reduced cleft height between the cell and the transistor will lead to an increase of the seal resistance R_{seal}, which is inversely proportional to the cleft height (equation (4.21)). In Figure 4-21 the simulated impedance spectra for the cases of the cell-free as well as the cell-covered transistor gates are presented. For the case of the cell-covered transistor gate different coupling strengths (R_{seal}) were considered (0.8 MΩ, 1.0 MΩ, 1.2 MΩ). As it can be seen in Figure 4-21, for the higher seal resistance values the amplitude of the transfer functions begins to decrease earlier than for the smaller values, whereas the inflection point

shifts to lower amplitude values. This indicates the increase of the difference in impedance spectra with and without cell on top of the transistor. Therefore, higher R_{seal} values are generally preferred (Susloparova et al., 2014).

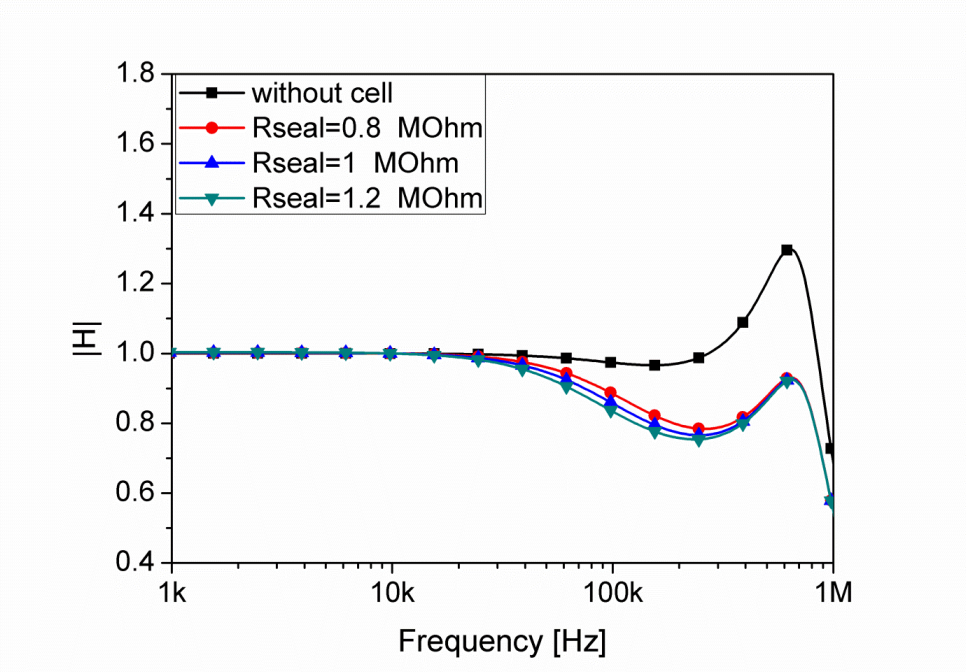

Figure 4-21 The impedance spectra simulated for the cases of a cell-free as well as a cell-covered transistor gate considering different coupling strengths (R_{seal}).

4.5 Investigation of the effect of the transimpedance circuit parameters on the impedance spectra

In this section, the influence of the transimpedance circuit parameters on the impedance spectra was investigated. Again the model circuit implemented in PSpice was used.

Firstly, the influence of the series resistance of the reference electrode and electrolyte solution R_{el} on the shape of the impedance spectra was investigated. In Figure 4-22 the impedance spectra, which were simulated for the case of the cell-covered transistor gate, by varying of the values of the reference electrode and electrolyte solution from 100 Ω to 2 kΩ were compared. As it can be seen from the Figure 4-22, the higher the resistance of the reference electrode and electrolyte solution, the smaller is the increase of the transfer functions at the peak position at about 800 kHz.

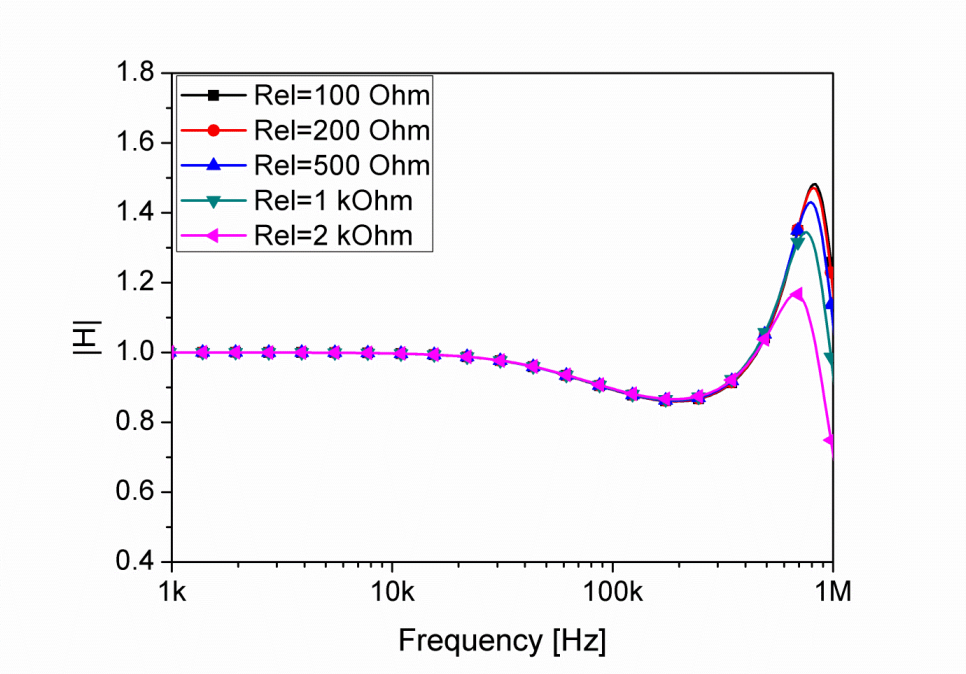

Figure 4-22 The impedance spectra simulated for the case of the cell-covered transistor gate considering the series resistance of the reference electrode and electrolyte solution R_{el} from 100 Ω to 2 kΩ.

In Figure 4-23 the impedance spectra, which were simulated for the cases of the cell-free as well as the cell-covered transistor gates, using different operational amplifiers were compared. The operational amplifiers differ from each other in bandwidth and slew rate (Table 4-12).

op-amp	Bandwidth [MHz]	Slew rate [V/µs]
OP97	0.9	0.2
OP37	63	17

Table 4-12 The operational amplifiers (OP97 and OP37 (Distrelec Schuricht GmbH, Germany)) differ from each other in bandwidth and slew rate.

As it can be seen, using of the operational amplifier with a higher bandwidth leads to an increased bandwidth of the readout system. Thus, the information about the condition of cells can be obtained at higher frequencies.

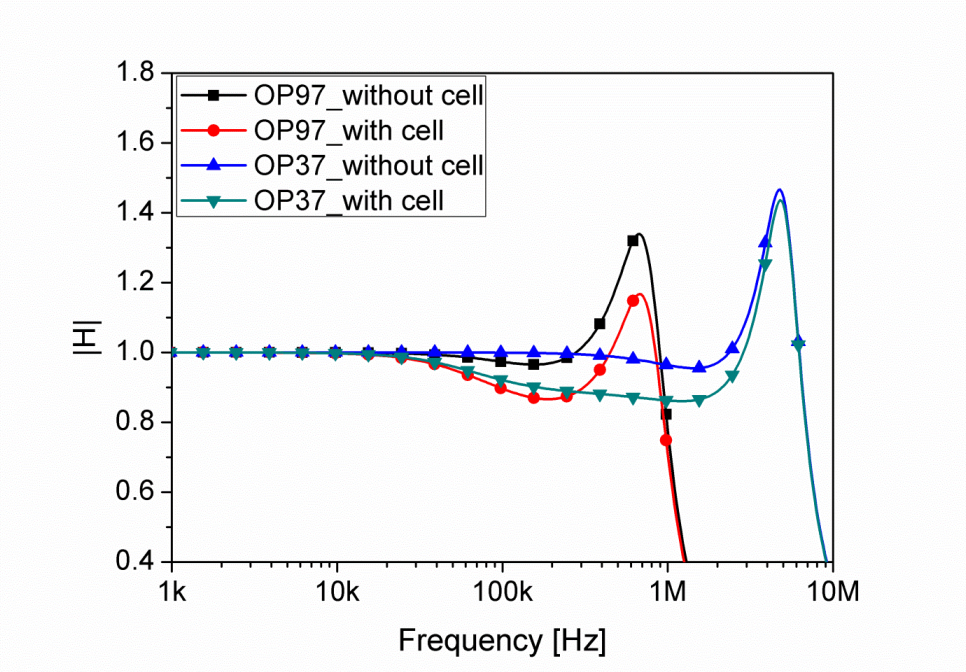

Figure 4-23 The simulated impedance spectra with and without cell on top of the transistor gate using different operational amplifiers, namely OP97 and OP37.

4.6 Mechanical removal of an individual cell from the transistor gate surface

In this section, experiments were performed on a patch-clamp setup to confirm that only one individual cell adhered to a transistor gate of an FET device causes the changes in the impedance spectra.

For these experiments, the HEK293 cells were cultured in a low density on the FET device surfaces. In Figure 4-24a, as an exemplary experiment two transistor gates of an FET device, cell-free transistor gate (number 7) and single cell-covered transistor gate (number 8), are shown. First, the impedance spectra of both transistor gates were recorded using the lock-in amplifier system (subsection 3.7.2). Afterwards, the cell was mechanically removed from the transitor gate surface (number 8) by a patch-clamp pipette (Figure 4-24c) and the impedance spectra were recorded again. The measured impedance spectra before and after removal of the cell are compared in Figure 4-24b. A significant change in the impedance spectra shape was observed confirming experimentally the theoretical model discussed in section 4.3.

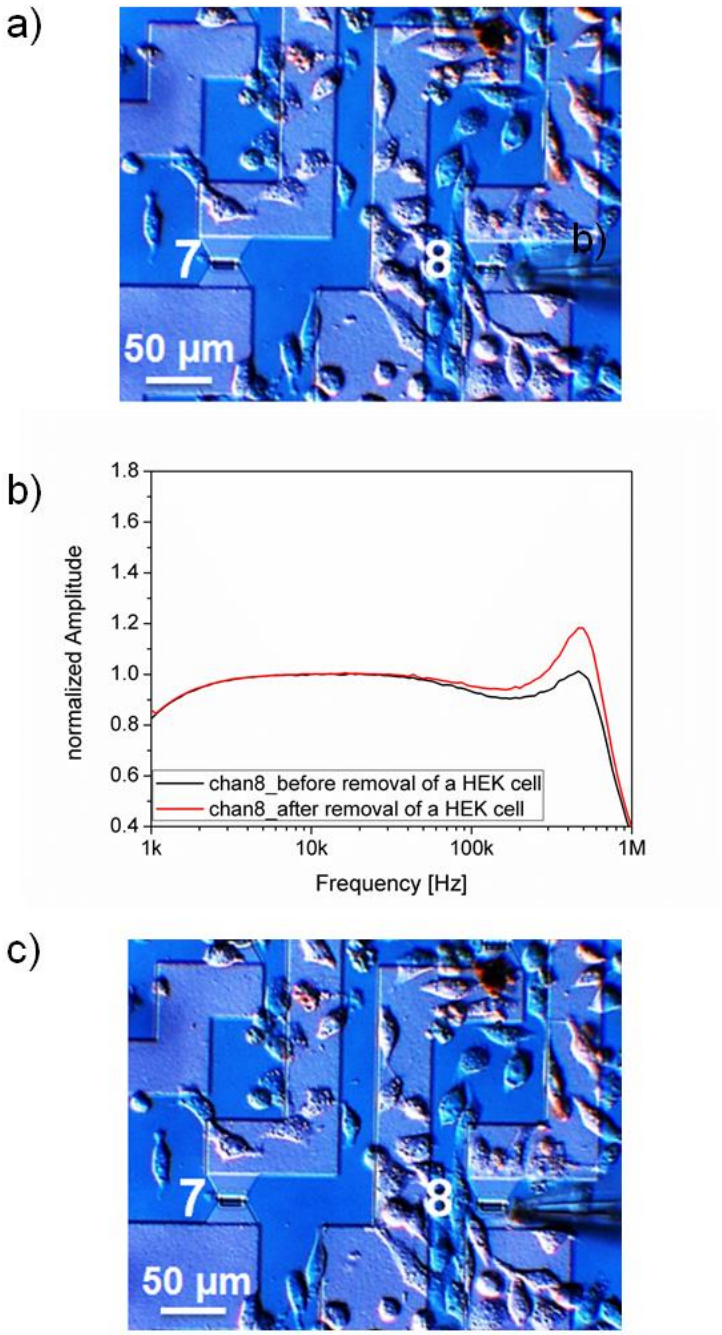

Figure 4-24 a) Microscopic image of two transistor gates of an FET device: cell-free transistor gate (number 7) and single cell-covered transistor gate (number 8). b) Comparison of the measured impedance spectra for the transistor gate 8 before and after removal of the single adhered HEK 293 cell with a patch-clamp pipette. c) Microscopic image after removal of the HEK 293 cell from the transistor gate 8 with a patch-clamp pipette. This image was adapted from (Susloparova et al., 2015).

Similar experiments were performed with the FET devices covered by single H441 cells (Figure 4-25). It can clearly be seen that the spectral changes vary from experiment to experiment and from cell type to cell type.

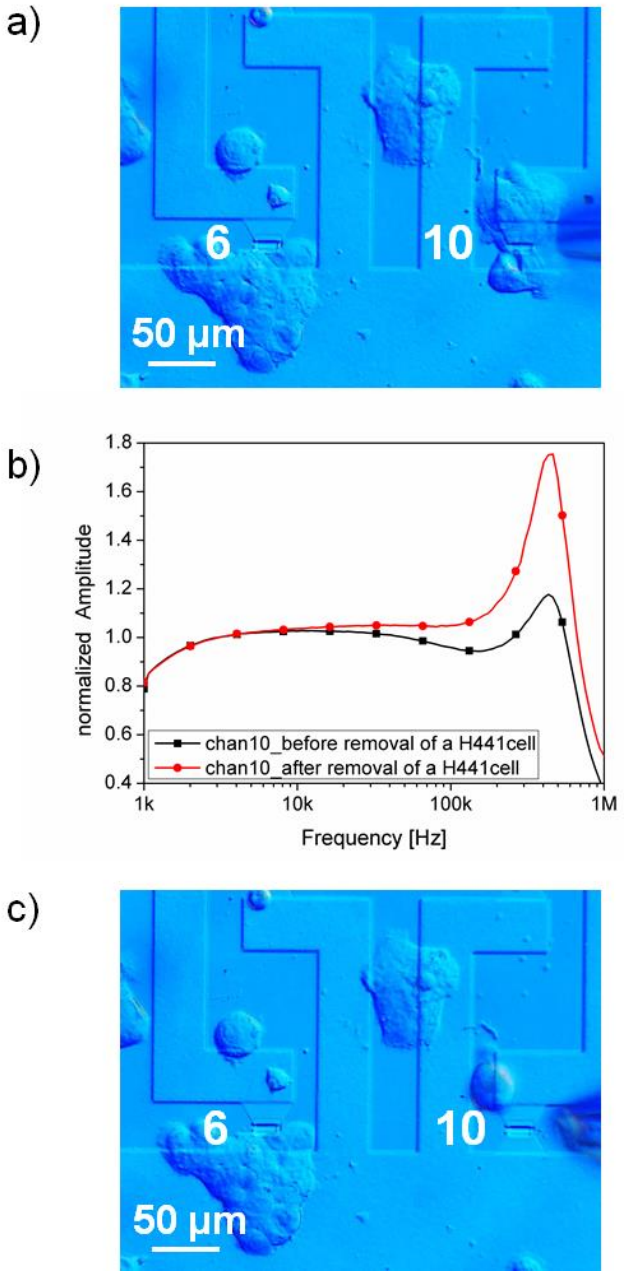

Figure 4-25 a) Microscopic image of two transistor gates of an FET device. Transistor gate 10 is covered by single H441 cell while transistor gate 6 is cell-free. b) Comparison of the measured impedance spectra for the transistor gate 10 before and after removal of the single adhered cell with a patch-clamp pipette. c) Microscopic image after removal of the H441 cell from the transistor gate 10 with a patch-clamp pipette.

4.7 Chemical removal of cells from the transistor gate surface

In contrast to the more basic experiment described in the last paragraph, the observation of chemical influences to cells attached to our devices is closer to real application in biochemical and biomedical sensing with this novel technique. In these experiments we moved from the very crude enzymatic digestion of cells by trypsin towards the application of anticancer drug known from chemotherapy in oncology pathients. In another PhD thesis work in our group (Koppenhöfer, 2016) more relevant biomedical assays were performed, while the physical foundations of this novel technique were elaborated in this thesis.

In section 4.3, the influence of the cell-related parameters on the impedance spectra was theoretically discussed by simulations. In this section (the content of this section is based on a publication (Susloparova et al., 2015)), gradual changes in the measured impedance spectra, which reflect gradual modifications in the adhesion status of the cell, will be explained by taking the example of the chemically-induced detachment process of single cells into account.

In first very basic experiment, the HEK293 cells cultured in a low density on the FET device surfaces were treated with 5 µg/ml trypsin solution. This leads to an enzymatic digestion of the extracellular matrix and to a detachment of the cells from the device. The impedance spectra were recorded stepwise one after another within 5 min of the cellular detachment process with the TTF amplifier system. In Figure 4-26 the obvious changes observed in the shape of the impedance spectra are presented for one particular experiment.

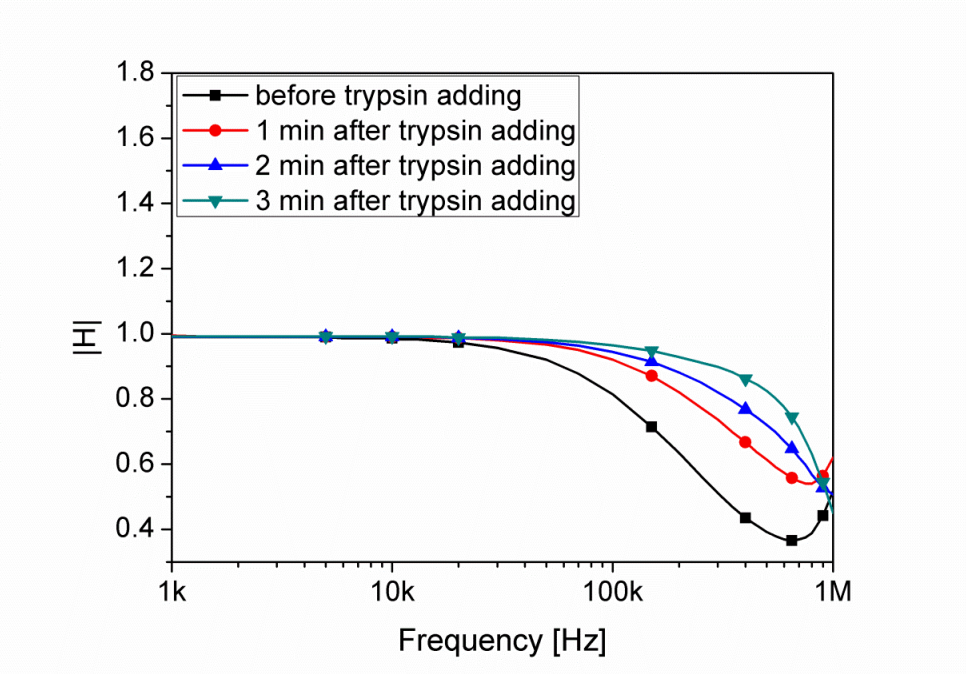

Figure 4-26 The impedance spectra for a cell-covered transistor gate of an FET device before and after adding of 5 µg/ml trypsin solution measured with the TTF amplifier system. Clear changes in the spectra can be seen during cellular detachment.

The spectra obtained during the detachment process were fitted incrementally using equation (4.17) (Figure 4-27). The fitted values of the seal resistance R_{seal} and the cell membrane capacitance C_M for this experiment are presented in Table 4-13.

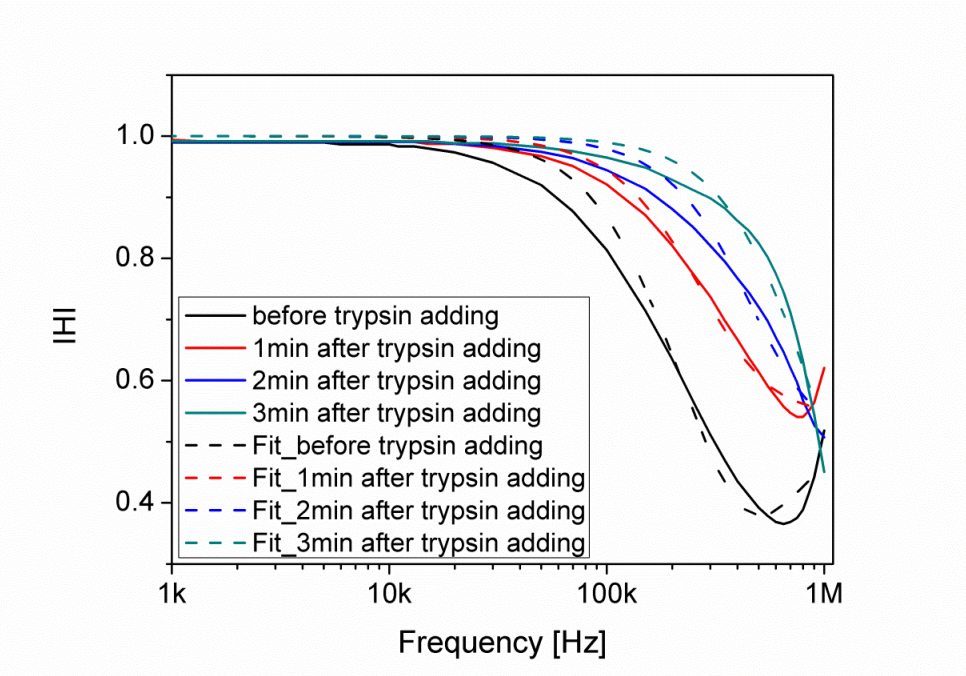

Figure 4-27 The impedance spectra measured with the TTF amplifier system during the detachment process induced by 5 µg/ml trypsin solution (solid lines) and corresponding spectra fitted by the analytical procedure described in paragraph 4.2 are shown. The corresponding seal resistance and the cell membrane capacitance values obtained from the fits are shown in Table 4-13.

	R_{seal} [MΩ]	**C_M [pF]**
before trypsin adding	1.305 ± 0.045	0.211 ± 0.011
1 min after trypsin adding	0.539 ± 0.021	0.664 ± 0.025
2 min after trypsin adding	0.259 ± 0.011	0.623 ± 0.056
3 min after trypsin adding	0.135 ± 0.011	0.917 ± 0.073

Table 4-13 The fitted values of the cell-related parameters of seal resistance R_{seal} and the cell membrane capacitance C_M during the detachment process induced by 5 µg/ml trypsin solution in the exemplary experiment shown in Figure 4-27. Error values result from the fitting procedure.

Since this detachment process happened quite fast, in the next experiments the trypsin concentration was lowered to a value of 1 µg/ml, resulting in a slower detachment. In this case, the impedance spectra were measured with the new lock-in amplifier system however, similar behaviour in the spectra was obtained.

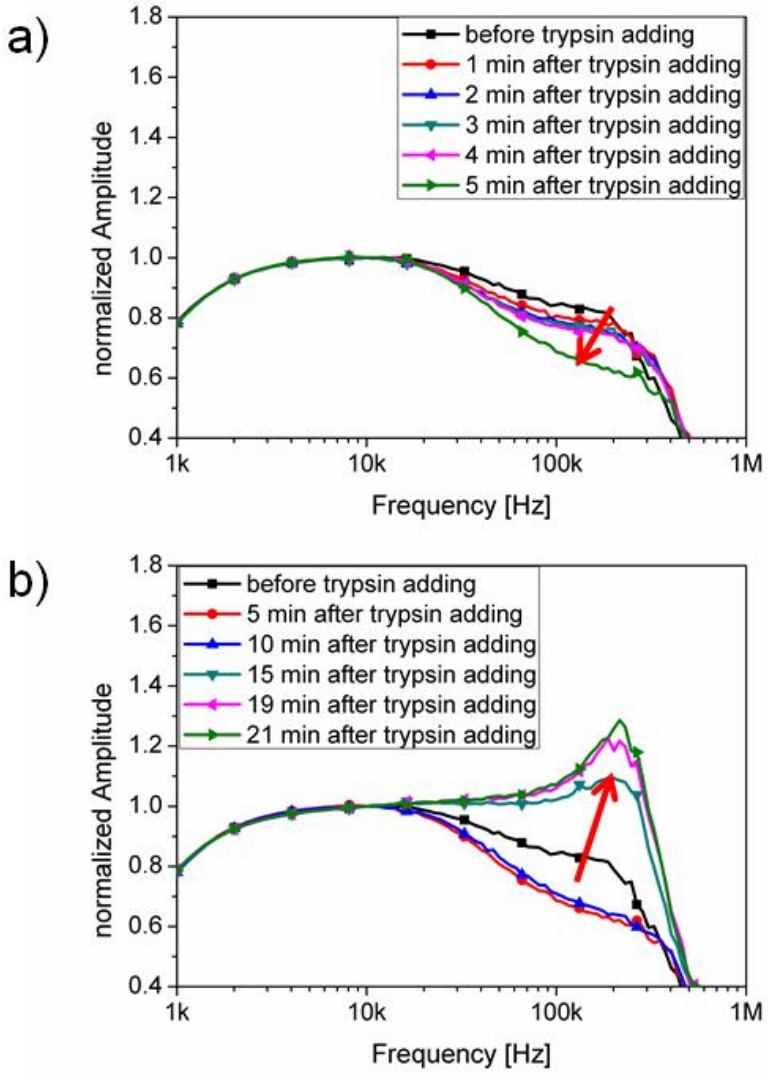

Figure 4-28 a) The impedance spectra measured with the lock-in amplifier system for a cell-covered transistor gate of an FET device after adding of 1 µg/ml trypsin solution within the first 5 minutes. A gradual decrease of the amplitude in the frequency range from 10 kHz to 400 kHz was observed. b) In the second part of the cell detachment process the measured impedance spectra showed an increase of the amplitude in the frequency range from 10 kHz to 400 kHz. An optically visible morphology change was observed only ten minutes after trypsin addition, while the electrical signals showed changes much earlier in the detachment signal.

As it can be seen in Figure 4-28, the impedance spectra were measured before and after adding of 1 µg/ml trypsin solution one after another within 21 min in this particular experiment. The cell-covered transistor gate responded very fast to the addition of the trypsin solution with gradual shape changes in the impedance spectra. After 21 min of the measurement, the typical shape of the impedance spectrum for a cell-free transistor gate was observed. For measurement and saving of each impedance spectrum with the lock-in amplifier system about 1 min was required. Within first 10 min of the measurement a gradual decrease in the transfer function amplitude in the frequency range from 10 kHz to 400 kHz was observed (Figure 4-28a). After 10 min of the measurement a gradual increase in the transfer function amplitude over time was monitored (Figure 4-28b).

The optical control showed the morphological changes of the cell from a flat to a round form, while the first changes were visibly observed after 10 min only. A combined effect of the seal resistance and the membrane capacitance to the measured shape of the impedance spectra was therefore clearly recognized in the electrical data. In Table 4-14 the fitted values of the seal resistance R_{seal} and the membrane capacitance C_M for the first five measured impedance spectra are shown. In this period a gradual decrease in transfer function amplitude (Figure 4-28a) and thus a gradual increase in the seal resistance (Table 4-14) was monitored. Afterwards a gradual increase of the amplitude (the reversing effect, which we attribute to a decrease of the seal resistance) was monitored. This effect was similar to the experiment in Figure 4-26.

	R_{seal} [MΩ]	**C_M [pF]**
1 min after trypsin adding	1.305 ± 0.081	0.155 ± 0.053
2 min after trypsin adding	1.409 ± 0.109	0.179 ± 0.043
3 min after trypsin adding	1.847 ± 0.167	0.272 ± 0.044
4 min after trypsin adding	2.162 ± 0.202	0.293 ± 0.043
5 min after trypsin adding	3.665 ± 0.278	0.228 ± 0.027

Table 4-14 The fitted values of the seal resistance R_{seal} and the cell membrane capacitance C_M during the detachment process induced by 1 µg/ml trypsin solution by fitting of the impedance spectra measured within first five minutes (Figure 4-28a).

The first experiment was performed using TTF amplifier system which is comparable to the lock-in amplifier system having no high-pass effect. Therefore, the measured impedance spectra for a cell-free transistor in Figure 4-26 and Figure 4-28 look slightly different. These two experiments discussed here represent typical recordings.

However, with the current status of our amplifier and our fitting procedure the data evaluation is quite cumbersome. In commercial systems usually time-dependent data are recorded at one particular frequency where largest changes in signal amplitude are observed.

4.8 Time-dependent measurements using a chemotherapeutic drug

In this section, such time-dependent experiments, which monitor the apoptosis event induced by a chemotherapeutic drug, are presented. For these experiments H441 cells were cultured on the FET devices in a low density and were then treated with the anticancer drug topotecan hydrochloride (10 μg/ml). Time-dependent measurements were performed using two different measurement setups, namely the TTF amplifier system (the discussed experiments are shown in a publication (Susloparova et al., 2013)) and the amplifier system with a lock-in amplifier (this data is based on a publication (Susloparova et al., 2015)). Since the cellular responses were investigated over longer periods, all experiments were carried out inside an incubator at 37°C and 5% CO_2.

4.8.1 Time-dependent measurement using TTF amplifier system

As it was already mentioned in section 3.7.1, with the TTF amplifier system is possible to record the time-dependent data by selection of only one fixed frequency for all 16 channels of an FET device, simultaneously. Therefore, one constant frequency, at which the strongest changes in the amplitude signal were expected, was selected and time-dependent measurements were performed. In Figure 4-29c for reasons of simplification, only 4 from 16 transistor gates of an FET device covered by H441 cell are presented. As it can be seen from this figure, transistor gates number 9, number 10, and number 13 are cell-covered, whereas the transistor

gate number 14 is cell-free. Figure 4-29a represents an exemplary, time-dependent measurement of the transfer functions at a constant frequency of 200 kHz for these transistor gates. The measurements were performed within 2 hours and 30 min (9000 sec). The cell-covered transistor gates (except the broken transistor gate number 9) responded with a change in the impedance spectra to the effect of the chemotherapeutic drug. The amplitude of the transfer functions for cell-covered transistor gates was increased, whereas the amplitude of the transfer function for cell-free transistor gate stayed constant. In Figure 4-29b the recorded impedance spectra before and after the administration of topotecan hydrochloride are compared. Figure 4-29d shows the morphological changes, induced when the drug containing solution was added to the cells.

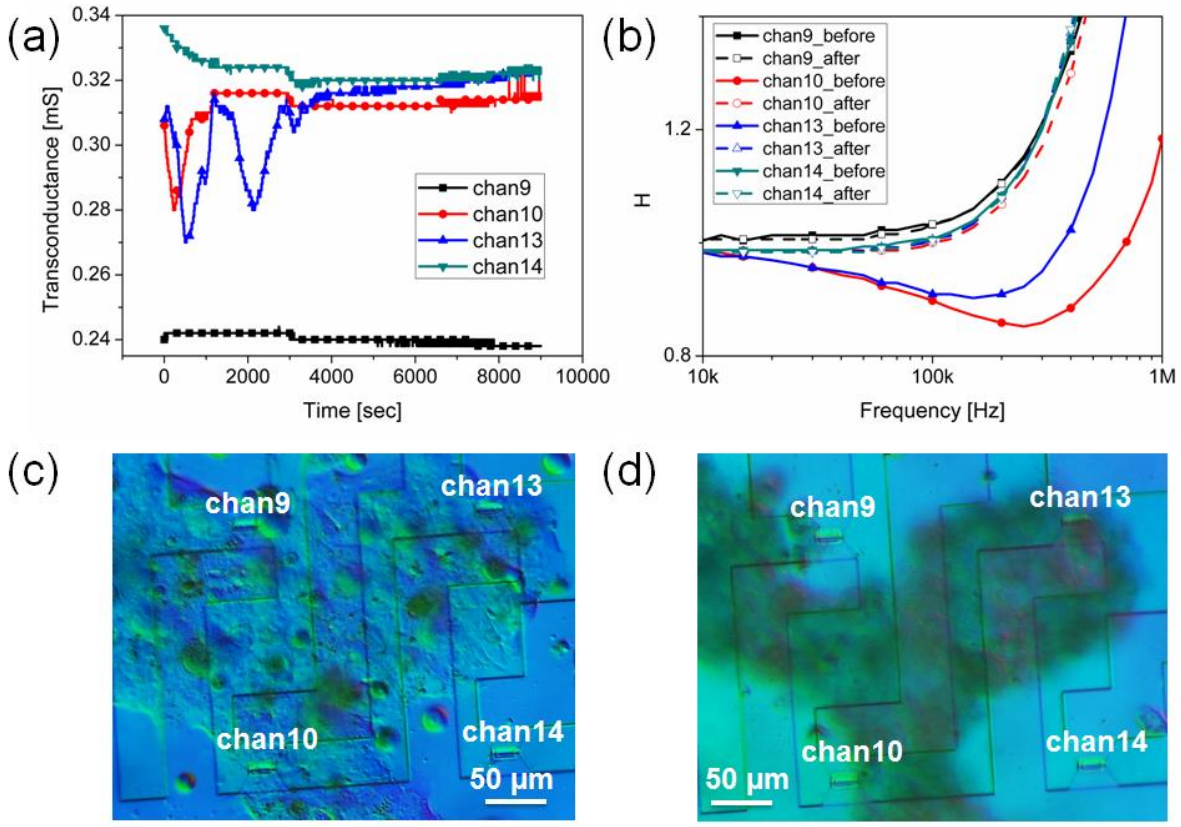

Figure 4-29 a) Time-dependent measurement performed with the TTF amplifier system at only one particular frequency of 200 kHz of four transistor gates of an FET device covered by H441 cells. b) Recorded impedance spectra before and after the administration of topotecan hydrochloride. Microscopic image of the transistor gates covered by H441 cells c) before and d) after drug administration. This image was adapted from (Susloparova et al., 2013).

4.8.2 Time-dependent measurement using lock-in amplifier system

In this section, the apoptosis event induced by the chemotherapeutic drug was investigated by time-dependent measurements performed with the second system using the fast lock-in amplifier. As it was already described in subsection 3.7.2, with this lock-in amplifier system it is possible to achieve the time-dependent recordings at several different frequencies, simultaneously. However, in this setup all 16 transistors of an FETdevice needed to be measured consecutively.

The H441 cells were cultured on the FET devices in a low density and then treated with the chemotherapeutic drug topotecan hydrochloride (10 µg/ml). First, in order to ascertain when the chemotherapeutic drug begins to affect the H441 cells, the time-dependent measurements were performed at one selected frequency within 49 hours. Figure 4-30 shows an exemplary experiment. Time-dependent recordings were carried out for a cell-covered transistor gate of an FET device at a frequency of 200 kHz. As it can be seen, the H441 cell was gradually damaged by the drug. The chemotherapeutic drug causes an increase of the amplitude value and thus the changes in the impedance spectra.

In order to confirm, that the changes were exclusively caused by the chemotherapeutic drug, for the next experiment two transistor gates of an FET device, a cell-free transistor gate and a cell-covered transistor gate were selected. The measurements for two different transistor gates of an FET device were carried out using two different analogue inputs of the lock-in amplifier. In Figure 4-31 one exemplary time-dependent measurement for two transistor gates at a selected frequency of 100 kHz is presented. As it can be seen, for the cell-free transistor gate no changes in amplitude were measured. In this experiment, the time-dependent signals were recorded for 6 hours starting 20 hours after drug administration. After 2 hours of the time-dependent recordings no changes in signal amplitude were monitored. However, similar to what was reported before for the ECIS devices a low frequency modulation is visible, which was reported before to be causal by micromotions of cells. After cell detachment only a silent signal with a slight upward drift is visible.

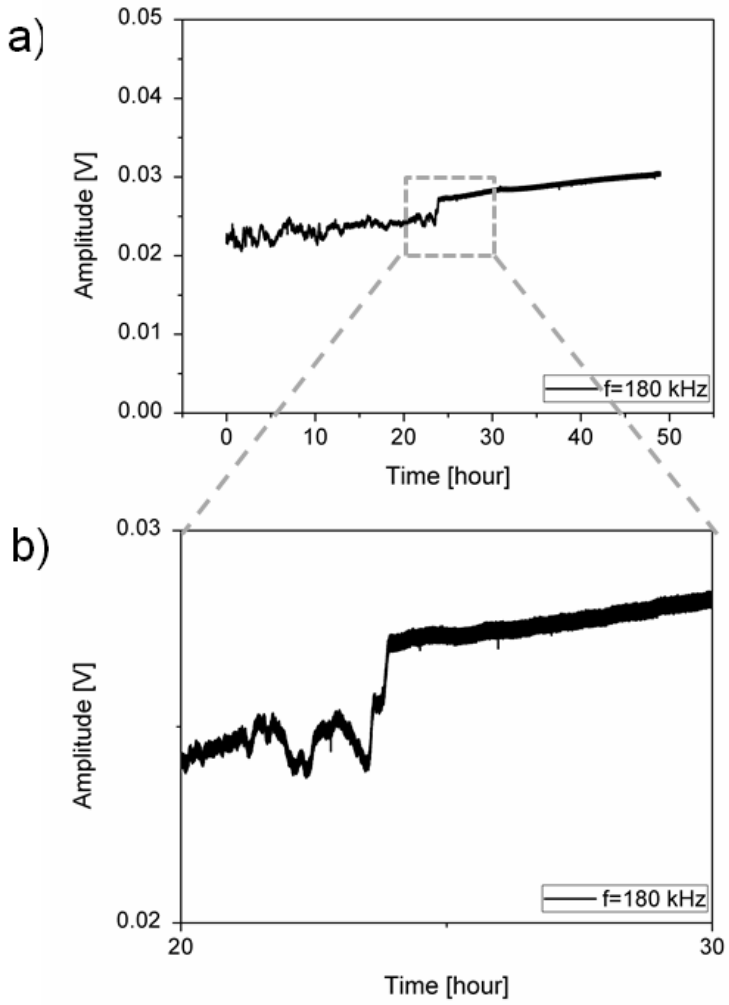

Figure 4-30 Time-dependent measurement performed with the lock-in amplifier system at frequency of 200 kHz within 49 hours for a cell-covered transistor gate of an FET device after treatment with the chemotherapeutic drug topotecan hydrochloride (10 µg/ml). After 24 hours the micromotion signal vanishes and the sensor shows no response, which we regarded as complete cell detachment.

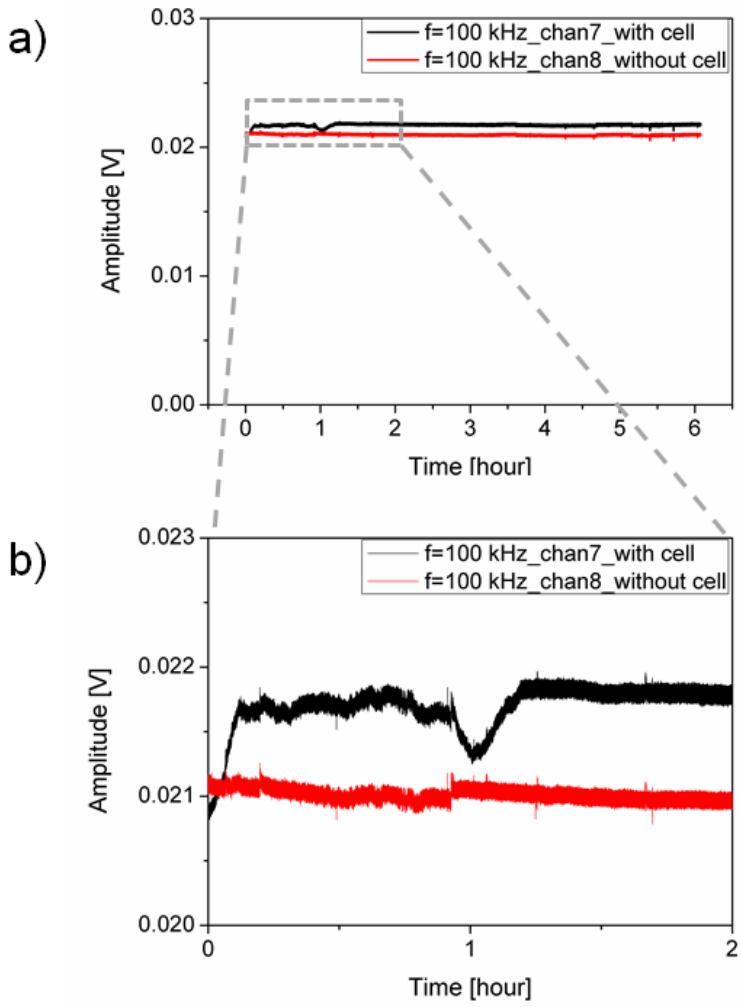

Figure 4-31 Time-dependent measurement performed with the lock-in amplifier system at frequency of 100 kHz within 6 hours for a cell-covered and a cell-free transistor gate as control channel. The data sampling was started 20 hours after drug administration.

The next experiments were carried out to monitor the effect of topotecan hydrochloride (10 µg/ml) on the H441 cells at two different frequencies, simultaneously. Two transistor gates of an FET device, a cell-free transistor gate (transistor gate 8 (Figure 4-32a)), and a cell-covered transistor gate (transistor gate 7 (Figure 4-32a)) were selected. When comparing the measured impedance spectra for a cell-free transistor gate and for a cell-covered transistor gate, it is quite evident that the largest differences can be recorded in a frequency range from 30 kHz to 600 kHz. Two different frequencies in this range (100 kHz and 300 kHz) were selected for this experiment. The recordings were performed 20 hours after drug administration as well. In Figure 4-32c the measured amplitudes over time at these two frequencies are compared. After

2 hours the cells were completely detached from the sensor surface. When comparing the measured curves at 100 kHz and 300 kHz it can be seen that the time evoluations are quite similar. First, an increase of the amplitudes of the impedance spectra over time was monitored. After one hour the amplitude was dropping, which was more pronounced at the trace of 300 kHz compared to 100 kHz. Afterwards, an increase of the amplitudes of the impedance spectra was observed again.

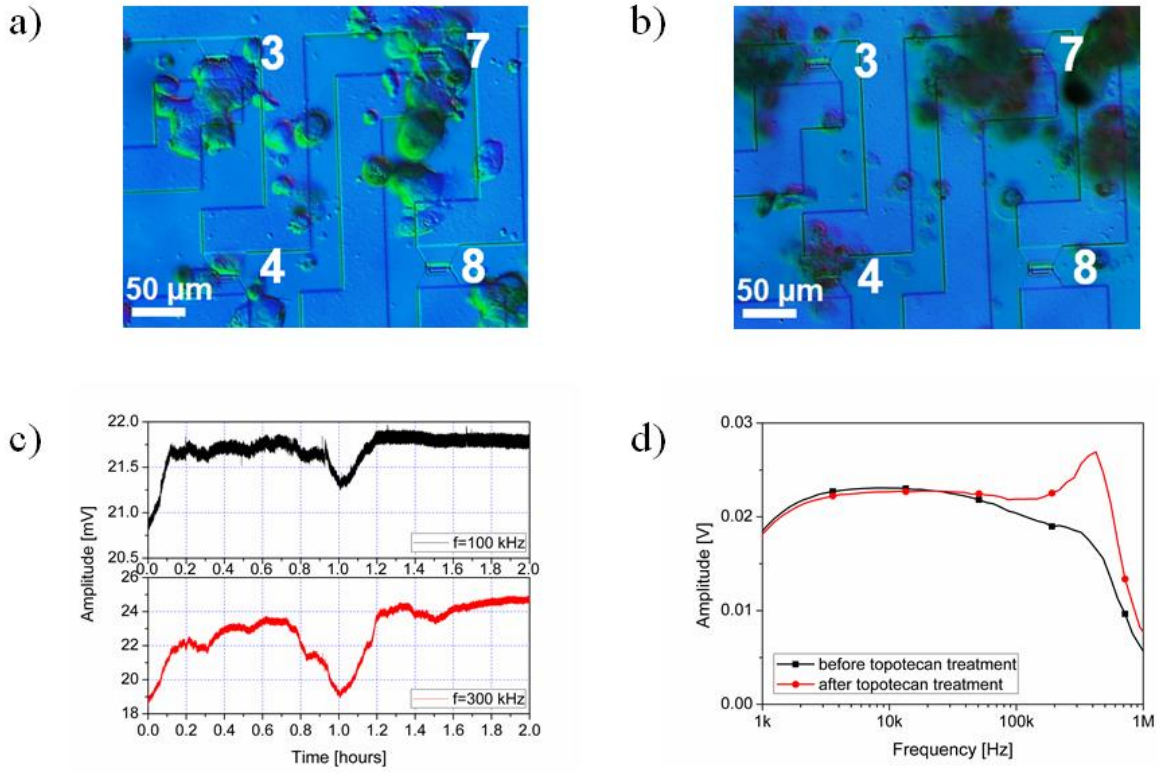

Figure 4-32 (a) Microscopic image of 4 from 16 transistor gates of an FET device covered by H441 cells. Gate 7 is cell-covered, while gates 3 and 4 are partially covered and gate 8 is cell-free. (b) The morphological changes induced after 24 hours of topotecan treatment. (c) Time-dependent measurement performed with the lock-in amplifier system at two different frequencies (at 100 kHz and at 300 kHz), simultaneously for cell-covered transistor gate (gate 7) (d) Comparison of the measured impedance spectra before and after 24 hours of topotecan (10µg/ml) treatment for cell-covered transistor gate (gate 7). This image was adapted from (Susloparova et al., 2015).

This experiment approved that a selection of only one frequency like it is usually done with the commercial ECIS systems might hide significant information and might lead to misinterpretation of the results.

A similar time evolution was observed by monitoring the detachment process induced by trypsin solution, where the amplitude of the transfer function was firstly decreased (Figure 4-28a) and afterwards increased again (Figure 4-28b). These measured impedance spectra (Figure 4-28) can be represented in a 3-dimensional plot (Figure 4-33).

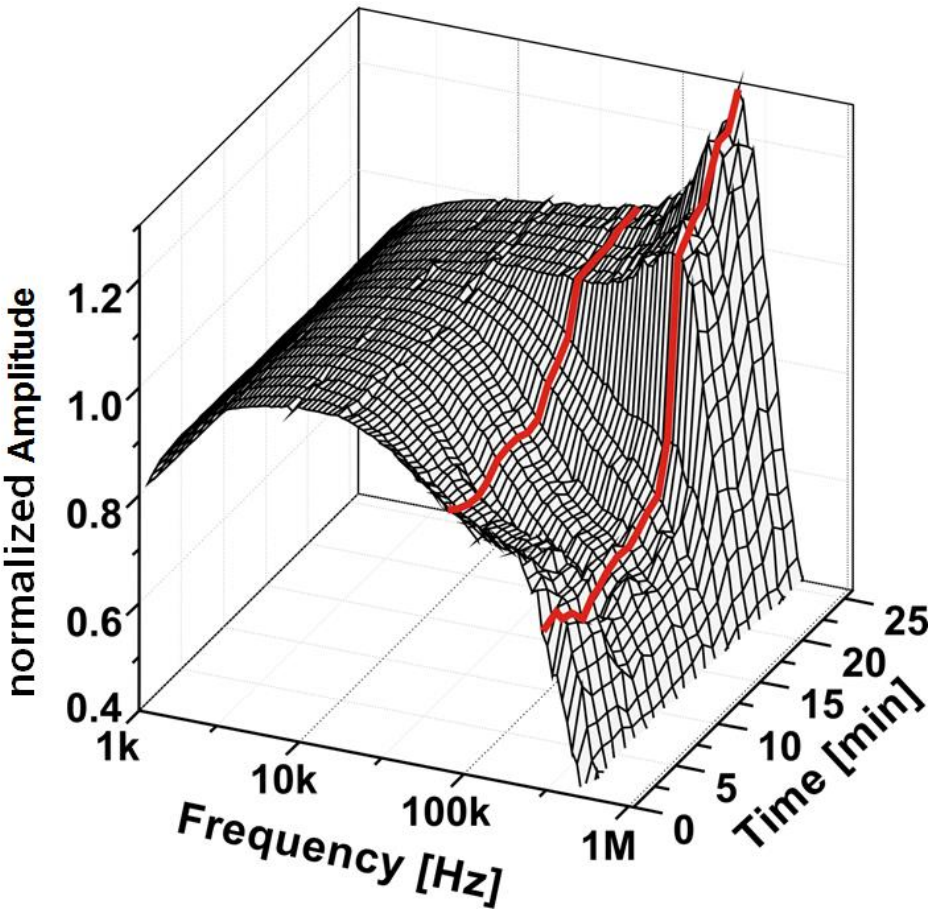

Figure 4-33 3D-representation of the time-dependent series of the impedance spectra shown in Figure 4-28. Recording at fixed frequencies is not able to reveal detailed data of the detachment processes. Such time-dependent recordings can be understood as the red lines, which are exemplary drawn into the data. The shape of these lines is quite different. Only a full recording of the respective spectra with fitting to the EEC model can reveal the shape of the 3D landscape and can be used to fully interpret the cell-related parameters during cellular detachment. This image was adapted from (Susloparova et al., 2015).

In similar way the ECIS data were presented earlier (Wegener et al., 2000) (Arndt et al., 2004). Exemplarily two lines were manually drawn into the 3D landscape, which should underpin the reason for the differences typically observed in time-dependent measurements.

The gradual decrease of the amplitude in the impedance spectra bears on a gradual increase of the seal resistance, whereas a gradual decrease of the seal resistance to the detaching cell-sensor connection and consequently to an increase of the transfer function amplitude.

However, in time-dependent experiments at fixed frequencies such effects are very difficult to observe. In order to pursue a detachment process of a single cell in detail, the complete recording of the impedance spectra and the gradual fitting of these spectra to the EEC model and obtaining of the cell-related parameters would be necessary.

4.9 Comparison of two generations of FET devices

In this section, two generations of the FET devices, which differ in gate dimensions, gate oxide thickness as well as in the thickness of the passivation layer for source and drain contact lines (section 3.1), will be compared with each other. In the following, the FET device characteristics as well as the cell-substrate adhesion measurements using two generations of FET devices will be presented. The results presented here are based on (Susloparova et al., 2014).

4.9.1 FET device characteristics

First, the electrical characteristics of both FET device generations were evaluated. The transfer characteristics $I_{DS}(V_{GS})$ of both FET device generations were measured in the same range of gate–source voltage V_{GS} from 0 to − 3V, while varying the drain–source voltage V_{DS} from 0 to − 3V in steps of 1 V. The transistor transconductance g_m was numerically derived from the transfer characteristics. The top graphs in Figure 4-34 and Figure 4-35 show the measured transfer characteristics, whereas the bottom graphs show the transistor transconductance. In terms of electrical performance the newer version of the FET devices has higher transconductance values. The maximum value of the transconductance for the former FET devices is

achieved at 0.45 mS (at $V_{DS} = -3$ V and $V_{GS} = -2$ V), while for the new FET devices of 0.5 mS (at $V_{DS} = -3$ V and $V_{GS} = -2.2$ V).

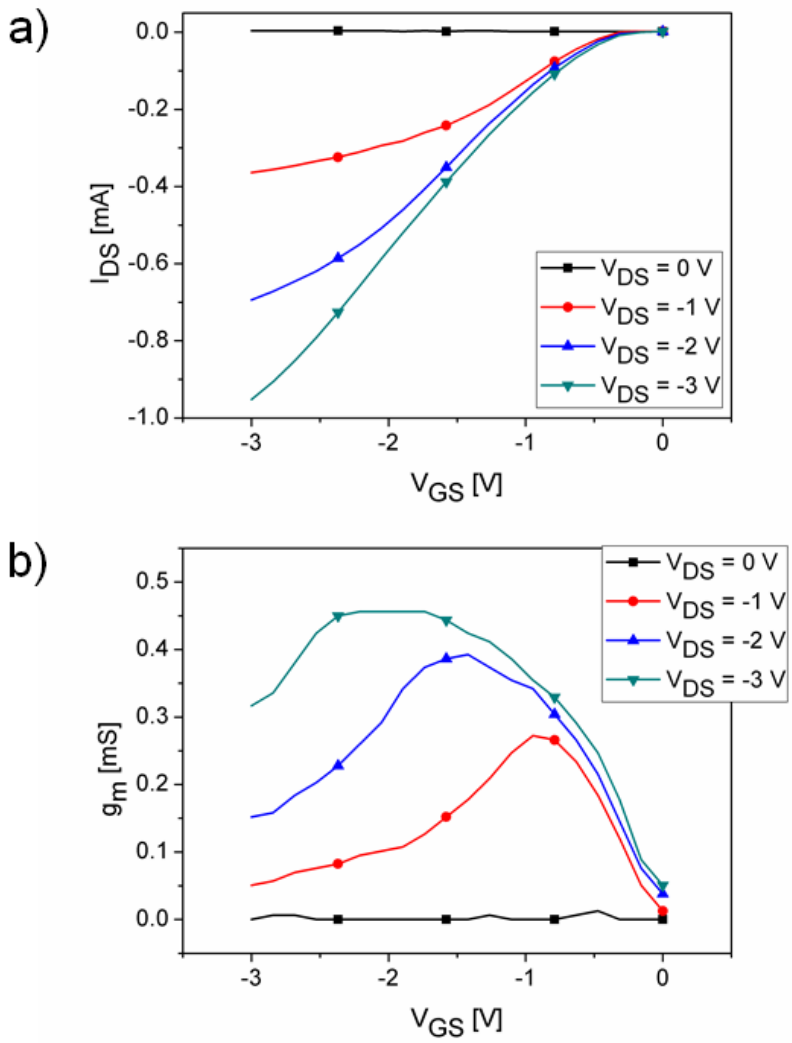

Figure 4-34 a) The transfer characteristics $I_{DS}(V_{GS})$ and (b) the transistor transconductance g_m of the previous FET device with the gate dimensions 5×16 µm^2, the gate oxide thickness of 10 nm, and the thickness of the passivation layer for source and drain contact lines of 480 nm. This image was adapted from (Susloparova et al., 2014).

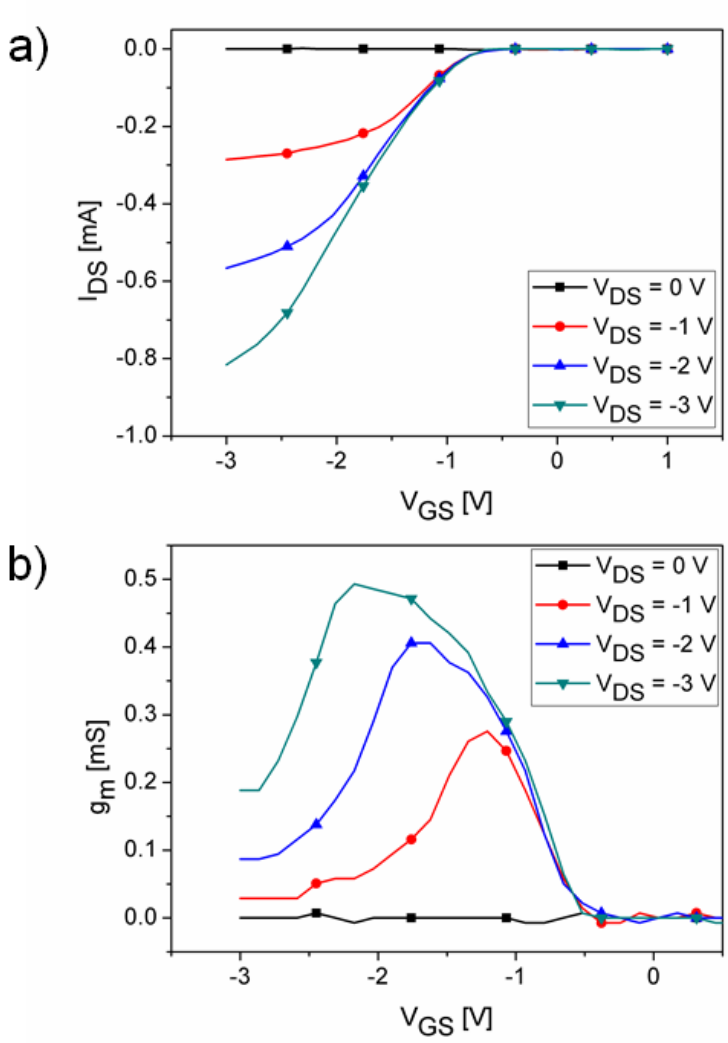

Figure 4-35 (a) The transfer characteristics $I_{DS}(V_{GS})$ and (b) the transistor transconductance g_m of the new FET device with the gate dimensions 5×25 µm^2, the gate oxide thickness of 6 nm, and the thickness of the passivation layer for source and drain contact lines of 220 nm. This image was adapted from (Susloparova et al., 2014).

4.9.2 Cell-substrate adhesion measurements

Further, cell-substrate adhesion measurements using both FET device generations were performed and compared with each other. The HEK293 cells were cultured on the both FET device generations (Figure 4-36). Considering the Figure 4-36a and Figure 4-36b is visible that in case of the previous chip design cells preferentially adhered to the edges of the contact

lines, whereas in case of the new chip design these effects were eliminated. This is due to the fact that a much shallower surface topography was obtained in the newer fabrication process.

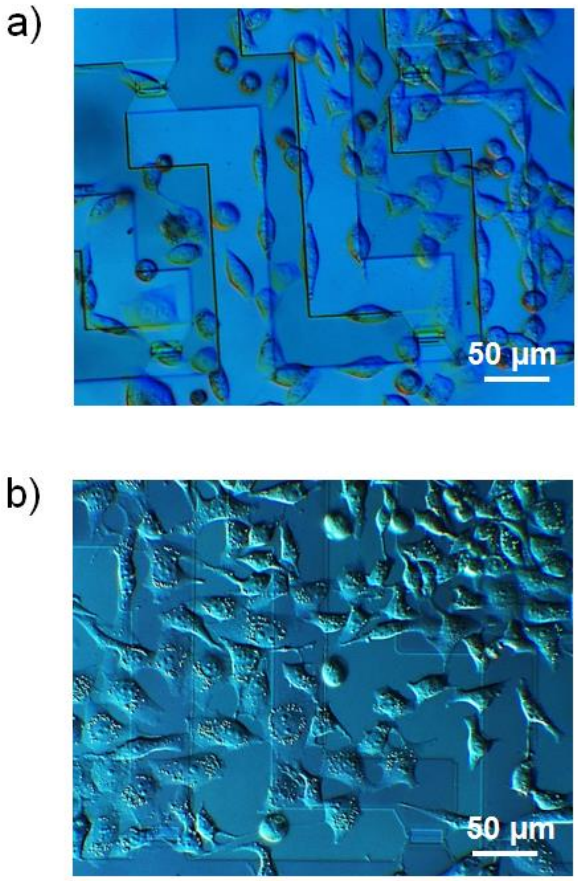

Figure 4-36 Microscopic images of the transistor gates of (a) a previous FET device and (b) a new FET device covered by HEK293 cells. In case of the previous chip design the preferentially adhesion of cells to the edges of the contact lines on the surface can be seen, whereas in the new chip design a preferentially flatter morphology of cells can be seen. This image was adapted from (Susloparova et al., 2014).

The cell-substrate adhesion measurements were performed with two different measurement setups. In Figure 4-37 the impedance spectra recorded with the TTF amplifier system for cell-free and cell-covered transistor gates of an FET device are shown. An increased difference in the impedance spectra measured for cell-covered and cell-free transistor gates in the case of the newly designed FET devices was clearly monitored. The value of the inflection point of the transfer function amounts to 0.92 for the previous FET device and 0.84 for the new FET

device, respectively. In the TTF amplifier system, usually the data recorded above 300 – 400 kHz are not really exact due to the custom-made, low cost electronics realization. In this former instrument the bandwidth of the recordings was widened by actively switching passive low pass and high pass filters, respectively.

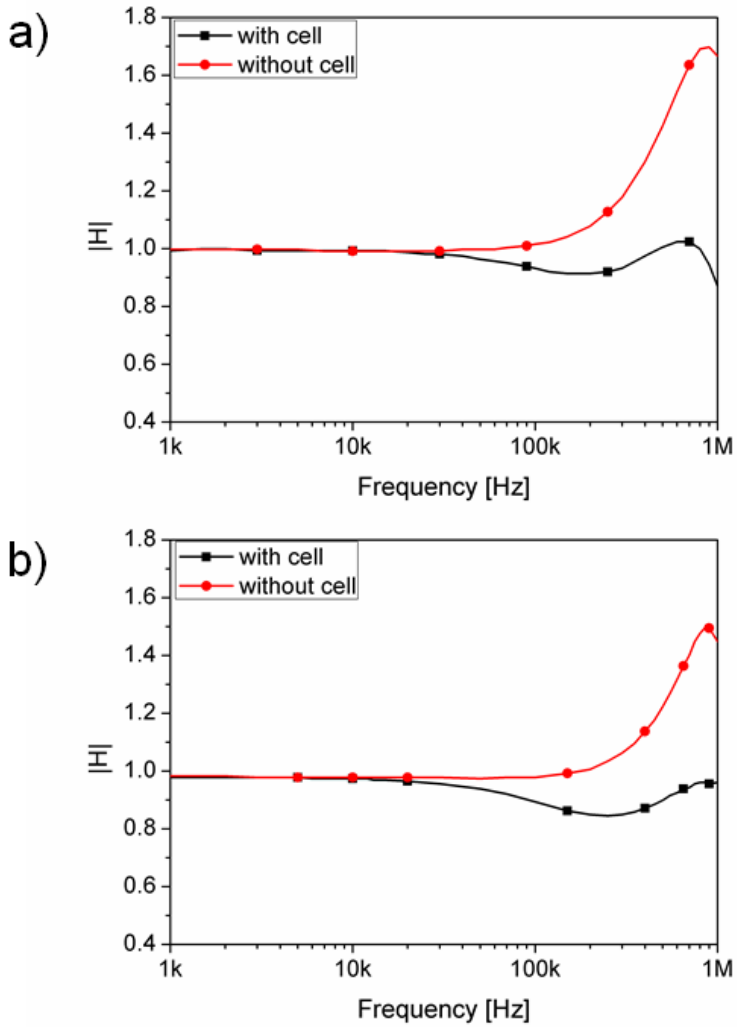

Figure 4-37 The impedance spectra measured with the TTF amplifier system using (a) former generation of the FET devices and (b) new generation of the FET devices. This image was adapted from (Susloparova et al., 2014).

This difference becomes more obvious in the exemplary measurement shown in Figure 4-38. In this case the spectra were measured with the high-frequency electronics using the fast lock-in amplifier. These spectra represent the pure impedance spectra which are not smothered by filter settings in the high frequency part where the spectral changes due to cell adhesion occur. However, at frequencies below 5 kHz a high pass filter is introduced by the lock-in amplifier.

In this measurement a clear shift of the cutoff frequency of the low pass filter effect to lower frequencies can be seen. The peak point in the impedance spectra in the cell-free cases shifted from 400 kHz in the former FET design to only 200 kHz in the new generation of the FET devices with flat topology. The difference in the measured impedance for cell-covered and cell-free transistor gates in the case of the newly designed FET devices was clearly discernible. A good correlation was found between the performed simulations (section 4.4) and the experimental data.

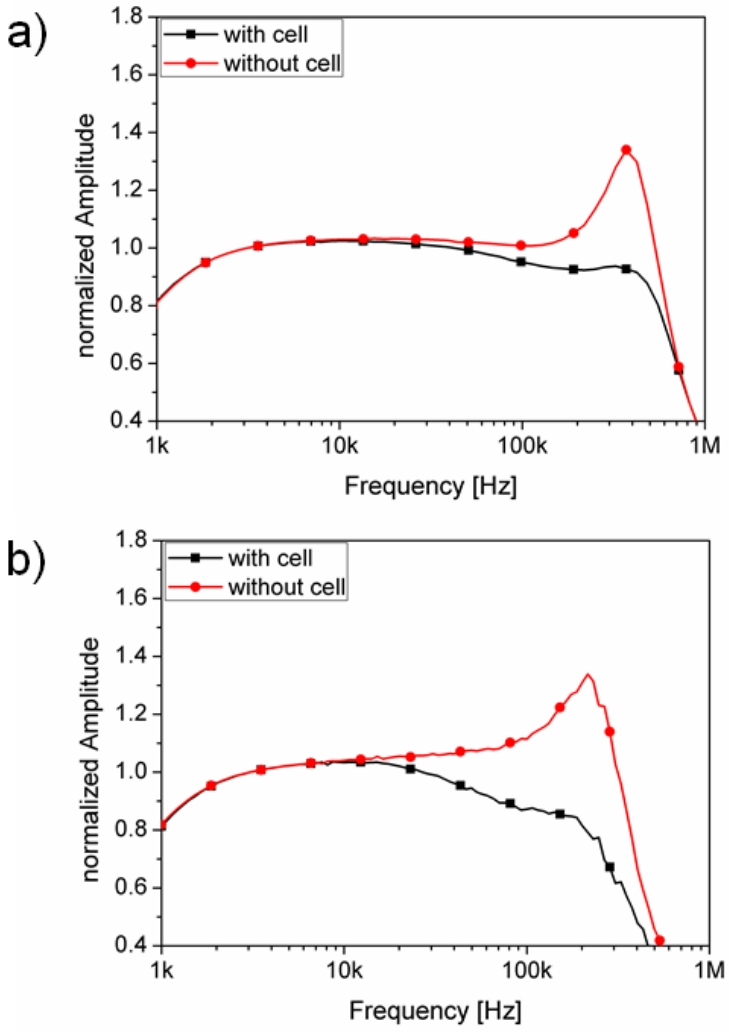

Figure 4-38 The impedance spectra measured with the lock-in amplifier system using (a) a former FET device and (b) a new FET device. This image was adapted from (Susloparova et al., 2014).

Chapter 5

5 Organic electrochemical field-effect transistor devices for cell adhesion monitoring

In this chapter, the field-effect transistor devices based on organic materials as active semiconductor component will be presented. In the end phase of this thesis these devices were tested with the optimized electronics and results were compared with the adhesion results obtained with the silicon FET devices. The development and the fabrication process, electrical characterization and first cell measurements with the OECT devices are described here (the content of this chapter is based on (Ingebrandt et al., 2015)). The OECT devices showed excellent biocompatibility. The HEK 293 cells were successfully grown on the PEDOT:PSS surface. The devices were stable enough in cell culture to use them to monitor the cell adhesion after a few days in culture.

Organic semiconductor materials have found broad application in optoelectronic devices such as organic light-emitting diodes (OLEDs), organic solar cells and organic thin-film transistors (OTFTs). OTFTs in general can be classified into organic field-effect transistors (OFETs) and organic electrochemical transistors (OECTs).

Field-effect transistor devices based on organic semiconductor materials recently have found application in the field of chemical- and biosensors. Different organic semiconductors, such as pentacene, poly(3-hexylthiophene) (P3HT), polyaniline (PANI), and poly(3,4-

ethylenedioxythiophene):poly(styrene sulfonic acid) (PEDOT:PSS) were used as the active layers in the sensors. These materials offer advantages, such as low cost, flexibility, easy fabrication and compatibility with biological systems. Several studies demonstrated that OECT devices could be used for sensing of ions (Lin et al., 2010a), pH (Loi et al., 2005) (Bartic et al., 2002), humidity (Nilsson et al., 2002), glucose (Zhu et al., 2004), antibody-antigen (Kim et al., 2010) (Kanungo et al., 2002), DNA (Krishnamoorthy et al., 2004) , and cells (Lin et al., 2010b). The OECT devices can be fabricated by spin coating, inkjet printing, and screen printing. The most common material for biological applications is PEDOT:PSS (Kergoat et al., 2012) (Nikolou and Malliaras, 2008) (Groenendaal et al., 2000).

The previously described field-effect transistor devices based on silicon were used throughout this thesis for electrical cell-substrate adhesion sensing. The main disadvantage of silicon-based transistors is the high cost of the fabrication process and the opaque devices, which interfere with standard cell culture microscopy. Polymer-based devices provide low fabrication cost and optical transparency and might be an alternative for new biosensor developments. Electrical cell-substrate impedance measurements with this device type were successfully established. They offer very promising future applications and eventual commercial impact.

5.1 First characterization steps of PEDOT:PSS

First, the electrical transport properties, the solubility and robustness in aqueous media, as well as the biocompatible features of PEDOT:PSS were examined. For this purpose PEDOT:PSS (Orgacon IJ-1005, Sigma Aldrich, Germany) was deposited by means of an inkjet printer (Dimatix Materials Printer 2800 (DMP-2800), FUJIFILM, USA) on glass substrates. At first glass samples (2.5×2.5 cm^2) were sonicated for 5 min each in acetone, isopropyl alcohol, DI water and were finally dried under nitrogen flow. Next, the glass surfaces were activated in a plasma oven at 240 W power and 40% oxygen environment for 3 minutes. Afterwards two layers of PEDOT:PSS were printed on top of glass substrates. PEDOT:PSS was inkjet printed in the center of the glass samples (pattern size of 1×1 cm^2) and then was annealed in vacuum environment at 120° C for four hours. Further the thickness as well as the uniformity of the PEDOT:PSS film was characterized by atomic force microscopy (AFM). For this purpose the printed area was scratched in the middle. The AFM measurements were carried out

in tapping mode with a scanned area of 90×90 µm^2. The AFM image of two PEDOT:PSS layers is shown in Figure 5-1. From the AFM measurement the thickness of two PEDOT:PSS layers resulted to about 130 nm.

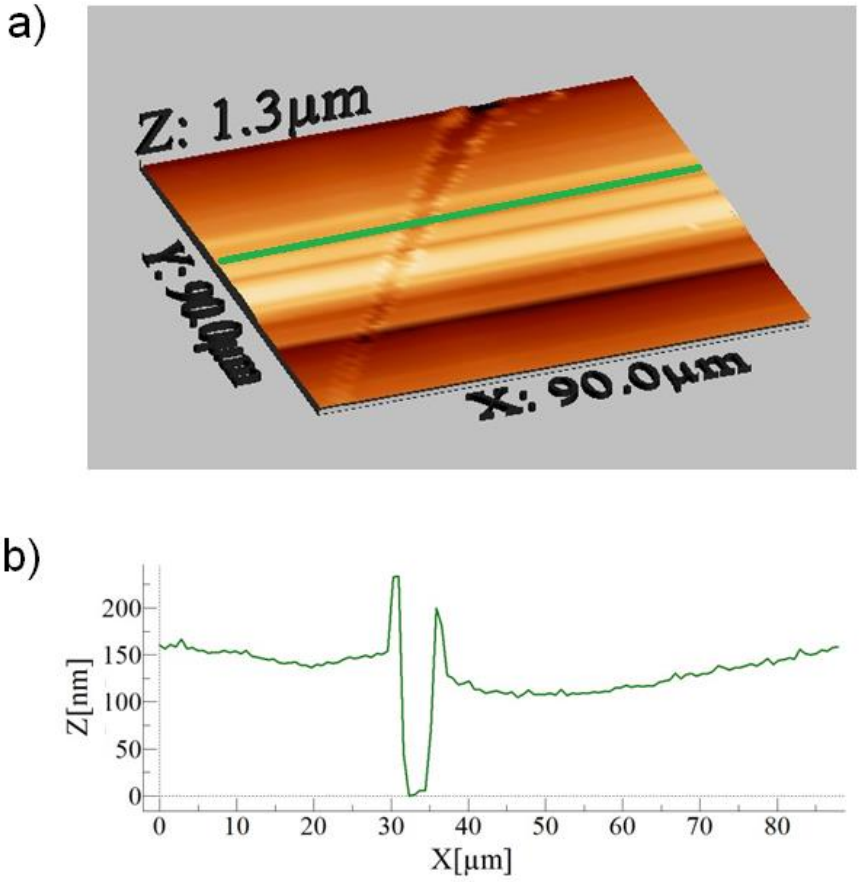

Figure 5-1 Atomic force microscopy image of two printed PEDOT:PSS layers with the thickness of about 130 nm.

Afterwards, a thin layer of ethylene glycol (EG) (Sigma Aldrich, Germany) was spin coated on top of the PEDOT:PSS film and subsequently annealed in vacuum environment at 120° C for 14 hours.

The fundamental electrical property of any semiconductor material is its electrical conductivity. Hence, at first the electrical conductivity of PEDOT:PSS was established. Conductivity σ is defined as the inverse of resistivity ρ:

$$\sigma = \frac{1}{\rho} \tag{5.1}$$

The resistivity of the PEDOT:PSS film was measured using the four-point probe method in an inline configuration. By passing a current I through two outer probes and measuring the voltage V through the inner probes allows the measurement of the substrate resistivity ρ:

$$\rho = \frac{\pi}{\ln 2}\frac{V}{I} \tag{5.2}$$

In Table 5-1 the resistivity values of the printed PEDOT:PSS film on glass substrates before and after treatment with ethylene glycol are compared. A clear increase of the conductivity of PEDOT:PSS after treatment with EG was observed. This can be explained by an improved carrier mobility of PEDOT:PSS. The carrier mobility of PEDOT:PSS after treatment with EG was reported to increase from 0.15 $cm^2/V\,s$ to 3.6 $cm^2/V\,s$ (Yamashita et al., 2011).

samples no.	**before treatment with EG ρ [MΩ·cm]**	**after treatment with EG ρ [kΩ·cm]**
1	223.74	23.69
2	249.23	23.32
3	361.9	26.49

Table 5-1 The resistivity values ρ of the PEDOT:PSS film measured using a four-point probe method before and after treatment with ethylene glycol (EG).

Changes in the surface properties of the PEDOT:PSS film after treatment with EG were tested by contact angle measurements (OCA 15Plus, DataPhysics, Germany). The water contact angle of a PEDOT:PSS film amounts to 8−12°, while a PEDOT:PSS film treated with ethylene glycol is 45-50° (Figure 5-2). This indicates that the surface of the PEDOT:PSS film becomes more hydrophobic after treatment with EG.

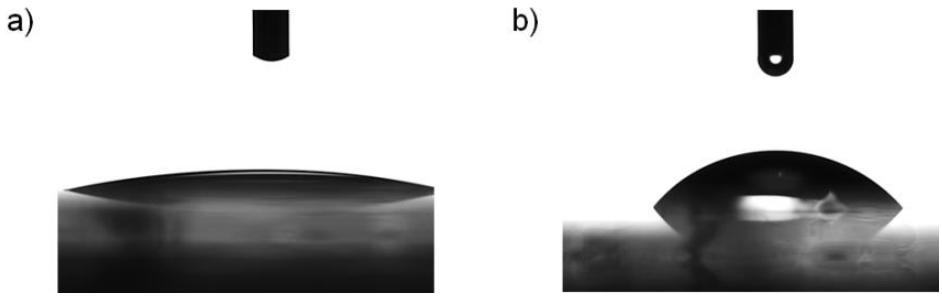

Figure 5-2 A water drop a) on a PEDOT:PSS film showed contact angle of 8-12° and b) on a PEDOT:PSS film treated with ethylene glycol of 45-50°.

In order to investigate the stability of the conductivity values of the PEDOT:PSS film treated with EG, the samples (two layers of PEDOT:PSS printed on glass substrates and treated with EG) were immersed in M10 medium and their resistivity was measured after 24 hours and 48 hours of incubation with M10 medium (Table 5-2). As it can be seen from the measured resistivity values, the electrical conductivity of the PEDOT:PSS film treated with EG was decreased by 10 times after 48 hours of incubation with M10 medium. Although this is a quite large change the devices will still function after longer incubation periods and could at least be used for acute cell adhesion and detachment experiments.

sample no.	**before ρ [kΩ cm]**	**after 24 h in M10 medium ρ [kΩ cm]**	**after 48 h in M10 medium ρ [kΩ cm]**
1	28.13	122.01	304.94
2	23.32	149.87	483.98

Table 5-2 The resistivity values ρ of the samples (two layers of PEDOT:PSS printed on glass substrates) measured using a four-point probe method before incubation of the samples in M10 medium and after 24 hours and 48 hours of incubation.

After it was demonstrated that the PEDOT:PSS film treated with EG is conductive and sufficiently stable in cell medium, the electrochemical gating behavior of PEDOT:PSS was investigated. PEDOT:PSS was printed on the glass substrates in the form of lines with a lenght of 1

cm and a width of 100 µm. The ends of the lines were coated with silver glue, which acted as source and drain electrodes (Figure 5-3).

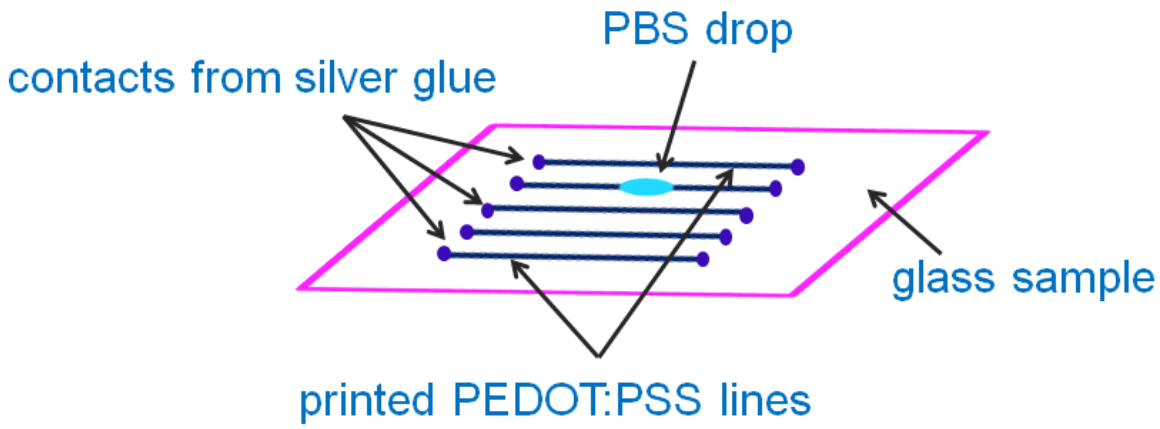

Figure 5-3 PEDOT:PSS was printed on a glass sample in form of lines with length of 1 cm and width of 100 µm.

The transfer characteristics and the leakage current of PEDOT:PSS line were measured at a wafer probe station. Two thin needles were positioned on source and drain electrodes and the third needle (Ag/AgCl wire) was immersed into a droplet of Phosphate Buffered Saline (PBS) solution, which was dropped on a PEDOS:PSS line. The gate-source voltage V_{GS} was varied from 0.5 V to − 0.5 V in steps of − 0.1 V, the drain-source voltage V_{DS} was varied from 0 V to − 0.3 V in steps of − 0.1 V, and the drain–source current $I_{DS}(V_{GS})$ and the leakage current $I_{GS}(V_{GS})$ were measured (Figure 5-4). As it can be seen, the fabricated device behaved in a typical manner of a field-effect transistor. However, the drain-source current lies in the range of µA, that leads to the transconductance value g_m in the range of µS for these very crude PEDOT:PSS lines.

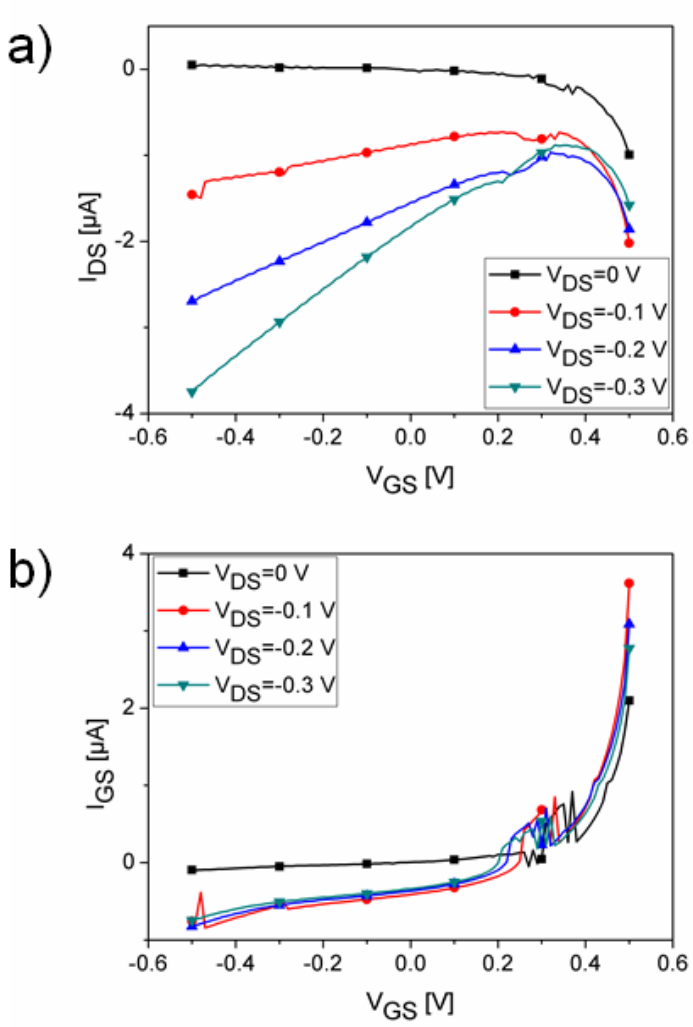

Figure 5-4 a) The transfer characteristics $I_{DS}(V_{GS})$ and b) the leakage current $I_{GS}(V_{GS})$ through the gate electrode measured at a wafer probe station for an PEDOT:PSS line with the dimensions 100 µm×1 cm.

5.2 Electrical characterization of the OECT devices

After the very general material optimization and characterization, real OECT devices were fabricated using the gold electrode array designs with single and multiple interdigitated source and drain electrodes as described in section 3.4. In the following, the electrical characterization of these devices is discussed.

Before encapsulation for cell experiments, the produced OECT devices were characterized at a wafer probe station as well. Source and drain electrodes were contacted by two thin needles,

while the gate was contacted via Ag/AgCl wire, which was immersed into a droplet of PBS on the transistor surface. The gate-source voltage V_{GS} was varied from 0.5 V to − 0.5 V in steps of − 0.1 V, the drain-source voltage V_{DS} was varied from 0 V to − 0.3 V in steps of − 0.1 V, and the drain–source current $I_{DS}(V_{GS})$ and the leakage current $I_{GS}(V_{GS})$ were measured, respectively. From this data, the transconductance g_m was calculated by derivation of $I_{DS}(V_{GS})$. The measured characteristics are presented in the following Figures: Figure 5-5 (an OECT device with the gate dimensions 100×10 μm^2 and single interdigitated source and drain electrode), Figure 5-6 (an OECT device with the gate dimensions 100×100 μm^2 and 4 interdigitated source and drain electrodes), and Figure 5-7 (an OECT device with the gate dimensions 200×200 μm^2 and 8 interdigitated source and drain electrodes).

The performance of the devices was compared with respect to the leakage current $I_{GS}(V_{GS})$ through the gate, which forms a limiting factor by signal creation and should be kept as small as possible. Compared to the drain-source current $I_{DS}(V_{GS})$ the leakage current $I_{GS}(V_{GS})$ is small and was measured in microamperes.

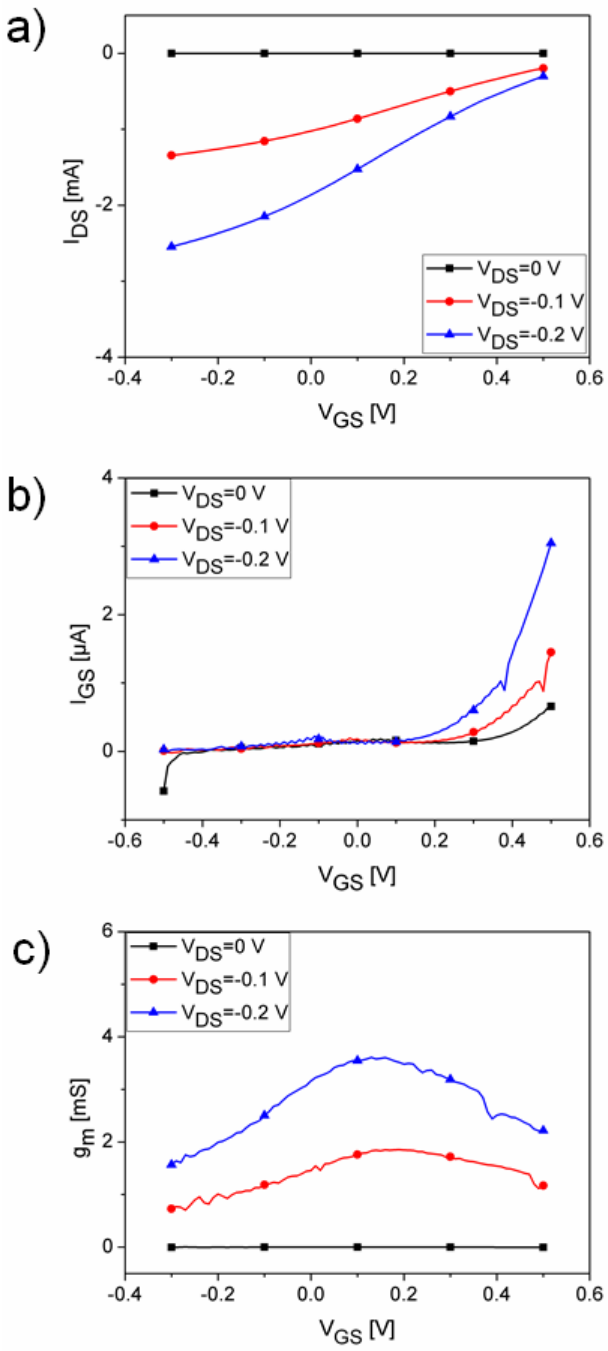

Figure 5-5 a) The transfer characteristics $I_{DS}(V_{GS})$ b) the leakage current $I_{GS}(V_{GS})$ and c) the transistor transconductance g_m of an OECT device with the gate dimensions 100×10 µm^2 (single interdigitated source and drain electrode) measured at a wafer probe station.

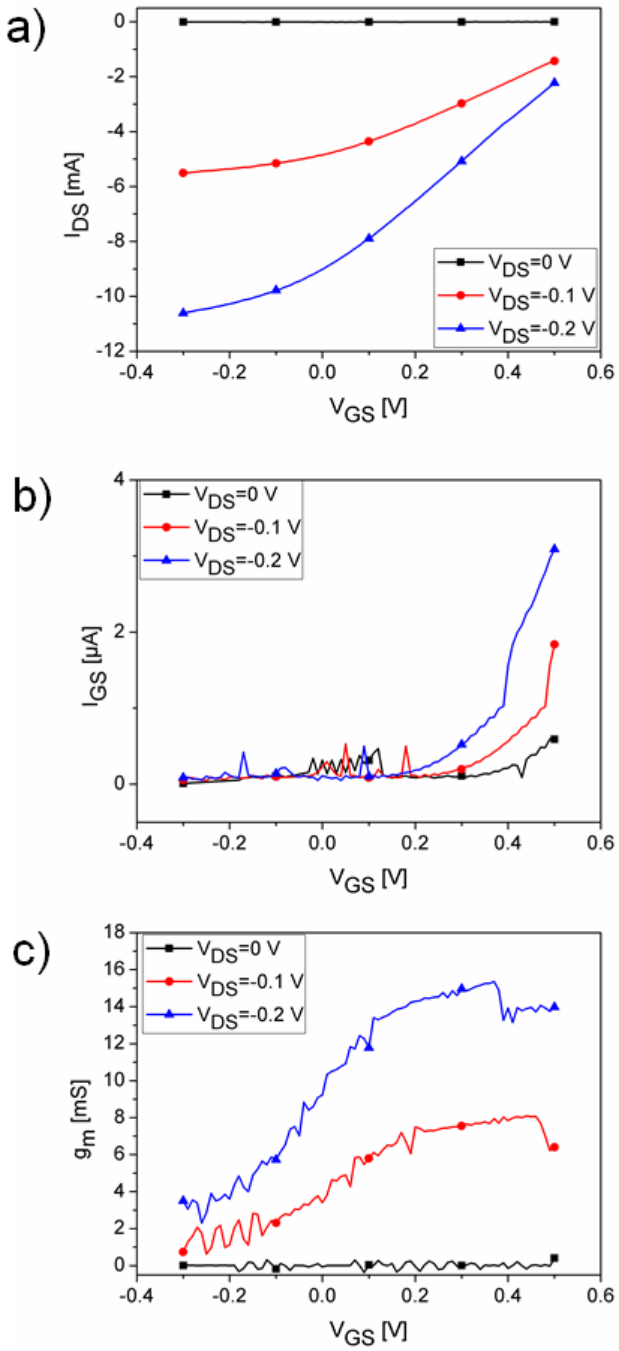

Figure 5-6 a) The transfer characteristics $I_{DS}(V_{GS})$ b) the leakage current $I_{GS}(V_{GS})$ and c) the transistor transconductance g_m of an OECT device with the gate dimensions 100×100 µm^2 (4 interdigitated source and drain electrodes) measured at a wafer probe station.

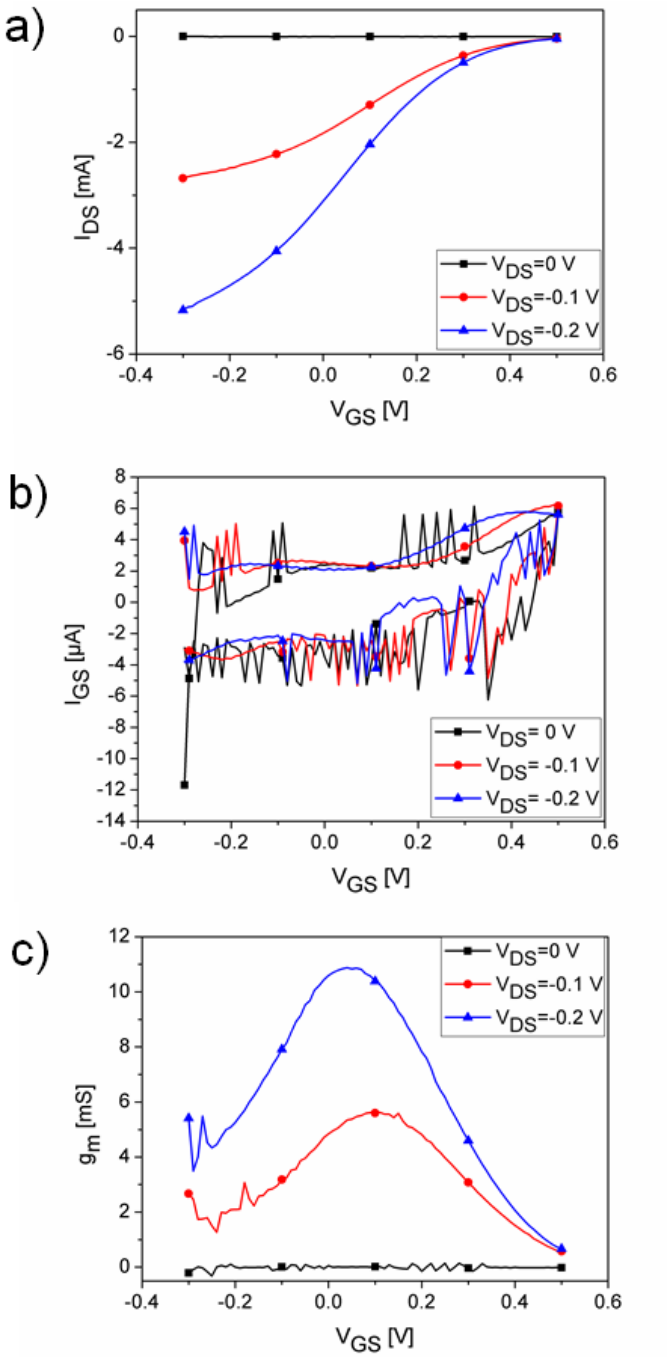

Figure 5-7 a) The transfer characteristics $I_{DS}(V_{GS})$ b) the leakage current $I_{GS}(V_{GS})$ and c) the transistor transconductance g_m of an OECT device with the gate dimensions 200×200 µm^2 (8 interdigitated source and drain electrodes) measured at a wafer probe station.

It can be seen from the graphs that with the multiple finger designs very large transconductance values compared to the silicon FET devices can be obtained. Another very nice effect is

that the OECT devices can be regarded as depletion mode types having highest transconductance values at zero gate voltage bios making then very suitable for biological experiments.

Afterwards the OECT devices were encapsulated and the electrical characteristics were measured with the TTF amplifier system. The gate-source voltage V_{GS} was varied from 0.8 V to − 0.4 V in steps of − 0.1 V, the drain-source voltage V_{DS} was varied from 0 V to − 0.3 V in steps of − 0.1 V, and the drain-source current $I_{DS}(V_{GS})$ was measured. From this data, the transconductance g_m was calculated by derivation of $I_{DS}(V_{GS})$. The measured characteristics are presented in the following Figures: Figure 5-8 (an OECT device with the gate dimensions 100×10 μm^2 and single interdigitated source and drain electrode), Figure 5-9 (an OECT device with the gate dimensions 100×100 μm^2 and 4 interdigitated source and drain electrodes), and Figure 5-10 (an OECT device with the gate dimensions 200×200 μm^2 and 8 interdigitated source and drain electrodes).

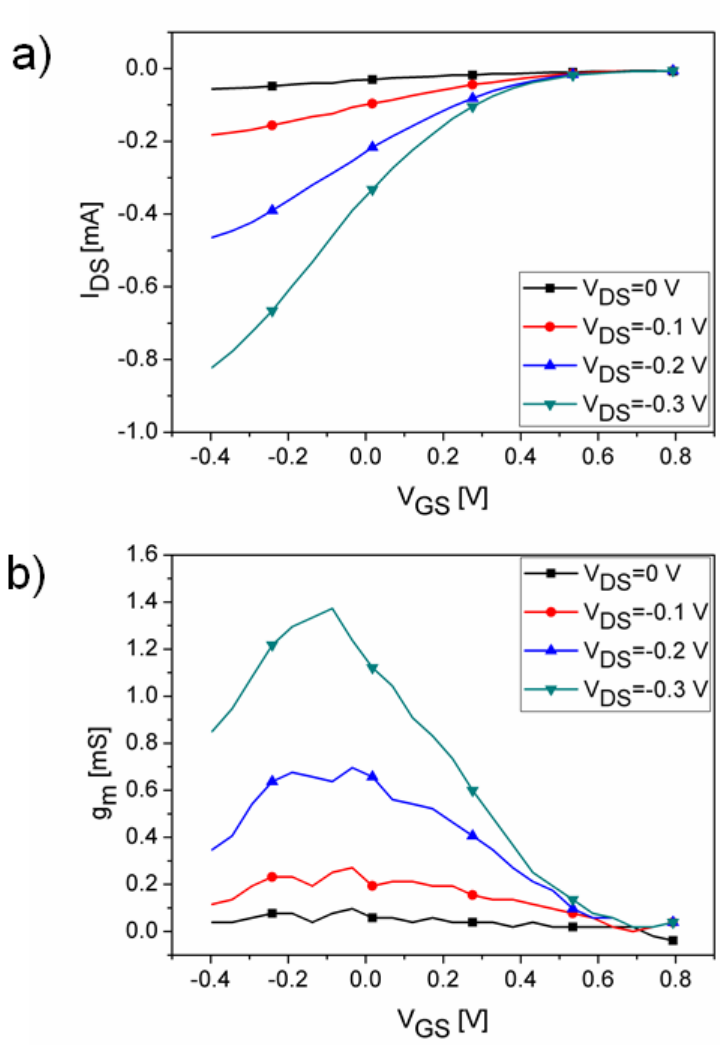

Figure 5-8 a) The transfer characteristics $I_{DS}(V_{GS})$ and b) the transistor transconductance g_m of an OECT device with the gate dimensions 100×10 µm^2 (single interdigitated source and drain electrode) measured with the TTF amplifier system.

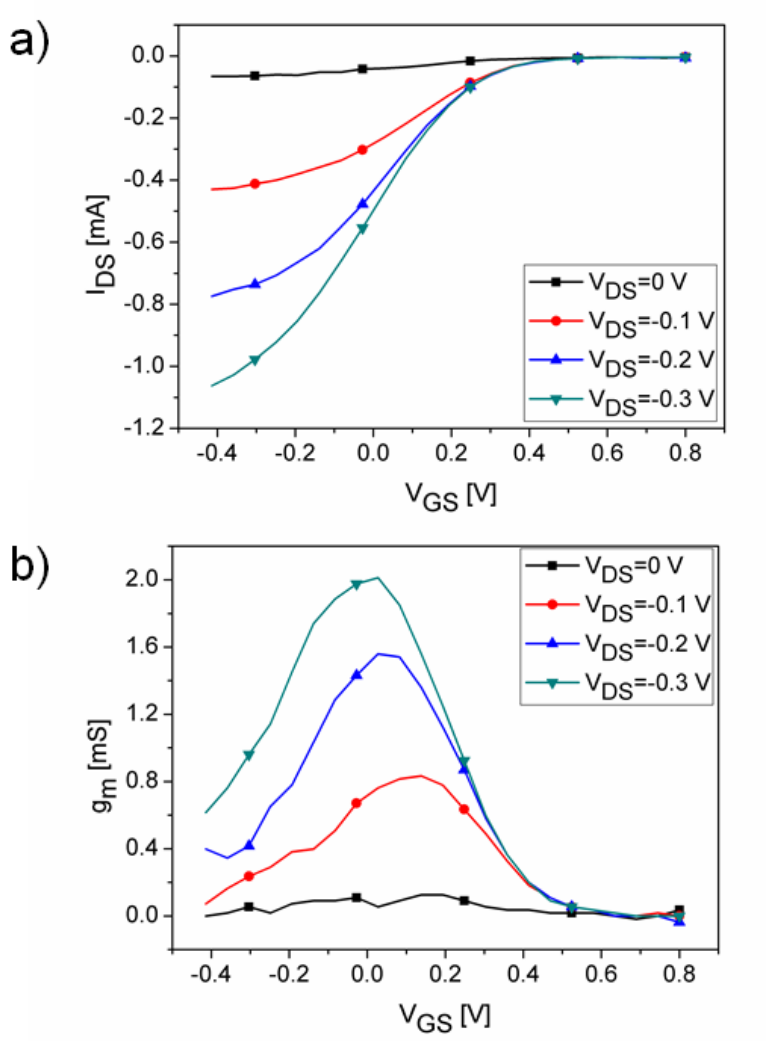

Figure 5-9 a) The transfer characteristics $I_{DS}(V_{GS})$ and b) the transistor transconductance g_m of an OECT device with the gate dimensions 100×100 µm^2 (4 interdigitated source and drain electrodes) measured with the TTF amplifier system.

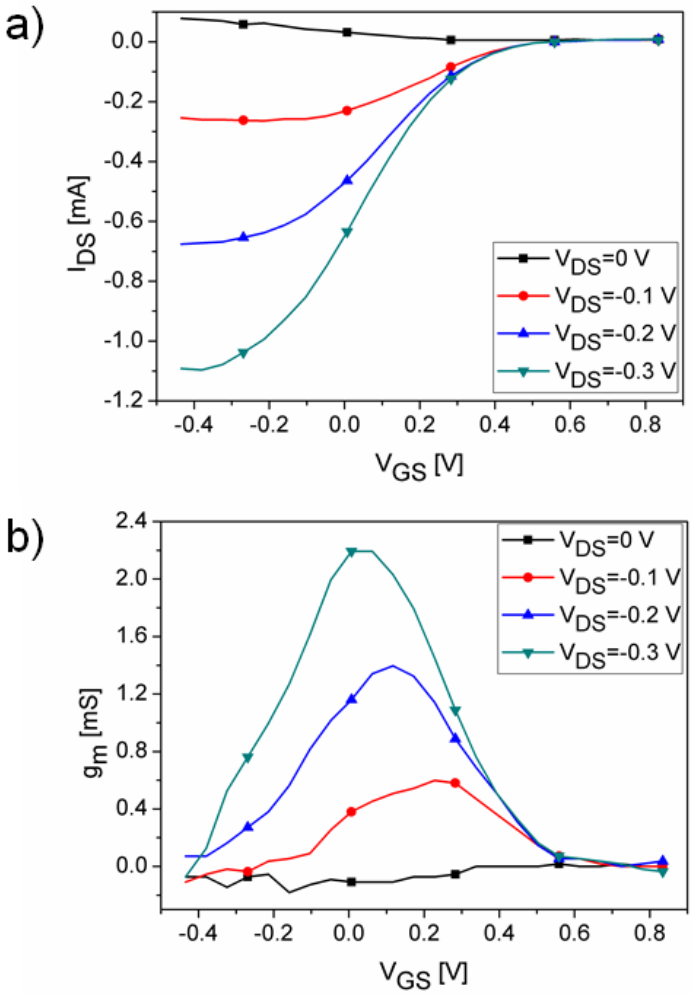

Figure 5-10 a) The transfer characteristics $I_{DS}(V_{GS})$ and b) the transistor transconductance g_m of an OECT device with the gate dimensions 200×200 µm^2 (8 interdigitated source and drain electrodes) measured with the TTF amplifier system.

In Table 5-3 the transconductance values g_m measured using wafer probe station before encapsulation of the OECT devices and using TTF amplifier system after encapsulation of the OECT devices are compared. As it can be seen from the Table 5-3, the transonductance g_m decreased when the TTF amplifier system is used.

no. of interdigitated source and drain electrodes	gate area [µm^2]	g_m [mS] (wafer probe station)	g_m [mS] (TTF amplifier system)
8	200×200	10.87	2.2
4	100×100	15.23	2
1	100×10	3.59	1.4

Table 5-3 In this table, the transconductance values g_m of different OECT devices measured at a wafer probe station and with a TTF amplifier system are compared.

The difference between characterization of a single device at a wafer probe station to the parallel recordings of 16 channels in a common source layout in our TTF amplifier system is well known from the characterization of silicon FET devices.

The effect of the gate geometry in terms of a multiple interdigitated electrodes layout on the electrical performance of the OECT devices was monitored. It can be clearly observed that the transconductance g_m increases with the increase of the ratio of gate width to gate length as it is known from silicon devices. In terms of electrical performance the OECT devices have high transconductance values in the mS range. A maximum value of the transconductance of 2.2 mS was achieved for the gate area 200×200 µm^2, when measured at the amplifier for cell recordings.

In order to investigate the stability of the organic semiconductor device recordings the drift in the output signal was measured as well. The drain-source current of an OECT device was monitored as a function of time. The complete measurement lasted for 3 hours. Figure 5-11 shows the drift of the signal over time. The drain-source current decreased in the first 30 min and then nearly saturated.

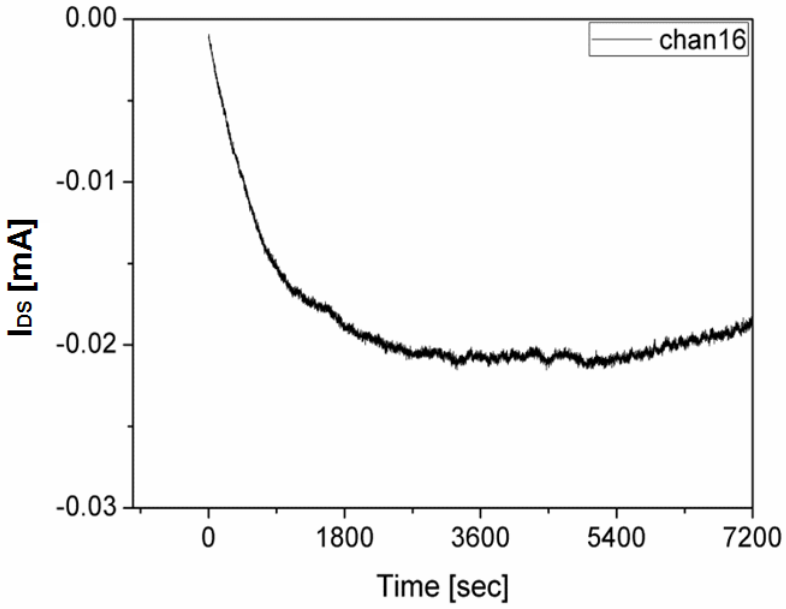

Figure 5-11 Drift measurement of a typical OECT device.

For electrical cell-substrate impedance measurements with these devices, stable impedimetric recordings are necessary. Figure 5-12 shows the frequency response of the OECT devices with respect to the device geometry. As it can be seen from this figure, the switching speed is limited to 1 kHz depending on the device geometry. Again the devices with 200×200 µm^2 gate size showed the fastest performance. In general the bandwidth is much smaller compared to our silicon devices, which is a result of the much lower carrier mobility in the OECT devices. Netherless the OECT in our impedance sensing configuration showed a stable performance and can be used for cell adhesion experiments.

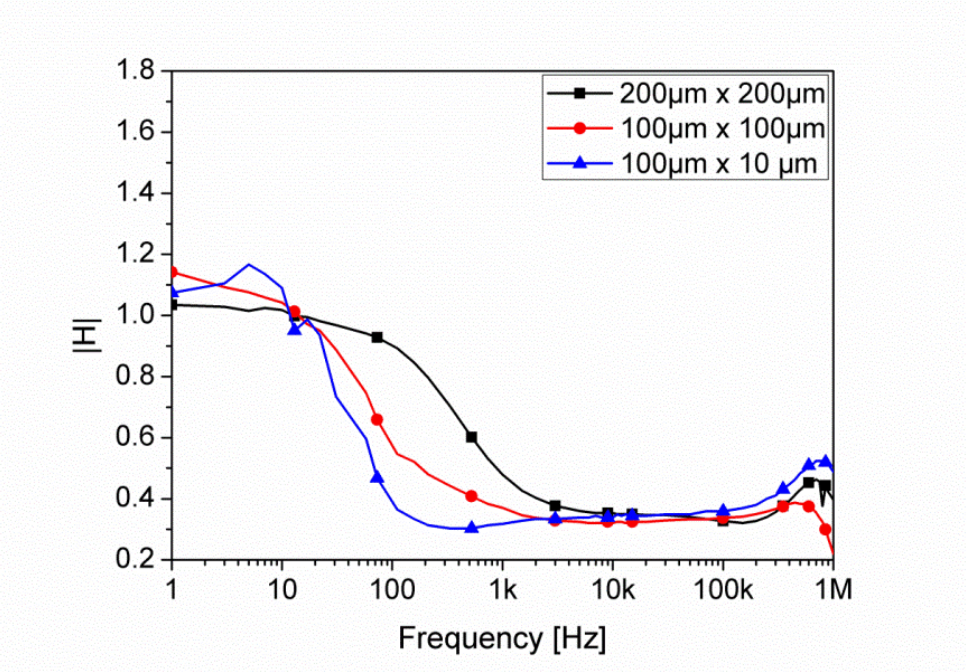

Figure 5-12 The impedance spectra of different OECT devices (gate dimensions: 100×10 µm^2, single interdigitated source and drain electrode, g_m = 1.36 mS; gate dimensions: 100×100 µm^2, 4 interdigitated source and drain electrodes, g_m = 2 mS; gate dimensions: 200×200 µm^2, 8 interdigitated source and drain electrodes, g_m = 2.19 mS) measured with the TTF amplifier system.

5.3 Impedimetric properties of the OECT devices in buffer solution with different ionic strength

In this section, the impedance properties in buffer solutions having different ionic strength were tested. In the TTF experiments with silicon FETs it is well known that with changing conductivity of the solution (hence changing R_{el} in the equivalent circuit) large changes in the spectra can be observed. The transfer characteristics of the OECT devices as well as the impedance spectra presented here were all measured using the TTF amplifier system.

In Figure 5-13a the transfer characteristics of an OECT device (with the gate dimensions of 50×10 µm^2 having a single finger electrode) measured in sodium chloride (NaCl) solutions with different concentrations (from 1 mM to 100 mM) are presented. As it can be seen, the drain-source current I_{DS} decreased and the threshold voltage shifts to higher voltages with the

increase of the concentration of NaCl solution. Consequently, the transconductance of the OECT device was decreased with the increase of the concentration of NaCl solution (Figure 5-13b). This is very different from silicon FETs. In this case a stable gate oxide is located at the gate input where almost the complete gate voltage is dropping. In the silicon FET devices therefore no shift in the transfer characteristics with changing ionic strength of the test solution is visible. In contrast to this OECTs based on PEDOT:PSS are gated by cation penetration and doping and dedoping effects. Nevertheless also in the impedance spectra a clear change similar to the silicon FET spectra can be seen.

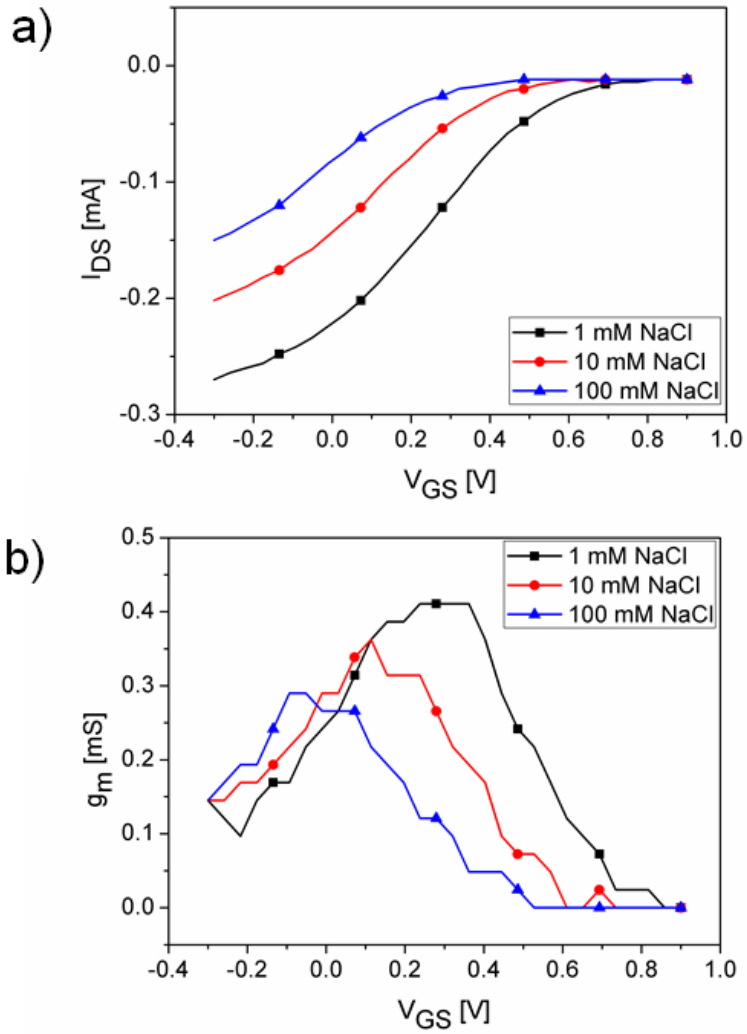

Figure 5-13 a) The transfer characteristics $I_{DS}(V_{GS})$ and b) the transistor transconductance g_m of an OECT device with the gate dimensions 50×10 µm^2 (single interdigitated source and drain electrode) at drain-source voltage V_{DS} = − 0.3 V measured with different concentration of the sodium chloride (NaCl) solution. The characteristic lines are shifting depending on the solt concentration while the low ionic strength buffer exhibits the highest transconductance value.

Figure 5-14 shows the impedance spectra measured using different concentrations of NaCl solution (from 1 mM to 100 mM). The increase in the cutoff frequency with increasing NaCl concentrations is mainly caused by the change of the electrolyte conductivity.

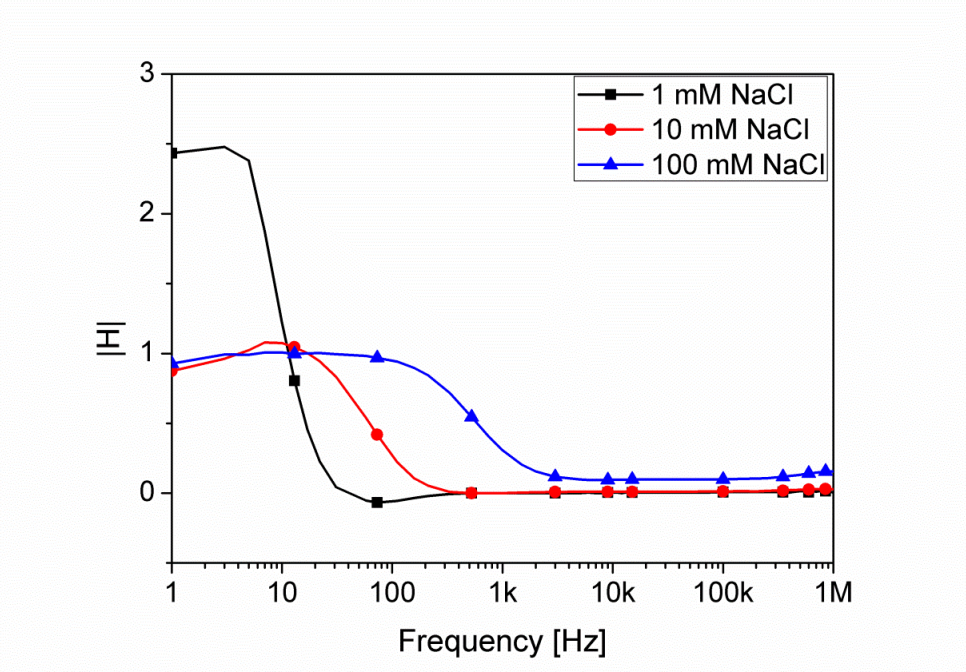

Figure 5-14 The impedance spectra of an OECT device with the gate dimensions 50×10 µm^2 (single interdigitated source and drain electrode) measured with different concentration of the sodium chloride (NaCl) solution.

The change in transconductance can also be seen in the low frequency part of the TTF recordings shown in Figure 5-14, where the lowest salt concentration shows the highest value. However, in the high frequency part the devices showed fastest reaction and highest low pass characteristics in higher salt concentration. This favours the cell adhesion experiments since the cells are usually recorded in physiological buffers with high salt concentration.

5.4 Cell adhesion measurements using OECT devices

The OECT devices were developed in this thesis with the objective to investigate the cell-substrate adhesion. Therefore, at first the biocompatibility of the devices was examined. Fig-

ure 5-15 shows that the cells grow very well on the PEDOT:PSS surface coated with ethylene glycol having a flat morphology.

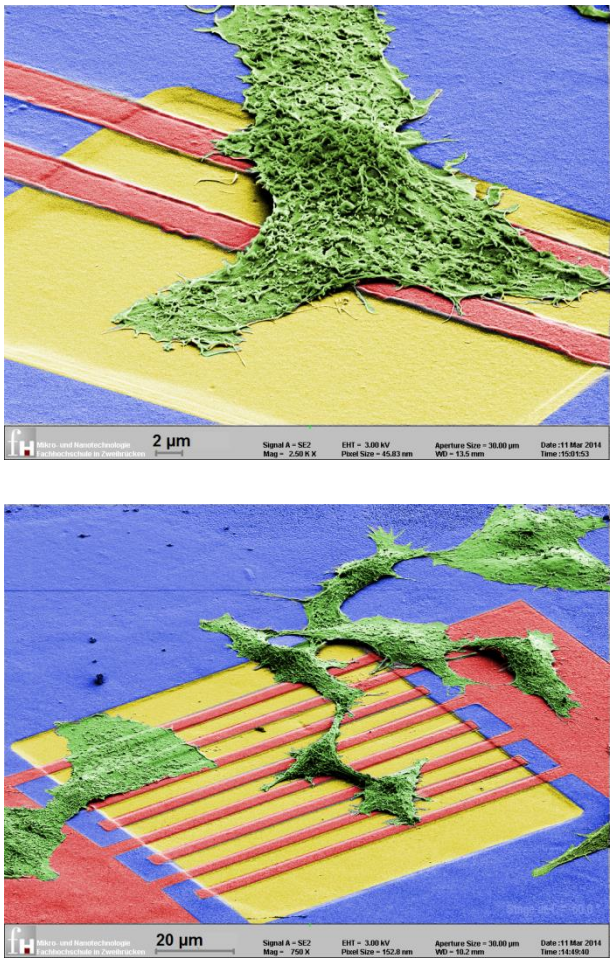

Figure 5-15 Colored scanning electron microscope images of HEK 293 cells cultured on OECT devices with single- (top) and multiple interdigitated source and drain electrodes design (bottom) with gate areas of 50×50 µm^2 and 100×100 µm^2, respectively. Cells adhered very closely to the surface although very low cell concentrations were used.

In Figure 5-16 the measured impedance spectra with and without cells on top of the interdigitated source and drain electrodes are compared. The cultured HEK 293 cells on the OECT device were treated with the 1 µg/ml trypsin solution in order to check the effect of the cells on the impedance spectra. Changes in impedance spectra were clearly monitored also with these devices.

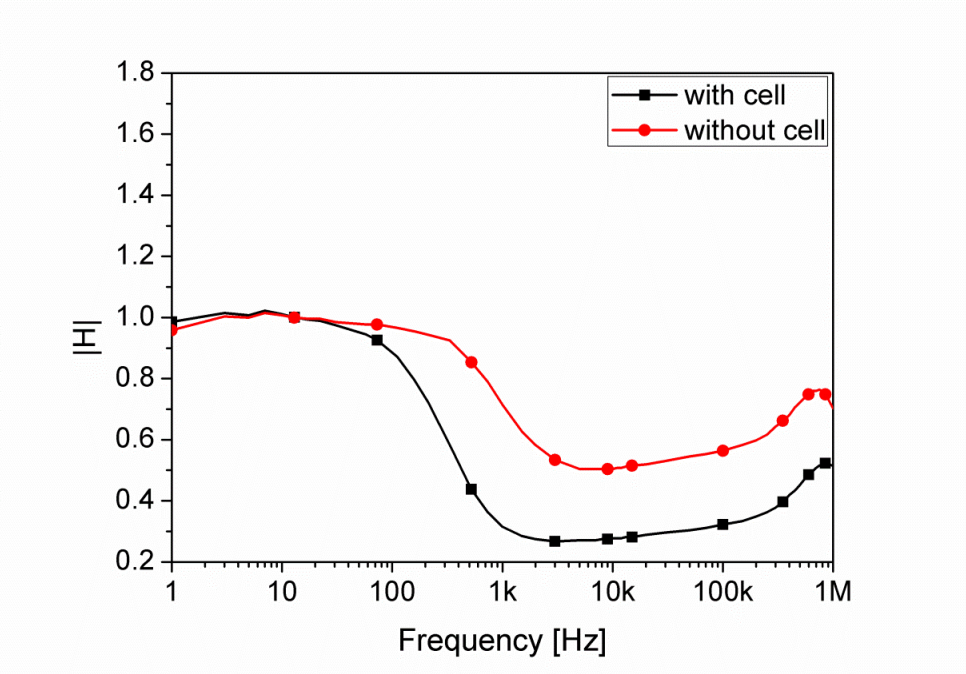

Figure 5-16 The impedance spectra measured before and after adding of 1 µg/ml trypsin solution with an OECT device using the TTF amplifier system. The cell detachment effect can be clearly seen.

In order to confirm that the measured effect was influenced by the detachment process of the cells from the transistor surface and not by eventual degradation of the device in impedance sensing, a control measurement was performed. In this control measurement the impedance spectra were measured one after another 10 times. No shift in cutoff frequency was monitored (Figure 5-17). The small shift in transconductance values can be explained by the decrease of the drain-source current because of the diffusion of cations from the culture medium into the PEDOT:PSS layer (Lin et al., 2010). This control experiment confirms that the change in impedance spectra measured before and after trypsin treatment in Figure 5-16 is induced by the detachment process of the cells from the transistor surface.

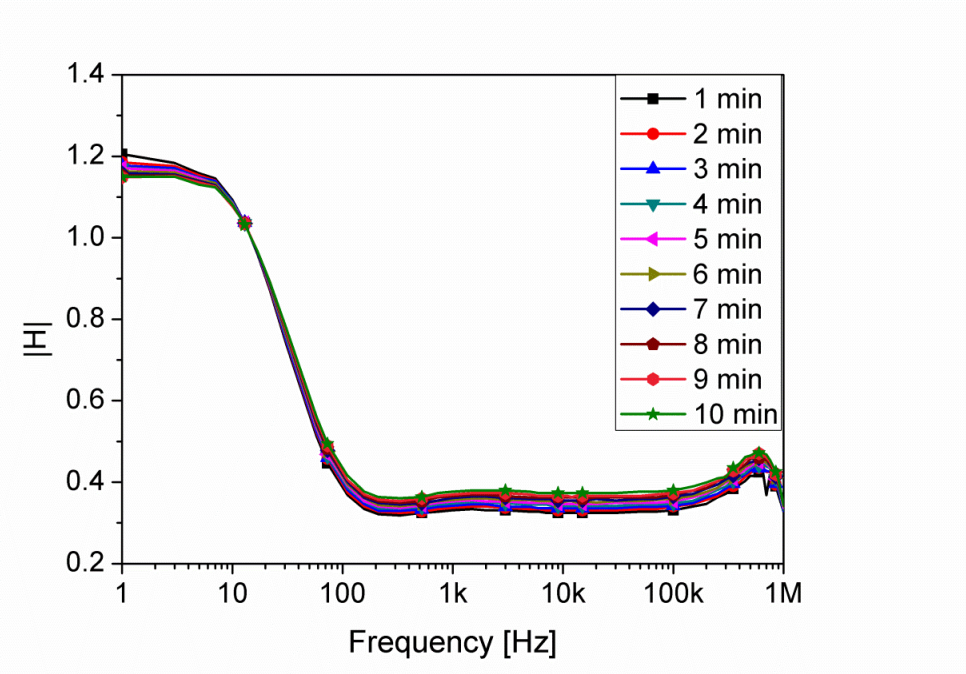

Figure 5-17 Control measurement, which confirmed that the measured effect in Figure 5-16 was a result of the detachment of the cells from the transistor surface after adding of 1 µg/ml trypsin solution and not by the degradation of the device.

The results presented in this chapter represent preliminary data using OECT devices for impedance monitoring of cells. First devices were fabricated, characterized and stabilized for experiments with cell culture.

It was shown that the OECTs exhibit some exiting properties for this kind of application. However, for more detailed studies and for simulation and explanation of the recorded effects in cell impedance measurements a follow up PhD thesis work has been started in our research group.

Chapter 6

6 Conclusion and outlook

In this thesis, a novel method for recording and investigation of the electrical cell-substrate adhesion using silicon-based, open-gate field-effect transistor devices was developed further. A detailed physical model to explain the recorded spectra and to extract cell-related parameters was elaborated and tested.

A new measurement setup with a fast lock-in amplifier was fabricated, which has following advantages compared to the previous amplifier system described in an earlier work in our group (Schäfer et al., 2009):

- increased bandwidth of the readout system
- measurements of the impedance spectra at higher frequencies (up to 50 MHz)
- time-dependent recordings at several different frequencies, simultaneously (Susloparova et al., 2015) (Susloparova et al., 2013).

With the newly developed measurement setup experiments with the human embryonic kidney (HEK293) cell line and human lung adenocarcinoma epithelial (H441) cell line were performed. Typical shapes of the impedance spectra for cell-free transistor gates and for the transistor gates covered by a single cell were recorded (Susloparova et al., 2013). The changes in the measured impedance spectra caused by the adhesion of individual cells were proven by chemical as well as mechanical removal of individual cells from the transistor gate surface (Susloparova et al., 2015). It was demonstrated that also an investigation of the efficiency of

anticancer drug on a single cell level is possible in long term experiments with this technique. The apoptosis event induced by a chemotherapeutic drug, topotecan hydrochloride, was observed time-dependently at several different frequencies, simultaneously. It was shown that the effects observed in time-dependent recordings at a fixed frequency is critical and is not revealing the full information. Nevertheless, this readout technique can be used for testing of the specificity and for interpretation of the effects of novel anticancer drugs on a single cell level. Eventually, the responses of malign and healthy cells in co-culture on the same chip can be compared. Such systems could be used in individual cancer therapy to find the optimal drug composition for the patient.

An electrically equivalent circuit (EEC) model composed of cell-related, device-related and transimpedance amplifier-related parameters was developed. This EEC model was implemented in a program for electrical circuit simulation, and the effect of different parameters on the impedance spectra was studied. In addition, an analytical expression representing the transfer functions was derived. The measured impedance spectra with the developed amplifier system were fitted with the derived analytical expression and the cell-related parameters were extracted. The ability to extract the biological relevant data from these complex spectra might be very important for the future application of our novel technique in biological experiments.

Moreover, the EEC model was utilized to optimize the FET device performance for impedimetric sensing of individual cell adhesion (Susloparova et al., 2014). Different simulations were carried out by varying the device-related parameters. From performed simulations it was derived that increased contact line capacitances, as well as an increased transconductance value of the FET devices lead to larger cell-substrate adhesion effects. The simulation results were considered in a new design and fabrication of the new generation of the FET devices for impedance monitoring. By comparing the impedace spectra measured using the previous and the new generation of FET devices, it was clearly shown that the differences in impedance spectra measured for the cell-free and cell-covered transistor gates can be recognized.

In the last part of this thesis, organic electrochemical transistor (OECT) devices were developed. The typical electrochemical gating behavior of the fabricated OECT devices, the biocompatible features of the devices as well as the cell-adhesion measurements on OECT devices was demonstrated. These experiments in the late part of this thesis eventually open up commercial opportunities for the Electrical Cell-substrate Impedance Sensing using field-effect transistors. The OECTs could be fabricated on cheap polymer materials in a roll-to-roll process, they could be very compatible for cell cul-

ture due to their transparency, and they could be used as disposable sensors. These promising results triggered a follow up PhD thesis in our research group.

7 Appendix

7.1 Fabrication process of the former generation of the FET devices

In this section, the fabrication process of the former generation of the FET devices will be described (Krause, 2000). These sensors were used in the first part of this thesis work. In the first step, 1 µm silicon oxide (basic silicon oxide layer) was grown on n-type silicon wafers. The conducting lines were defined by a first lithography step and etching of the basic silicon oxide layer by buffered hydrofluoric (BHF) acid (Figure 7-1).

Figure 7-1 In the first step, the basic silicon oxide (SiO_2) layer (1 µm) was grown on silicon wafers, the conducting lines were defined and afterwards the basic silicon oxide layer was etched.

Afterwards, boron ions were implanted on the exposed conducting lines with a high dose of $8 \cdot 10^{15}$ ions/cm^2 and an energy of 120 keV. The subsequent diffusion step shifts the implantation profile into the wafer. Thereby, the boron ions diffuse both into the silicon and also under the area, which is still covered with the silicon oxide mask. After this diffusion step, a wet oxidation of silicon wafers was carried out. Thereby, the basic silicon oxide layer as well as the area over the implanted areas was increased by 110 nm (Figure 7-2).

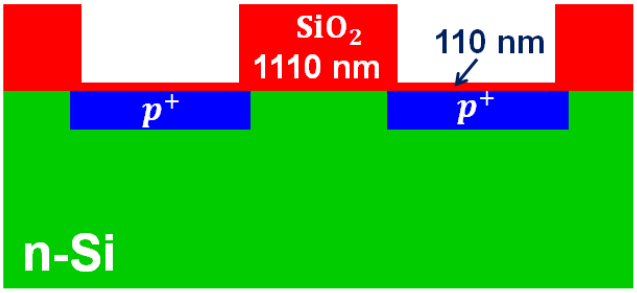

Figure 7-2 In the second step, the oxide-free places were implanted with boron ions. In the subsequent diffusion and oxidation step, the implantation profile was shifted into the wafer and during this step the conducting lines were covered with silicon oxide (110 nm).

In the second lithography step, the source and drain areas were defined. Afterwards, the oxide of the previously implanted areas and the basic silicon oxide layer remaining at the source and drain areas was etched by BHF acid. A second boron implantation was done with a dose of $5 \cdot 10^{15}$ ions/cm^2 and an energy of 80 keV to define source and drain. The subsequent diffusion and oxidation steps lead to ion diffusion into the wafer and to the creation of a silicon oxide layer of 250 nm over the implantation areas, respectively (Figure 7-3).

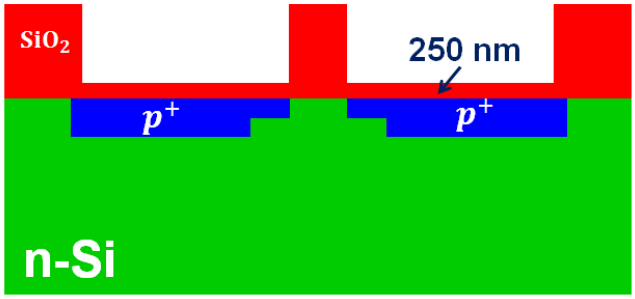

Figure 7-3 Definition of the source and drain areas, second boron implantation, and creation of the silicon oxide layer of 250 nm over the implantation areas.

The third lithography step defines 16 gate areas and contact areas. The silicon oxide was removed with BHF acid and 60 nm of protective silicon oxide for the late silicon nitride etch was grown (Figure 7-4)

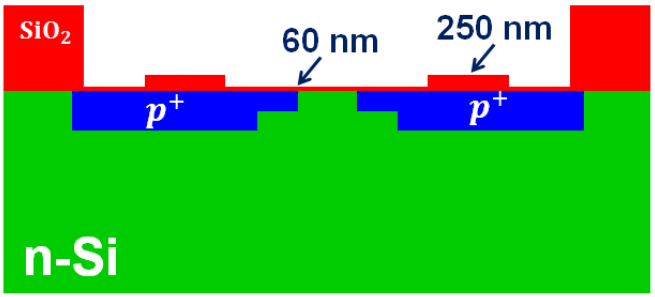

Figure 7-4 The gate and contact areas were opened and 60 nm of a protective silicon oxide (SiO_2) layer over these areas was created.

In the next step a Low-Pressure-Chemical-Vapour-Deposition (LPCVD) process was used to create a silicon nitride (Si_3N_4) layer of 125 nm. Afterwards, 100 nm of Plasma Enhanced-Chemical-Vapour-Deposition (PECVD) oxide layer was used to core the complete chip surface for better controlled surface chemistry (Figure 7-5).

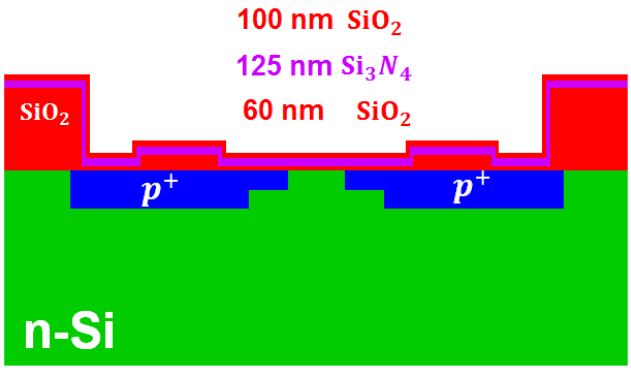

Figure 7-5 125 nm of the silicon nitride (Si_3N_4) layer for passivation and of 100 nm of silicon oxide (SiO_2) layer for better chemical functionalization of the sensor surface were created.

In the fourth lithography step, the final size of gate and contact areas was defined. The PECVD oxide layer was removed with BHF acid. The LPCVD nitride layer was removed with Isotropic-Chemical-Plasma etching process, which stopped at the protective silicon oxide layer. This was then removed with BHF acid down to the pure silicon layer on the gate surfaces (Figure 7-6).

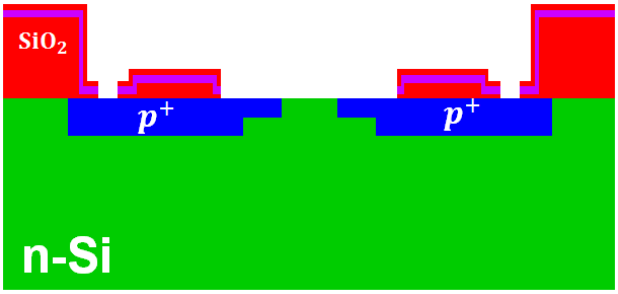

Figure 7-6 After deposition of the ONO-stack, the gate area was opened by a combination of dry and wet etching.

In the next step, the gate oxide of 8, 10 or 12 nm was grown in a dry oxidation process over the gate area (Figure 7-7).

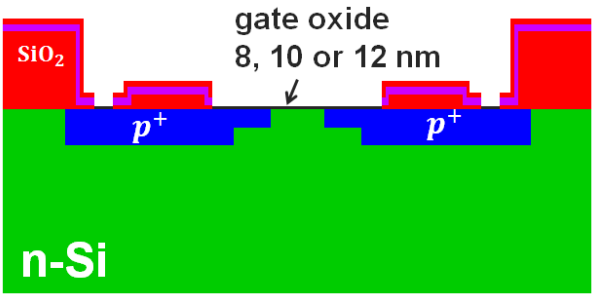

Figure 7-7 A thin silicon dioxide layer (12, 10, or 8 nm) was formed in a dry oxidation process and was used as a gate dielectric.

In the fifth lithography step, the contact areas at the bond pads were defined, which were then etched in a subsequent etch process with BHF acid. The sixth lithography step was realised with an Image-Reversal (IR) resist. The bond pad areas were metallised with 200 nm of aluminium followed by annealing to form good ohmic contacts (Figure 7-8).

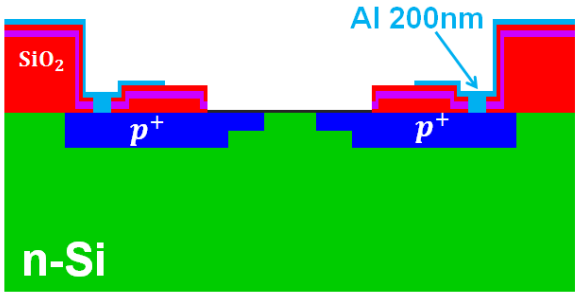

Figure 7-8 The contact areas were defined, which were etched in subsequent etch process with BHF acid. The sixth lithography step was realised in an Image-Reversal process. The bond pad areas were finally metallised with 200 nm of aluminium.

7.2 Fabrication process of the new generation of the FET devices

The fabrication of the new generation of the FET devices (the content of this section is based on a publication (Koppenhöfer et al., 2015)) was done on n-type silicon wafers (4 inch, resis-

tivity 2-10 Ω cm, Si-mat, Germany). In the first step, 1 µm silicon oxide was thermally grown in a wet oxidation process (1000°C, 5 hours), which acted as the masking layer for the ion implantation process (Figure 7-9). Prior to the oxidation, the wafers were cleaned by a standard RCA (Radio Cooperation of America) protocol.

Figure 7-9 1 µm of the silicon oxide (SiO_2) was grown on the n-type silicon wafer, which was used as a hard mask for implantation.

The contact lines were defined by optical lithography and wet etching of silicon oxide by BHF acid. The photoresist was removed and the wafer was cleaned by a standard RCA protocol before the first ion implantation. To reduce the contact line resistances, boron ions were implanted with a high dose and energy ($1 \cdot 10^{16}$ ions/cm^2, 150 keV) by an external supplier (IPS, France). The wafers were then cleaned in piranha solution with 1% hydrofluoric acid and annealed at 1050°C for 2 hours to activate the boron ions (Figure 7-10).

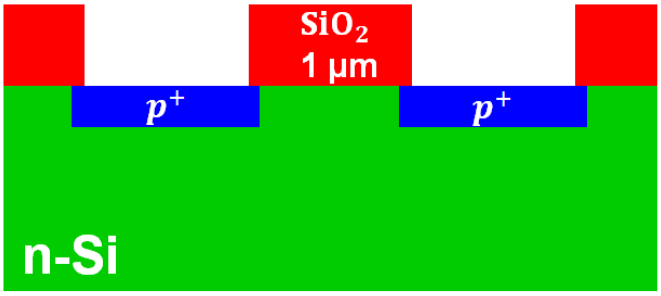

Figure 7-10 The contact line areas were defined by a first optical lithography and wet etching of the silicon oxide. Then the contact lines were implanted with boron with slightly higher dose and energy.

We defined the source and drain electrode areas by a second optical lithography and subsequent wet etching of the silicon oxide by BHF. A second boron implantation was done with a dose of $1 \cdot 10^{15}$ ions/cm^2 and an energy of 80 keV (Figure 7-11).

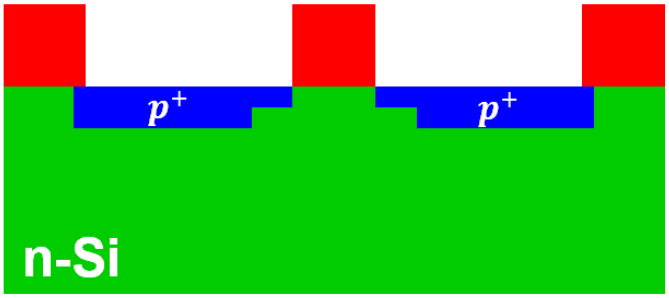

Figure 7-11 The source and drain areas were defined by a second optical lithography followed by wet etching of the silicon oxide. A second boron implantation was carried out for definition of source and drain contacts.

In the next step, in order to achieve a quasi-planar topography, all silicon oxide layers were completely removed from the entire wafer by wet etching in BHF and subsequent cleaning by the RCA protocol (Figure 7-12). This is then resulting to much larger contact line capacitances compared to the previous process.

Figure 7-12 For a quasi planar topography, the implantation oxide was removed completely in this process.

Then the wafers were annealed for 10 min in N_2 and subsequently brought into a wet oxidation process for 30 min, both at 900°C. With this annealing process we aimed to activate the dopants and to achieve a uniform 220 nm thick SiO_2 passivation layer on the complete chip surface (Figure 7-13).

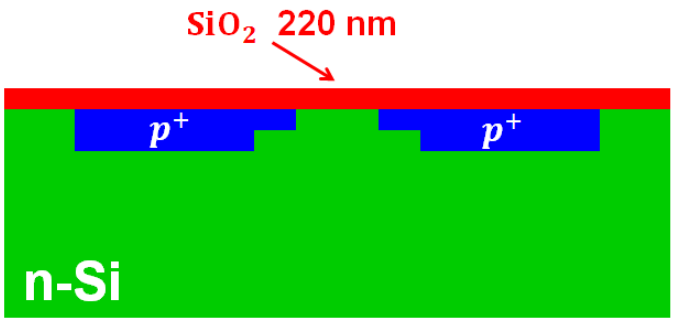

Figure 7-13 220 nm of silicon dioxide SiO_2 was grown as passivation layer on the whole surface.

A third lithography was applied to define the gate area and the outer source and drain contacts for final metallization. This etching step is quite delicate, since the surface, where the gate oxide is grown, will be opened. To reduce the roughness created by the wet etching process on the gate areas, the 220 nm thick silicon oxide layer was etched in BHF for 3 minutes and subsequently in 1% HF until the silicon oxide was totally etched. The resist was removed by acetone only and the wafer was carefully cleaned by an RCA protocol (Figure 7-14).

Figure 7-14 Definition of the source and drain contacts. The gate as well as the source and drain contact areas were opened.

The gate oxide layer was then thermally grown in a dry oxidation process (820° C, 40 min), which formed a 6 nm thick silicon oxide as gate dielectrics for the FET devices (Figure 7-15). This thickness was less compared to the previous process.

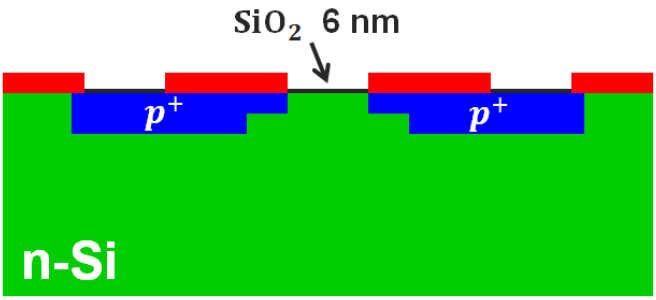

Figure 7-15 The 6 nm thick gate oxide (SiO_2) layer was thermally grown as gate dielectric.

At the end of the device fabrication, the outer metallizations to the source and drain contact lines were realized in a lift-off process. Prior to metal evaporation, the silicon oxide on the source and drain contacts were etched by 1% HF. A metal stack of 200 nm of aluminium, 20 nm of titanium and 100 nm of gold was deposited using electron beam evaporation (Figure 7-16). This enables also an encapsulation process by flip-chip. The metal contacts were then annealed for 10 min at 400°C in N_2 atmosphere in order to form good ohmic contacts.

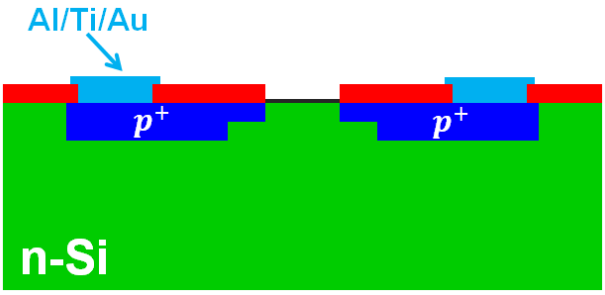

Figure 7-16 The source and drain electrical contacts at the outside of the sensor array were realized in a lift-off process (layer stack of Al/Ti/Au).

We used our standard design, where transistor gates are arranged in a 4×4 pattern localized in the center of a 7×7 mm^2 chip with a distance of 200 µm between individual gates. Typical gate size was 12×5 $µm^2$ (mask design), which resulted in an effective gate length of about 1.3 µm due to the under-diffusion in the process described above. Electron microscopy images show the almost planar design. Only at the gate area an opening of 220 nm is visible in the passivation layer, while the rest of the surface remained almost completely flat. Compared to

a previously described process this fabrication was much easier and faster and resulted in sensors which were much better suited for the single cell adhesion experiments in this thesis.

7.3 List of softwares, equipments and chemicals

Software

Origin	OriginPro 9.0, OriginLab Corporation, Germany
PSpice	OrCad Version 9.1, Cadence Design System Inc., San Jose, CA, USA
CleWin	CleWin3, http://clewin3.software.informer.com/
LabView	National Instruments, Germany

Equipment

Differential interference contrast microscope	Axiotech Vario, Carl Zeiss AG, Germany
Scanning electron microscope (SEM)	Carl Zeiss AG, Supra 40, Germany
Atomic force microscope (AFM)	Dimension 3100, Digital Instruments Veeco Metrology, Santa Barbara, USA
Precision semiconductor parameter analyzer	Precision Semiconductor Parameter Analyzer 4156C, Agilent
Printer	Dimatix Materials Printer 2800 (DMP-2800), FUJIFILM, USA
Contact angle instrument	OCA 15Plus, DataPhysics, Germany
Wedge-wedge wire bonding machine	West Bond Inc., USA
CO_2 Incubator	NuAire Inc., USA

Equipment for removal of an individual cell from the transistor surface

Patch-Clamp Pipette Puller	Sutter Instrument Co.. USA
Patch-Clamp Pipettes	Science Products GmbH, Germany

Equipment for measuring of the transfet functions (impedance spectra)

TTF amplifier system	TTF amplifier system – 5 kΩ, N. Wolters, Research Center Jülich, Germany
Lock-in amplifier	HF2LI, Zürich Instruments, Switzerland
Data acquisition card	USB 6251, National Instruments Inc., Germany

FET device encapsulation

68-pin LCC (Leaded Chip Carrier) carrier	Global chip Materials, LLC, USA
Epoxy glue	EPO-TEC 377 1LB Kit, Epoxy Technology Inc., USA
Polydimethylsiloxan (PDMS) glue	SYLGARD 184, Dow Corning, Germany

Chemicals

Acetone	ChemSolute, Germany
Isopropyl alcohol	Merck, Germany
Ethanol	ChemSolute, Germany
Sulfuric acid (H_2SO_4)	AppliChem GmbH, Germany
Helmanex II	Hellma Analytics, Germany
Fibronectin	AppliChem GmbH, Germany
Fetal Calf Serum (FCS)	PAN Biotech GmbH, Germany
Non-Essential Amino Acid (NEAA)	PAN Biotech GmbH, Germany
Penicillin/Streptomycin Solution	PAN Biotech GmbH, Germany
L-Glutamine	PAN Biotech GmbH, Germany
Trypsin	PAN Biotech GmbH, Germany
poly(3,4-ethylenedioxythiophene):poly(styrene sulfonic acid) (PEDOT:PSS)	Orgacon IJ-1005, Sigma Aldrich, Germany
Ethylene glycol (EG)	Sigma Aldrich, Germany

Chemical and buffer solutions

Sodium chloride (NaCl)	AppliChem GmbH, Germany
Phosphate Buffered Saline (PBS)	Sigma Aldrich, Germany

Cell culture

Roswell Park Memorial Institute medium (RPMI1640)	PAN Biotech GmbH, Germany
Minimal Essential Medium (M10)	PAN Biotech GmbH, Germany

Chemotherapeutic drug

Topotecan hydrochloride	Sigma Aldrich, St. Louis, Missouri, USA

Electronic components

Operational amplifier OP97	Distrelec Schuricht GmbH, Germany
Operational amplifier OPA627	Distrelec Schuricht GmbH, Germany

References

Abdurrahman, a, Price, D., Bhansali, S., 2007. Effect of electrode geometry on the impedance evaluation of tissue and cell culture. Sensors Actuators B Chem. 127, 89–96. doi:10.1016/j.snb.2007.07.038

Antonisse, M.M.G., Snellink-rue, B.H.M., Lugtenberg, R.J.W., Engbersen, J.F.J., Berg, A. Van Den, Reinhoudt, D.N., 2000. Membrane Characterization of Anion-Selective CHEMFETs by Impedance Spectroscopy 72, 343–348.

Arndt, S., Seebach, J., Psathaki, K., Galla, H.J., Wegener, J., 2004. Bioelectrical impedance assay to monitor changes in cell shape during apoptosis. Biosens. Bioelectron. 19, 583–594. doi:10.1016/S0956-5663(03)00269-0

Bartic, C., Campitelli, A., Borghs, S., 2003. Field-effect detection of chemical species with hybrid organic/inorganic transistors. Appl. Phys. Lett. 82, 475–477. doi:10.1063/1.1527698

Bartic, C., Palan, B., Campitelli, A., Borghs, G., 2002. Monitoring pH with organic-based ® eld-effect transistors 83, 115–122.

Basiric, L., 2012. Inkjet Printing of Organic Transistor Devices. University of Cagliari.

Basiricò, L., Cosseddu, P., Scidà, a., Fraboni, B., Malliaras, G.G., Bonfiglio, a., 2012. Electrical characteristics of ink-jet printed, all-polymer electrochemical transistors. Org. Electron. 13, 244–248. doi:10.1016/j.orgel.2011.11.010

Bergveld, P., 2003. Thirty years of ISFETOLOGY: What happened in the past 30 years and what may happen in the next 30 years. Sensors Actuators, B Chem. 88, 1–20. doi:10.1016/S0925-4005(02)00301-5

Bernards, D.A., Malliaras, G.G., Toombes, G.E.S., Gruner, S.M., 2006. Gating of an organic transistor through a bilayer lipid membrane with ion channels. Appl. Phys. Lett. 89. doi:10.1063/1.2266250

Bolin, M.H., Svennersten, K., Nilsson, D., Sawatdee, A., Jager, E.W.H., Richter-Dahlfors, A., Berggren, M., 2009. Active control of epithelial cell-density gradients grown along the channel of an organic electrochemical transistor. Adv. Mater. 21, 4379–4382. doi:10.1002/adma.200901191

Braun, D., Fromherz, P., 1998. Fluorescence Interferometry of Neuronal Cell Adhesion on Microstructured Silicon. Phys. Rev. Lett. doi:10.1103/PhysRevLett.81.5241

Brütting, W., 2005. Organic Semiconductors. Semiconductors 6, 1–11. doi:10.1016/B0-12-369401-9/00658-6

Brütting, W., Rieß, W., 2008. Grundlagen der organischen Halbleiter. Phys. J. 5, 33–38. doi:10.1002/ange.19710831423

Caboni, A., Orgiu, E., Barbaro, M., Bonfiglio, A., 2009a. Flexible Organic Thin-Film Transistors for pH Monitoring. IEEE Sens. J. 9. doi:10.1109/JSEN.2009.2032779

Caboni, A., Orgiu, E., Scavetta, E., Barbaro, M., Bonfiglio, A., 2009b. Organic-based sensor for chemical detection in aqueous solution. Appl. Phys. Lett. 95. doi:10.1063/1.3232252

Chovelon, J.M., Jaffrezic-Renault, N., Clechet, P., Cros, Y., Fombon, J.J., Baraton, M.I., Quintard, P., 1991. PECVD silicon oxynitride: A new insulator for ISFETs with insulator surface modified by chemical grafting. Sensors Actuators B Chem. doi:10.1016/0925-4005(91)80140-F

Curtis, A.S., 1964. The mechanism of adhesion of cells to glass. A styudy by interference refection microscopy. J. Cell Biol. 20, 199–215. doi:10.1083/jcb.20.2.199

E W Paul, Antonio J Ricco, et al, 1985. Resistance of polyaniline films as a function of electrochemical potential and the fabrication of polyaniline-based microelectronic devices. J. Phys. Chem. 89, 1441–1447.

Elmore, S., 2007. NIH Public Access 35, 495–516.

Fromherz, P., Offenhäusser, A., Vetter, T., Weis, J., 1991. A neuron-silicon junction: a Retzius cell of the leech on an insulated-gate field-effect transistor. Science 252, 1290–1293. doi:10.1126/science.1925540

FUJIFILM Dimatix Materials Printer DMP-2800 Series User Manual, 2010. . FUJIFILM Dimatix Mater. Print.

Geggier, P., Fuhr, G., 1999. Time-resolved total internal reflection aqueous fluorescence (TIRAF) microscope for the investigation of cell adhesion dynamics. Appl. Phys. A Mater. Sci. Process. 68, 505–514. doi:10.1007/s003390050933

GhoshMoulick, R., Vu, X.T., Gilles, S., Mayer, D., Offenhäusser, A., Ingebrandt, S., 2009. Impedimetric detection of covalently attached biomolecules on field-effect transistors. Phys. Status Solidi 206, 417–425. doi:10.1002/pssa.200880482

Giaever, I., Keese, C.R., 1991. Micromotion of mammalian cells measured electrically. Proc. Natl. Acad. Sci. U. S. A. 88, 7896–7900. doi:10.1073/pnas.88.17.7896

Giaever, I., Keese, C.R., 1993. A morphological biosensor for mammalian cells. Nature 366, 591–592. doi:10.1038/366591a0

Gleixner, R., Fromherz, P., 2006. The extracellular electrical resistivity in cell adhesion. Biophys. J. 90, 2600–2611. doi:10.1529/biophysj.105.072587

Groenendaal, B.L., Jonas, F., Freitag, D., Pielartzik, H., Reynolds, J.R., 2000. Its Derivatives : Past , Present , and Future ** 481–494.

Han, Y., 2006. Label-free detection of biomolecules by a field-effect transistor microarray biosensor with bio-functionalized gate surfaces. RWTH Aachen University.

HF2 User Manual, 2014. . Zurich Instruments AG.

Hodgkin, a L., Huxley, a F., 1952. A quantitative description of membrane current and its applicaiton to conduction and excitation in nerve. J Physiol 117, 500–544. doi:10.1016/S0092-8240(05)80004-7

Hofmann, B., 2009. Communicating with electrogenic cells. Rheinisch-Westfälische Technische Hochschule Aachen.

Hong, J., Kandasamy, K., Marimuthu, M., Choi, C.S., Kim, S., 2011. Electrical cell-substrate impedance sensing as a non-invasive tool for cancer cell study. Analyst 136, 237–245. doi:10.1039/c0an00560f

Ingebrandt, S., Han, Y., Nakamura, F., Poghossian, a, Schöning, M.J., Offenhäusser, a, 2007. Label-free detection of single nucleotide polymorphisms utilizing the differential transfer function of field-effect transistors. Biosens. Bioelectron. 22, 2834–40. doi:10.1016/j.bios.2006.11.019

Ingebrandt, S., Susloparova, A., Vu, X.T., Koppenhöfer, D., 2015. Device and method for measuring biological and/or electronic properties of a sample, and uses thereof. DE 10 2014 001 155 A1 2015.08.06.

Ingebrandt, S., Yeung, C.K., Krause, M., Offenhäusser, a, 2001. Cardiomyocyte-transistor-hybrids for sensor application. Biosens. Bioelectron. 16, 565–70.

Ingebrandt, S., Yeung, C.-K., Krause, M., Offenhäusser, A., 2005. Neuron-transistor coupling: interpretation of individual extracellular recorded signals. Eur. Biophys. J. 34, 144–54. doi:10.1007/s00249-004-0437-9

Janshoff, A., Kunze, A., Michaelis, S., Heitmann, V., Reiss, B., Wegener, J., 2010. Cell adhesion monitoring using substrate-integrated sensors. J. Adhes. Sci. Technol. 24, 2079–2104. doi:10.1163/016942410X507939

Ji, T., Rai, P., Jung, S., Varadan, V.K., 2008. In vitro evaluation of flexible pH and potassium ion-sensitive organic field effect transistor sensors. Appl. Phys. Lett. 92. doi:10.1063/1.2936296

Kanungo, M., Srivastava, D.N., Kumar, A., Contractor, A.Q., 2002. Conductimetric immunosensor based on poly(3,4-ethylenedioxythiophene). Chem. Commun. (Camb). 680–681. doi:10.1039/b111728a

Katz, E., Willner, I., 2003. Probing Biomolecular Interactions at Conductive and Semiconductive Surfaces by Impedance Spectroscopy: Routes to Impedimetric Immunosensors, DNA-Sensors, and Enzyme Biosensors. Electroanalysis 15, 913–947. doi:10.1002/elan.200390114

Kergoat, L., Piro, B., Berggren, M., Horowitz, G., Pham, M.-C., 2012. Advances in organic transistor-based biosensors: from organic electrochemical transistors to electrolyte-gated organic field-effect transistors. Anal. Bioanal. Chem. 402, 1813–26. doi:10.1007/s00216-011-5363-y

Khan, H.U., Roberts, M.E., Johnson, O., Förch, R., Knoll, W., Bao, Z., 2010. In situ, label-free DNA detection using organic transistor sensors. Adv. Mater. 22, 4452–4456. doi:10.1002/adma.201000790

Kharitonov, A.B., Wasserman, J., Katz, E., Willner, I., 2001. The Use of Impedance Spectroscopy for the Characterization of Protein-Modified ISFET Devices: Application of the Method for the Analysis of Biorecognition Processes. J. Phys. Chem. B 105, 4205–4213. doi:10.1021/jp0045383

Kim, D.-J., Lee, N.-E., Park, J.-S., Park, I.-J., Kim, J.-G., Cho, H.J., 2010. Organic electrochemical transistor based immunosensor for prostate specific antigen (PSA) detection using gold nanoparticles for signal amplification. Biosens. Bioelectron. 25, 2477–82. doi:10.1016/j.bios.2010.04.013

Koppenhöfer, D., Susloparova, a., Law, J.K.Y., Vu, X.T., Ingebrandt, S., 2015. Electronic monitoring of single cell-substrate adhesion events with quasi-planar field-effect transistors. Sensors Actuators B Chem. 210, 776–783. doi:10.1016/j.snb.2015.01.034

Krause, M., 2000. Untersuchungen zur Zell-Transistor Kopplung mittels der Voltage-Clamp Technik. Johannes Gutenberg-Universität Mainz.

Krishnamoorthy, K., Gokhale, R.S., Contractor, A.Q., Kumar, A., 2004. Novel label-free DNA sensors based on poly(3,4-ethylenedioxythiophene). Chem. Commun. (Camb). 820–821. doi:10.1039/b316794a

Kruise, J., Rispens, J.G., Bergveld, P., Kremer, F.J.B., Starmans, D., Haak, J.R., Feijen, J., Reinhoudt, D.N., 1992. Detection of charged proteins by means of impedance measurements. Sensors Actuators B Chem. doi:10.1016/0925-4005(92)80039-Z

Lambacher, A., Fromherz, P., 1996. Fluorescence interference-contrast microscopy on oxidized silicon using a monomolecular dye layer. Appl. Phys. A Mater. Sci. Process. doi:10.1007/s003390050374

Li, D.W., Borkent, E.J., Nortrup, R., Moon, H., Katz, H., Bao, Z.N., 2005. Humidity effect on electrical performance of organic thin-film transistors. Appl. Phys. Lett. 86. doi:Artn 042105\rDoi 10.1063/1.1852708

Li, N., 2005. β 1 integrins regulate mammary gland proliferation and maintain the integrity of mammary alveoli.

Lin, P., Luo, X., Hsing, I.M., Yan, F., 2011. Organic electrochemical transistors integrated in flexible microfluidic systems and used for label-free DNA sensing. Adv. Mater. 23, 4035–4040. doi:10.1002/adma.201102017

Lin, P., Yan, F., 2012. Organic thin-film transistors for chemical and biological sensing. Adv. Mater. 24, 34–51. doi:10.1002/adma.201103334

Lin, P., Yan, F., Chan, H.L.W., 2010a. Ion-sensitive properties of organic electrochemical transistors. ACS Appl. Mater. Interfaces 2, 1637–41. doi:10.1021/am100154e

Lin, P., Yan, F., Yu, J., Chan, H.L.W., Yang, M., 2010b. The application of organic electrochemical transistors in cell-based biosensors. Adv. Mater. 22, 3655–3660. doi:10.1002/adma.201000971

Liu, J., Agarwal, M., Varahramyan, K., 2008. Glucose sensor based on organic thin film transistor using glucose oxidase and conducting polymer. Sensors Actuators, B Chem. 135, 195–199. doi:10.1016/j.snb.2008.08.009

Lo, C.M., Keese, C.R., Giaever, I., 1995. Impedance analysis of MDCK cells measured by electric cell-substrate impedance sensing. Biophys. J. 69, 2800–2807. doi:10.1103/PhysRevE.57.6982

Loi, A., Manunza, I., Bonfiglio, A., 2005. Flexible, organic, ion-sensitive field-effect transistor. Appl. Phys. Lett. 86, 1–3. doi:10.1063/1.1873051

Lotfi, M., Nejib, M., Naceur, M., 2013. Cell Adhesion to Biomaterials : Concept of Biocompatibility. INTECH Open Access Publ. chapter 8, 207–240.

Lowe, S.W., Lin, A.W., 2000. Apoptosis in cancer 21, 485–495.

Meyburg, S., Stockmann, R., Moers, J., Offenhäusser, A., Ingebrandt, S., 2007. Advanced CMOS process for floating gate field-effect transistors in bioelectronic applications. Sensors Actuators, B Chem. 128, 208–217. doi:10.1016/j.snb.2007.06.003

Michaelis, S., Robelek, R., Wegener, J., 2012. Studying Cell – Surface Interactions In Vitro : A Survey of Experimental Approaches and Techniques 33–66. doi:10.1007/10

Mousavi, Z., Ekholm, A., Bobacka, J., Ivaska, A., 2009. Ion-selective organic electrochemical junction transistors based on poly(3,4-ethylenedioxythiophene) doped with poly(styrene sulfonate). Electroanalysis 21, 472–479. doi:10.1002/elan.200804427

Newman, J., 2008. Physics of the Life Sciences 401–430. doi:10.1007/978-0-387-77259-2

Nikolou, M., Malliaras, G.G., 2008. Applications of poly(3,4-ethylenedioxythiophene) doped with poly(styrene sulfonic acid) transistors in chemical and biological sensors. Chem. Rec. 8, 13–22. doi:10.1002/tcr.20133

Nilsson, D., Kugler, T., Svensson, P., Berggren, M., 2002. An all-organic sensor ± transistor based on a novel electrochemical transducer concept printed electrochemical sensors on paper 86, 193–197.

Ouyang, J., Xu, Q., Chu, C.-W., Yang, Y., Li, G., Shinar, J., 2004. On the mechanism of conductivity enhancement in poly(3,4-ethylenedioxythiophene):poly(styrene sulfonate) film through solvent treatment. Polymer (Guildf). 45, 8443–8450. doi:10.1016/j.polymer.2004.10.001

Pabst, M., Wrobel, G., Ingebrandt, S., Sommerhage, F., Offenhäusser, a, 2007. Solution of the Poisson-Nernst-Planck equations in the cell-substrate interface. Eur. Phys. J. E. Soft Matter 24, 1–8. doi:10.1140/epje/i2007-10204-6

Pancrazio, J.J., Whelan, J.P., Borkholder, D.A., Ma, W., Stenger, D.A., 1999. Development and application of cell-based biosensors. [Review] [157 refs]. Ann. Biomed. Eng. 27, 697–711.

Poghossian, a, Ingebrandt, S., Offenhäusser, a, Schöning, M.J., 2009. Field-effect devices for detecting cellular signals. Semin. Cell Dev. Biol. 20, 41–8. doi:10.1016/j.semcdb.2009.01.014

Pradhan, R., Mitra, A., Das, S., 2012. Characterization of Electrode/Electrolyte Interface of ECIS Devices. Electroanalysis 24, 2405–2414. doi:10.1002/elan.201200455

Regehr, W.G., Pine, J., Cohan, C.S., Mischke, M.D., Tank, D.W., 1989. Sealing cultured invertebrate neurons to embedded dish electrodes facilitates long-term stimulation and recording. J. Neurosci. Methods 30, 91–106. doi:10.1016/0165-0270(89)90055-1

Roberts, M.E., Mannsfeld, S.C.B., Queraltó, N., Reese, C., Locklin, J., Knoll, W., Bao, Z., 2008. Water-stable organic transistors and their application in chemical and biological sensors. Proc. Natl. Acad. Sci. U. S. A. 105, 12134–12139. doi:10.1073/pnas.0802105105

Rogers, J.A., Bao, Z., Baldwin, K., Dodabalapur, A., Crone, B., Raju, V.R., Kuck, V., Katz, H., Amundson, K., Ewing, J., Drzaic, P., 2001. Paper-like electronic displays: large-area rubber-stamped plastic sheets of electronics and microencapsulated electrophoretic inks. Proc. Natl. Acad. Sci. U. S. A. 98, 4835–4840. doi:10.1073/pnas.091588098

Santoro, F., Pud, S., Wolfrum, B., 2012. Cell-chip coupling for bioelectronic devices Lab manual.

Scarpa, G., Idzko, A.L., Yadav, A., Martin, E., Thalhammer, S., 2010a. Toward cheap disposable sensing devices for biological assays, in: IEEE Transactions on Nanotechnology. pp. 527–532. doi:10.1109/TNANO.2010.2060493

Scarpa, G., Idzko, A.L., Yadav, A., Thalhammer, S., 2010b. Organic ISFET based on poly (3-hexylthiophene). Sensors 10, 2262–2273. doi:10.3390/s100302262

Schäfer, S., Eick, S., Hofmann, B., Dufaux, T., Stockmann, R., Wrobel, G., Offenhäusser, a, Ingebrandt, S., 2009. Time-dependent observation of individual cellular binding events to field-effect transistors. Biosens. Bioelectron. 24, 1201–8. doi:10.1016/j.bios.2008.07.003

Schasfoort, R.B.M., Bergveld, P., Bomer, J., Kooyman, R.P.H., Greve, J., 1989. Modulation of the ISFET response by an immunological reaction. Sensors and actuators 17, 531–535. doi:10.1016/0250-6874(89)80041-1

Schatzthauer, R., 1998. Neuron-silicon junction with voltage-gated ionic currents. Eur. J. Neurosci. 10, 1956–1962. doi:10.1046/j.1460-9568.1998.00205.x

Shim, N.Y., Bernards, D.A., Macaya, D.J., DeFranco, J.A., Nikolou, M., Owens, R.M., Malliaras, G.G., 2009. All-plastic electrochemical transistor for glucose sensing using a ferrocene mediator. Sensors 9, 9896–9902. doi:10.3390/s91209896

Sirringhaus, H., Kawase, T., Friend, R.H., Shimoda, T., Inbasekaran, M., Wu, W., Woo, E.P., 2000. High-resolution inkjet printing of all-polymer transistor circuits. Science 290, 2123–2126. doi:10.1557/mrs2001.127

Someya, T., Dodabalapur, A., Gelperin, A., Katz, H.E., Bao, Z., 2002. Integration and response of organic electronics with aqueous microfluidics. Langmuir 18, 5299–5302. doi:10.1021/la020026z

Sommerhage, F., 2011. Chloride versus Protons Ion Currents in the Cell-Transistor Junction. RWTH Aachen University.

Sommerhage, F., Helpenstein, R., Rauf, A., Wrobel, G., Offenhäusser, A., Ingebrandt, S., 2008. Membrane allocation profiling: A method to characterize three-dimensional cell shape and attachment based on surface reconstruction. Biomaterials 29, 3927–3935. doi:10.1016/j.biomaterials.2008.06.020

Souteyrand, E., Cloarec, J.P., Martin, J.R., Wilson, C., Lawrence, I., Mikkelsen, S., Lawrence, M.F., Physicochimie, L. De, Lyon, E.C. De, Cedex, E., 1997. Direct Detection of the Hybridization of Synthetic Homo-Oligomer DNA Sequences by Field Effect 5647, 2980–2985.

Spijkman, M.-J., Brondijk, J.J., Geuns, T.C.T., Smits, E.C.P., Cramer, T., Zerbetto, F., Stoliar, P., Biscarini, F., Blom, P.W.M., de Leeuw, D.M., 2010. Dual-Gate Organic Field-Effect Transistors as Potentiometric Sensors in Aqueous Solution. Adv. Funct. Mater. 20, 898–905. doi:10.1002/adfm.200901830

Sprössler, C., Denyer, M., Britland, S., Knoll, W., Offenhäusser, A., 1999. Electrical recordings from rat cardiac muscle cells using field-effect transistors. Phys. Rev. E. Stat. Phys. Plasmas. Fluids. Relat. Interdiscip. Topics 60, 2171–2176.

Stoliar, P., Bystrenova, E., Quiroga, S.D., Annibale, P., Facchini, M., Spijkman, M., Setayesh, S., de Leeuw, D., Biscarini, F., 2009. DNA adsorption measured with ultra-thin film organic field effect transistors. Biosens. Bioelectron. 24, 2935–2938. doi:10.1016/j.bios.2009.02.003

Susloparova, A., Koppenhöfer, D., Law, J.K.Y., Vu, X.T., Ingebrandt, S., 2015. Electrical cell-substrate impedance sensing with field-effect transistors is able to unravel cellular adhesion and detachment processes on a single cell level. Lab Chip 15, 668–679. doi:10.1039/C4LC00593G

Susloparova, A., Koppenhöfer, D., Vu, X.T., Weil, M., Ingebrandt, S., 2013. Impedance spectroscopy with field-effect transistor arrays for the analysis of anti-cancer drug action on individual cells. Biosens. Bioelectron. 40, 50–56.

Susloparova, A., Vu, X.T., Koppenhöfer, D., Law, J.K.-Y., Ingebrandt, S., 2014. Investigation of ISFET device parameters to optimize for impedimetric sensing of cellular adhesion. Phys. Status Solidi 211, 1395–1403. doi:10.1002/pssa.201330636

Sze, S.M., 1981. Physics of Semiconductor Devices, 2nd ed, New York Wiley.

Sze, S.M., 2002. Semiconductor Devices: Physics and Technology, Technology.

Tang, H., Yan, F., Lin, P., Xu, J., Chan, H.L.W., 2011. Highly sensitive glucose biosensors based on organic electrochemical transistors using platinum gate electrodes modified with enzyme and nanomaterials. Adv. Funct. Mater. 21, 2264–2272. doi:10.1002/adfm.201002117

Tsukada, S., Nakashima, H., Torimitsu, K., 2012. Conductive Polymer Combined Silk Fiber Bundle for Bioelectrical Signal Recording. PLoS One 7, e33689. doi:10.1371/journal.pone.0033689

Uslu, F., Ingebrandt, S., Mayer, D., Böcker-Meffert, S., Odenthal, M., Offenhäusser, a, 2004. Labelfree fully electronic nucleic acid detection system based on a field-effect transistor device. Biosens. Bioelectron. 19, 1723–31. doi:10.1016/j.bios.2004.01.019

Van Hal, R.E.G., Eijkel, J.C.T., Bergveld, P., 1995. A novel description of ISFET sensitivity with the buffer capacity and double-layer capacitance as key parameters. Sensors Actuators B Chem. 24, 201–205. doi:10.1016/0925-4005(95)85043-0

Voelker, M., Fromherz, P., 2006. Nyquist noise of cell adhesion detected in a neuron-silicon transistor. Phys. Rev. Lett. 96. doi:10.1103/PhysRevLett.96.228102

Wegener, J., Keese, C.R., Giaever, I., 2000. Electric cell-substrate impedance sensing (ECIS) as a noninvasive means to monitor the kinetics of cell spreading to artificial surfaces. Exp. Cell Res. 259, 158–166. doi:10.1006/excr.2000.4919

Wiest, J., 2008. Entwicklung und Erprobung von miniaturisierten , elektrochemischen Sensoren für die Gelöst-Sauerstoff- Messung zum Einsatz in Lab-on-chip-Systemen. Technische Universität München.

Wrobel, G., Höller, M., Ingebrandt, S., Dieluweit, S., Sommerhage, F., Bochem, H.P., Offenhäusser, A., 2008. Transmission electron microscopy study of the cell-sensor interface. J. R. Soc. Interface 5, 213–22. doi:10.1098/rsif.2007.1094

Wrobel, G., Seifert, R., Ingebrandt, S., Enderlein, J., Ecken, H., Baumann, A., Kaupp, U.B., Offenhäusser, A., 2005. Cell-transistor coupling: investigation of potassium currents recorded with p- and n-channel FETs. Biophys. J. 89, 3628–3638. doi:10.1529/biophysj.104.049809

Xiao, C., Lachance, B., Sunahara, G., Luong, J.H.T., 2002. An in-depth analysis of electric cell-substrate impedance sensing to study the attachment and spreading of mammalian cells. Anal. Chem. 74, 1333–1339. doi:10.1021/ac011104a

Yamashita, M., Otani, C., Shimizu, M., Okuzaki, H., 2011. Effect of solvent on carrier transport in poly(3,4-ethylenedioxythiophene)/poly(4-styrenesulfonate) studied by terahertz and infrared-ultraviolet spectroscopy. Appl. Phys. Lett. 99, 143307. doi:10.1063/1.3647574

Yan, F., Mok, S.M., Yu, J., Chan, H.L.W., Yang, M., 2009. Label-free DNA sensor based on organic thin film transistors. Biosens. Bioelectron. 24, 1241–1245. doi:10.1016/j.bios.2008.07.030

Yang, S.Y., Cicoira, F., Byrne, R., Benito-Lopez, F., Diamond, D., Owens, R.M., Malliaras, G.G., 2010. Electrochemical transistors with ionic liquids for enzymatic sensing. Chem. Commun. (Camb). 46, 7972–7974. doi:10.1039/c0cc02064h

Yang, S.Y., Defranco, J.A., Sylvester, Y.A., Gobert, T.J., Macaya, D.J., Owens, R.M., Malliaras, G.G., 2009. Integration of a surface-directed microfluidic system with an organic electrochemical transistor array for multi-analyte biosensors. Lab Chip 9, 704–708. doi:10.1039/b811606g

Zhu, Z., Mabeck, J.T., Zhu, C., Cady, N.C., Batt, A., Malliaras, G.G., 2004. transistor for glucose sensing at neutral pH 1556–1557.

Zhu, Z.T., Mason, J.T., Dieckmann, R., Malliaras, G.G., 2002. Humidity sensors based on pentacene thin-film transistors. Appl. Phys. Lett. 81, 4643–4645. doi:10.1063/1.1527233

Ziersch, A., 1999. Optimierung der Mukoviszidose-Diagnostik und Überprüfung neuer Therapie-Ansätze auf der Basis der nasalen Potentialdifferenz-Messung. Justus-Liebig-Universität Giessen.

Publications

1. **A. Susloparova**, D. Koppenhöfer, X. T. Vu, M. Weil, S. Ingebrandt, "Impedance spectroscopy with field-effect transistor arrays for the analysis of anti-cancer drug action on individual cells", Biosens. Bioelectron. 40 (2013) 50–56, doi:10.1016/j.bios.2012.06.006
2. D. Koppenhöfer, **A. Susloparova**, D. Docter, R. H. Stauber, S. Ingebrandt, "Monitoring of nanoparticle induced cell death in H441 cells using field-effect transistors", Biosens. Bioelectron. 40 (2013) 89–95, doi:10.1016/j.bios.2012.06.031
3. **A. Susloparova**, X. T. Vu, D. Koppenhöfer, J. K. Y. Law, S. Ingebrandt, "Investigation of ISFET device parameters to optimize for impedimetric sensing of cellular adhesion" Phys. Status Solidi A 211 (2014) 1395–1403, doi:10.1002/pssa.201330636
4. J. K. Y. Law, **A. Susloparova**, X. T. Vu, X. Zhou, F. Hempel, B. Qu, M. Hoth, S. Ingebrandt, "Human T cells monitored by impedance spectrometry using field-effect transistor arrays: A novel tool for single-cell adhesion and migration studies", Biosens. Bioelectron. 67 (2015) 170-176, doi:10.1016/j.bios.2014.08.007
5. D. Koppenhöfer, F. Kettenbaum, **A. Susloparova**, J. K. Y. Law, X. T. Vu, T. Schwab, K. H. Schäfer, S. Ingebrandt, "Neurodegeneration through oxidative stress: Monitoring Hydrogen peroxide induced apoptosis in primary cells from the subventricular zone of BALB/c mice using field-effect transistors", Biosens. Bioelectron. 67 (2015) 490-496, doi:10.1016/j.bios.2014.09.012
6. **A. Susloparova**, D. Koppenhöfer, J. K. Y. Law, X. T. Vu, S. Ingebrandt, "Electrical Cell-substrate Impedance Sensing with field-effect transistors is able to unravel cellular adhesion and detachment processes on a single cell level", *Lab Chip 15* (2015) 668-679, doi:10.1039/C4LC00593G
7. D. Koppenhöfer, **A. Susloparova**, J. K. Y. Law, X. T. Vu, S. Ingebrandt, "Electronic monitoring of single cell-substrate adhesion events with quasi-planar field-effect transistors", Sens. Actuators B: Chem. 210 (2015) 776-783, doi:10.1016/j.snb.2015.01.034

Patent:

International application for a patent by the German Patent and Trade Mark Office (DPMA) PCT/DE2015/100040, S. Ingebrandt, **A. Susloparova**, X. T. Vu, D. Koppenhöfer "Device and method for measuring biological and/or electronic properties of a sample, and uses thereof", WO2015113560A1

Short oral presentations at conferences:

1. **A. Susloparova**, D. Koppenhöfer, X. T. Vu, S. Ingebrandt "Transfer function measurements with field-effect transistors for biomedical applications", Workshop Engineering of Functional Interfaces EnFI 2011, 19. – 20. Juli 2011, Linz, Austria
2. **A. Susloparova**, D. Koppenhöfer, X. T. Vu, S. Ingebrandt "Investigation of the effect of chemotherapeutic drugs on individual tumor samples using impedance spectroscopy measurements", Workshop Engineering of Functional Interfaces EnFI 2012, July 16th – 17th, 2012, Zweibrücken, Germany
3. **A. Susloparova**, D. Koppenhöfer, X. T. Vu, J. K.Y. Law, S. Ingebrandt "Investigation of the effects of the FET device parameters for chip design optimization" Workshop Engineering of Functional Interfaces EnFI 2013, July 08 & July 09, 2013, Hasselt, Belgium

Posters at conferences:

1. **A. Susloparova**, D. Koppenhöfer, X. T. Vu, S. Ingebrandt "Transfer function measurements with field-effect transistors for biomedical applications", Workshop Engineering of Functional Interfaces EnFI 2011, 19. – 20. Juli 2011, Linz, Austria
2. D. Koppenhöfer, **A. Susloparova**, T. Martin, S. Ingebrandt "Field-effect transistors as a novel tool in cancer research and therapy", Workshop Engineering of Functional Interfaces EnFI 2011, 19 – 20 Juli 2011, Linz, Austria
3. **A. Susloparova**, D. Koppenhöfer, X. T. Vu, S. Ingebrandt "Transfer function measurements with field-effect transistors", BMT-Biomedizinische Technik, 27 – 30 September 2011, Freiburg, Germany
4. D. Koppenhöfer, **A. Susloparova**, T. Martin, S. Ingebrandt "Field-effect transistors as modern tool in individual cancer therapy" BMT-Biomedizinische Technik, 27 – 30 September 2011, Freiburg, Germany
5. **A. Susloparova**, D. Koppenhöfer, X. T. Vu, S. Ingebrandt "Impedance spectroscopy with field-effect transistor arrays for the analysis of single cell adhesion", 22nd Anniversary World Congress on Biosensors 2012, 15 – 18 May 2012, Cancun, Mexico
6. D. Koppenhöfer, **A. Susloparova**, D. Docter, R. H. Stauber, S. Ingebrandt "Monitoring of nanoparticle induced cell death in H441 cells using field-effect transistors", 22nd Anniversary World Congress on Biosensors 2012, 15 – 18 May 2012, Cancun, Mexico

7. **A. Susloparova**, D. Koppenhöfer, X. T. Vu, S. Ingebrandt "Investigation of the effect of chemotherapeutic drugs on individual tumor samples using impedance spectroscopy measurements", Workshop Engineering of Functional Interfaces EnFI 2012, July 16th – 17th, 2012, Zweibrücken, Germany
8. D. Koppenhöfer, **A. Susloparova**, D. Docter, R. H. Stauber, S. Ingebrandt "Field-Effect Transistors in Cancer Research and Therapy: Monitoring Nanoparticles Induced Cell death in Human Cancer Cells", Workshop Engineering of Functional Interfaces EnFI 2012, July 16th – 17th, 2012, Zweibrücken, Germany
9. **A. Susloparova**, D. Koppenhöfer, X. T. Vu, J. K.Y. Law, S. Ingebrandt "Investigation of the effects of the FET device parameters for chip design optimization", Workshop Engineering of Functional Interfaces EnFI 2013, July 08 & July 09, 2013, Hasselt, Belgium
10. D. Koppenhöfer, **A. Susloparova**, J. K.Y. Law, X. T. Vu, S. Ingebrandt "Influence of cell morphology and area of gate coverage of single cells on impedimetric measurement of cell adhesion using field-effect transistors", Workshop Engineering of Functional Interfaces EnFI 2013, July 08 & July 09, 2013, Hasselt, Belgium
11. **A. Susloparova**, X. T. Vu, D. Koppenhöfer, J. K.Y. Law, S. Ingebrandt "Impedance spectroscopy with organic field-effect transistors for the analysis of cell adhesion", 2nd Conference on Impedance-Based Cellular Assays IBCA 2013, August 21 – 23, 2013, Budapest, Hungary
12. D. Koppenhöfer, **A. Susloparova**, J. K.Y. Law, X. T. Vu, S. Ingebrandt "Neurodegeneration and neuroprotection-Analyzing the effects of oxidative stress on neurons using impedance measurements with field-effect transistors", 2nd Conference on Impedance-Based Cellular Assays IBCA 2013, August 21 – 23, 2013, Budapest, Hungary
13. F. Hempel, N. Bernhard, J. K.Y. Law, **A. Susloparova**, D. Koppenhöfer, X. T. Vu, S. Ingebrandt "The influence of medium conductivity on electrical cell-substrate impedance measurements with field-effect transistor arrays", MEA Meeting 2014, 9th International Meeting on Substrate-Integrated Microelectrode Arrays and 1st Tübingen Symposium on Current Topics in Neurotechnology, July 1 – 4, 2014, Reutlingen, Germany
14. L. Delle, **A. Susloparova**, X. T. Vu, O. Fominov, F. Hempel, J. K.Y. Law, S. Ingebrandt "Organic field-effect transistor arrays are a possible low-cost alternative for in-vitro monitoring of different cell cultures", MEA Meeting 2014, 9th International Meeting on Substrate-Integrated Microelectrode Arrays and 1st Tübingen Symposium on Current Topics in Neurotechnology, July 1 – 4, 2014, Reutlingen, Germany

15. F. Hempel, **A. Susloparova**, J. K.Y. Law, S. Ingebrandt "Organic field-effect transistors for electric cell-substrate impedance sensing", Workshop Engineering of Functional Interfaces EnFI 2014, July 14 & 15, 2014, Aachen, Germany
16. J. K.Y. Law, X. T. Vu, **A. Susloparova**, S. Ingebrandt "Organic field-effect transistors for in-vitro action potential recordings", Workshop Engineering of Functional Interfaces EnFI 2014, July 14 & 15, 2014, Aachen, Germany
17. O. Fominov, **A. Susloparova**, X. T. Vu, S. Ingebrandt "pH-sensing properties of an organic field-effect transistors based on PEDOT:PSS", Workshop Engineering of Functional Interfaces EnFI 2014, July 14 & 15, 2014, Aachen, Germany

List of figures

List of tables

Acknowledgements

At this point, I would like to thank all who contributed to this work.

First, I would like to express my deep gratitude to Prof. Dr. Sven Ingebrandt for the opportunity to perform a doctorate with such exciting topic, for his great supervision, subject-specific discussions and suggestions, support and correction of this thesis.

I would like to express my deep gratitude to Prof Dr. Martin Eickhoff and Prof. Dr. Derck Schlettwein for friendly acquisition of dissertation advisors of this thesis.

My sincere thanks to:

Dr. Xuan Thang Vu for the introduction in different spheres of this work, fabrication of the new generation of silicon-based FET devices and OECT devices, support in clean room processes, comments and discussions during this work.

Dr. Jessica Ka-Yan Law for the patch-clamp removal of the cells for my experiments, cultivation of cell lines on the FET devices, comments and discussions during this work.

Dr. Maryam Weil for the subject-specific discussions and tips for preparation of the presentations, posters, and publications.

Dr. Vivek Pachauri for the characterizing of the sensor surfaces with the atomic force microscope.

Dieter Koppenhöfer for the good collaboration, discussions in biological topics and the cultivation of cell lines on the FET devices.

All members of our research group: Lotta Emilia Delle, Ruben Lanche, Thanh Chien Nguyen, Miriam Schwartz, Dipti Rani, Xiaoling Lu, Walid Munief, Felix Hempel, Achim Müller for the collaboration and for a great time in the group.

Rainer Lilischkis for the SEM images of the silicon-based FET devices and for the SEM images of the HEK293 cells on OECT devices.

Alice Kasjanow for the bonding and encapsulation of the FET chips in first phase of this work.

Tanja Martin and Nina Stock for the cultivation of cell lines on the FET devices.

Christian Astor for the introduction in the inkjet-printing process.

My family for the support in all aspects.

Selbstständigkeitserklärung

Ich erkläre: Ich habe die vorgelegte Dissertation selbständig und ohne unerlaubte fremde Hilfe und nur mit den Hilfen angefertigt, die ich in der Dissertation angegeben habe.
Alle Textstellen, die wörtlich oder sinngemäß aus veröffentlichten Schriften entnommen sind, und alle Angaben, die auf mündlichen Auskünften beruhen, sind als solche kenntlich gemacht.
Bei den von mir durchgeführten und in der Dissertation erwähnten Untersuchungen habe ich die Grundsätze guter wissenschaftlicher Praxis, wie sie in der „Satzung der Justus-Liebig-Universität Gießen zur Sicherung guter wissenschaftlicher Praxis“ niedergelegt sind, eingehalten.

Karlsruhe,14.04.2016 _____

Datum Unterschrift